RADIAL VELOCITY VARIATIONS IN RED GIANT STARS: PULSATIONS, SPOTS AND PLANETS

RADIAL VELOCITY VARIATIONS IN RED GIANT STARS: PULSATIONS, SPOTS AND PLANETS

Proefschrift

ter verkrijging van
de graad van Doctor aan de Universiteit Leiden,
op gezag van de Rector Magnificus prof. mr. P. F. van der Heijden,
volgens besluit van het College voor Promoties
te verdedigen op 18 september 2007
klokke 13:45 uur

door

Saskia Hekker

geboren te Heeze
in 1978

Promotiecommissie

Promotor:	Prof. dr. A. Quirrenbach	Sterrewacht Leiden Landessternwarte Heidelberg
Promotor:	Prof. dr. C. Aerts	Katholieke Universiteit Leuven Radboud Universiteit Nijmegen
Co-promotor:	Dr. I. A. G. Snellen	Sterrewacht Leiden
Overige leden:	Prof. dr. E. F. van Dishoeck	Sterrewacht Leiden
	Prof. dr. K. H. Kuijken	Sterrewacht Leiden
	Prof. dr. P. T. de Zeeuw	Sterrewacht Leiden
	Dr. M. Hogerheijde	Sterrewacht Leiden
	Dr. J. Lub	Sterrewacht Leiden

Dit proefschrift is tot stand gekomen met steun van

Nederlandse Organisatie voor Wetenschappelijk Onderzoek

No pain, no gain

Contents

CHAPTER 1

Introduction

In this Chapter some background information on the main topics of this thesis will be described. First, I will describe the red giant phase of stars, why stars in this phase are of particular interest, and some open questions. Subsequently, I will discuss two different spectroscopic calibration methods that are widely used to observe radial velocity variations, namely iodine cell and simultaneous ThAr observations. Both methods reach accuracies of order $\mathrm{m\,s^{-1}}$, but are based on different strategies. I will continue with some background information on oscillations, starspots and sub-stellar companions. These phenomena can all cause variations in the observed radial velocity, but expose different characteristics of the star. Oscillations reveal in a quasi-direct way the internal structure of a star, while starspots provide information on the magnetic field(s) of the star. Detection of sub-stellar companions contributes to present knowledge on the formation and evolution of planetary systems. Following the description of these phenomena, I will discuss why they can cause similar observational results in radial velocity measurements. A variation, or a lack of variation, in spectral line shape plays an important role in distinguishing between the different phenomena, and, therefore, spectral line shape diagnostics are presented together with some examples for oscillations, spots and companions.

An overview of the contents of the subsequent chapters of this thesis is provided at the end of the introduction.

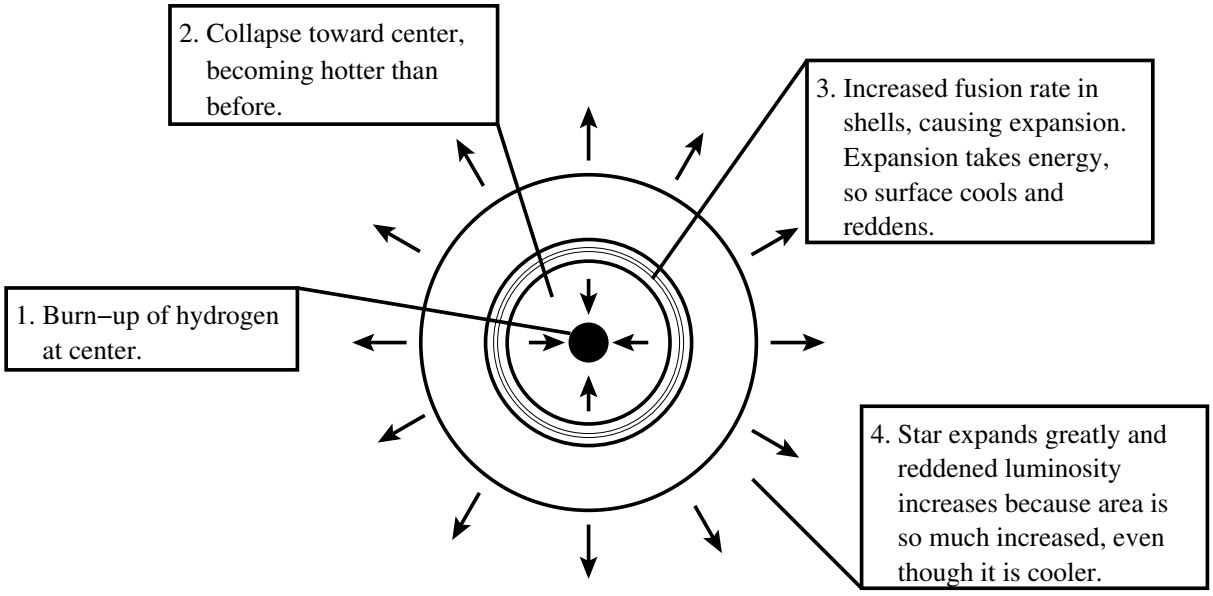

Figure 1.1: The evolution of a red giant.

1.1 RED GIANT STARS

It is generally thought that stars are born in an interstellar cloud, which collapses under its own gravity. The mass of this cloud is one of the parameters determining the mass of a star. During the main sequence life of stars, energy is generated in the core by fusion of hydrogen to helium. The star is in hydrostatic equilibrium in this phase with equal, but opposite, pressure and gravitational forces. Over time the star develops towards an object with a core of pure helium surrounded by a hydrogen shell. The temperature in the core is not (yet) sufficient to fuse helium to carbon. Without a source of energy generation, the helium core cannot support itself against gravitational collapse. Consequently, the core starts to collapse, which results in a temperature increase. Due to this temperature rise, the fusion in the hydrogen shell increases, and the outer layers of the star will expand and cool. The collapse of the core continues until it reaches a temperature of 100 million degrees, at which fusion of helium to carbon starts. The star expands and cools further due to the increased heating in the core, and eventually progresses to an equilibrium phase. This evolution is schematically shown in Figure 1.1.

Red giant stars are of particular interest for several reasons:

1. Every star with a mass between 0.4 and 10 times the mass of the sun should eventually go through a red giant phase. Only in the red giant phase carbon and more heavy elements are formed, the basis of all life, and, therefore, this is an important phase in stellar evolution.

2. A large fraction of the brightest stars are red giants. Not only the number of stars is large, but they are also observable over large distances, which make them potential reference stars for e.g. astrometry.

3. Research on red giants is a way to learn more about massive stars. Massive stars on the main sequence rotate rapidly and are very hot. As a result, they do not have many spectral

lines, and the ones they have, are broadened due to rotation. When these stars turn off the main sequence, they cool down and their rotational velocity decreases, which increases the number of spectral lines and narrows them. In this phase, it becomes possible to perform spectroscopic measurements to detect small radial velocity variations.

4. Red giants are ideal targets for stellar oscillation studies. They have large turbulent atmospheres in which solar-like oscillations are excited. The frequency with maximum power of solar-like oscillations scales with radius^{-2}. Therefore, for expanded stars like red giants, maximum power occurs at lower frequencies, i.e. longer periods (order hours), compared to the sun (order minutes). Furthermore, the velocity amplitude scales with luminosity. Therefore, larger velocity amplitudes (order m s $^{-1}$) are present in red giant stars compared to the sun (order cm s^{-1}).

Red giant stars are studied for many different phenomena. The extended outer atmosphere is studied for e.g. oscillations, dredge up of lithium or other metals, turbulence patterns and massive winds. Here I will provide a more detailed description of some open questions related to the research described in this thesis:

1. What does the internal structure of red giant stars look like in detail? For instance the thickness of different layers and the overshoot between those layers, as well as mass, age and differential rotation, if present, are not known in detail. Also, from the colour and magnitude of a star, it is difficult to determine in what state the star is, i.e. before or after the onset of helium burning. With observations of radial and non-radial oscillations, the internal structure of stars can be probed. The conclusion that non-radial oscillations are present among the observed solar-like oscillations in three red (sub)giant stars, as described in Chapter 2 of this thesis, can be a first step towards a better understanding of the stellar structure.

2. What is the excitation mechanism of long period variable red giants? Data obtained from a number of photometric surveys revealed that red giants can be variable with small amplitudes or with long periods. These are two distinct types of pulsating red variables. From a theoretical point of view, Xiong & Deng (2007) recently presented calculations in which they include dynamic coupling between convection and oscillations as a first step to reveal the excitation mechanism of the long period variations. The radial velocity variations observed in the spectroscopic survey of red giants presented in this thesis have periods of the same order as the ones observed photometrically. The investigation of the cause of the radial velocity variations as described in Chapter 4 of this thesis, may contribute to reveal the excitation mechanism of the long period variable red giants.

3. Which parameters dominate the formation of sub-stellar companions? Sub-stellar companions are predominantly found around main sequence stars with super-solar abundance, but also a correlation between sub-stellar companion occurrence and stellar mass seems to be present. By investigating red giants it is possible to probe stars with higher masses for the presence of sub-stellar companions. With a larger mass range and the metallicities of these stars it might be possible to reveal the role of these parameters on the formation of sub-stellar companions. A preliminary comparison of the iron abundance of 380 red

giants with the abundance of red giants with announced sub-stellar companions reveals that the same trend with abundance may be present in red giants as for main sequence stars.

1.2 OBSERVATIONS

From spectra of a single object with narrow spectral lines, it is possible to determine small shifts in wavelength compared to a standard. Shifts, observed at different epochs, are interpreted as variation in the radial velocity of the star and can be measured, nowadays, with an accuracy of order $\mathrm{m\,s^{-1}}$ (see for instance Marcy & Butler (2000) and Queloz et al. (2001)). Even though variations measured in this way are not always caused by real variations in the radial velocity of the star, but by phenomena intrinsic to the star, the observed variations will still be called radial velocity variations throughout this thesis.

It is obvious that accurate spectral calibration is crucial. Two different ways are widely used at the moment. Data obtained from both methods are used in this thesis, and, therefore, both methods are explained here.

1.2.1 Iodine cell

In order to measure radial velocity variations of order $\mathrm{m\,s^{-1}}$, an accurate wavelength calibration of the spectrum is needed. Iodine gas at 50° Celsius contains a lot of very well defined narrow spectral lines in the region between 5000 and 6000 Ångstrom. A cell with iodine gas is placed in the light path before stellar light enters the spectrograph, as schematically shown in Figure 1.2, and the narrow iodine lines are superposed onto the stellar spectrum. The observed stellar spectrum with iodine lines can be modelled from a stellar template spectrum without iodine lines and an iodine spectrum. One of the free parameters in this model is a wavelength shift of the observed spectrum with respect to the stellar template spectrum, i.e. the radial velocity variation. This method is described in detail by Marcy & Butler (1992), Valenti et al. (1995) and Butler et al. (1996). Note that with this method the absolute radial velocity is not measured, but only the radial velocity relative to the stellar template is obtained. An iodine spectrum, stellar spectrum without iodine lines and a stellar spectrum with iodine lines are shown in Figure 1.3.

The main advantages of this method are the lower requirements for the spectrograph set-up. Humidity, temperature and pressure are preferably constant, but the iodine lines will also change due to changing circumstances. Therefore, it is possible to correct for these environmental changes. The main drawback is the contamination of the spectrum with iodine lines. The iodine cell reduces the efficiency of the spectrograph due to absorption and makes the best-illuminated part of the spectrum inaccessible for other spectroscopic purposes, such as line profile analysis.

1.2.2 Simultaneous ThAr

With the simultaneous Thorium-Argon (ThAr) method a set-up with two fibres is needed, as shown in Figure 1.4. With this set-up a calibration spectrum can be obtained simultaneously

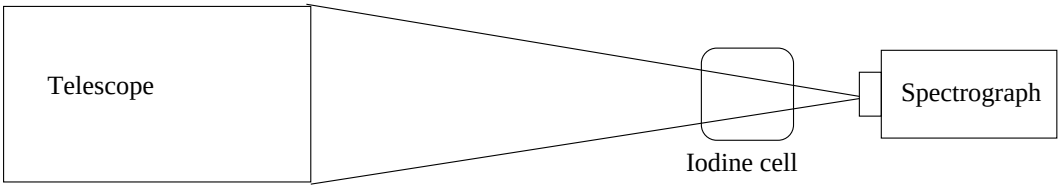

Figure 1.2: A schematic view of the light path from the telescope through the iodine cell to the spectrograph.

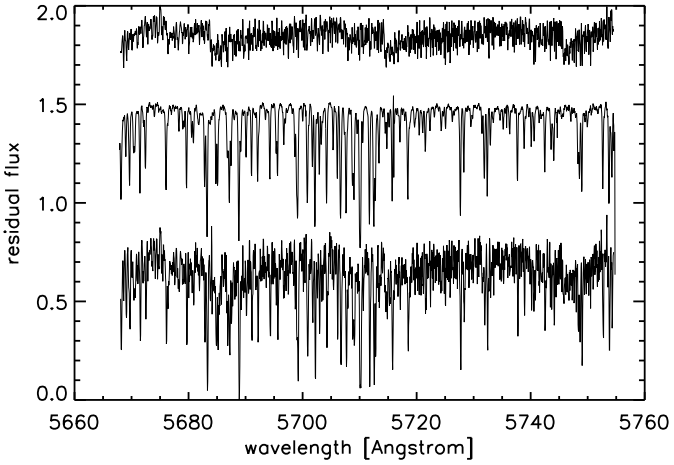

Figure 1.3: An example of an iodine spectrum (top), a stellar template spectrum without iodine lines (middle) and a stellar observation with iodine lines. The spectra are shifted for clarity.

with the observation. This calibration spectrum is displayed between the orders of the échelle spectrograph as shown in Figure 1.5.

With a block-shaped mask selecting suitable spectral lines (Baranne et al. 1996), a cross-correlation profile is constructed. The shift of the centre of this cross-correlation profile is the radial velocity variation of the star. With this method the radial velocity variations and the absolute radial velocity of the star can be obtained.

This method needs a very stable spectrograph, because the stellar observation and calibration do not follow the same light path as with the iodine method, described in the previous subsection. On the other hand, the spectrum is not contaminated and useful for other spectroscopic purposes, such as a line profile analysis.

1.3 OSCILLATIONS

Oscillations are a quasi-direct way to reveal the internal structure of a star. By observing non-radial oscillation modes with different frequencies it is possible to probe the star to different depth. In this way, it is possible to determine, for instance, overshoot parameters in transition regions, such as the edge of the core or between a radiative and turbulent layer. In addition, the frequency separation between different radial modes is proportional to the mean density of the star.

In this section the basic ideas about oscillating stars are described. The description is largely based on the overview paper by Saio (1993) and the textbooks by Cox (1980) and Unno et al.

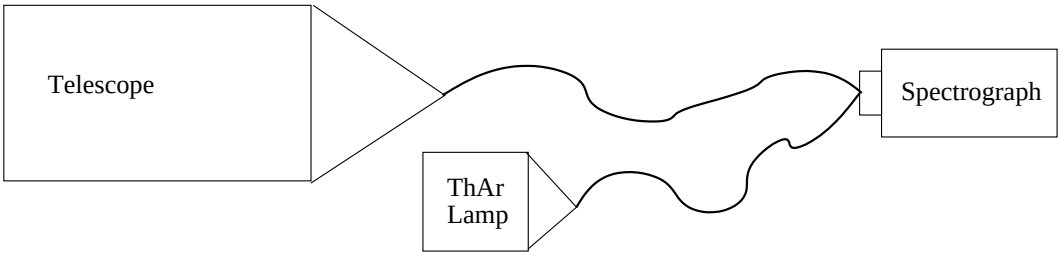

Figure 1.4: A schematic view of the light path from the telescope through a fibre to the spectrograph with simultaneously a Thorium-Argon calibration lamp from a second fibre.

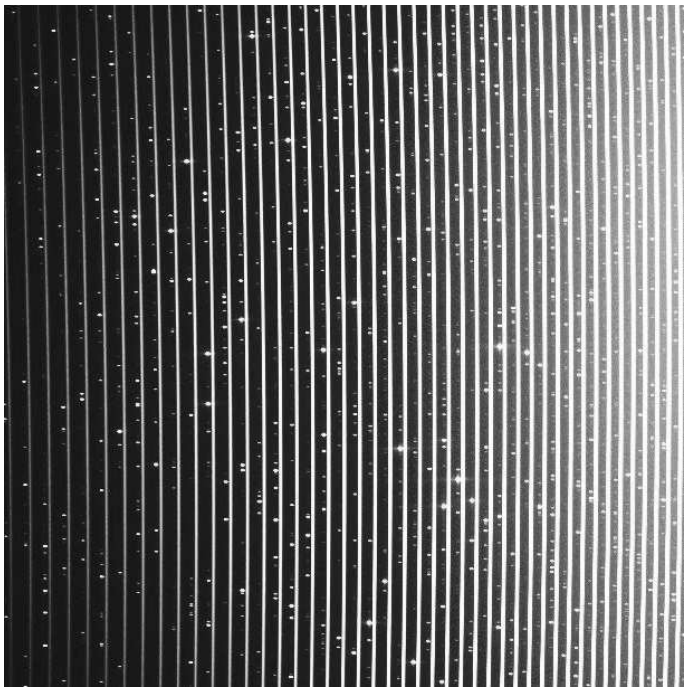

Figure 1.5: Part of a spectrum taken with a simultaneous Thorium-Argon image. The lines are the stellar spectrum, while a Thorium-Argon spectrum is projected in-between the orders of the échelle spectrograph.

(1989). Since stellar oscillations are eigenfunctions of the star, the oscillation frequencies contain information about the internal structure of the star. The basic equations for stellar oscillations are the hydrodynamic equations.

Consider a non-rotating spherically symmetric star without viscosity, magnetic fields or external forces for which the hydrodynamic equations will take the following forms:
Conservation of mass (continuity equation):

$$\frac{\partial \rho}{\partial t} + \bar{\nabla}(\rho \bar{v}) = 0; \tag{1.1}$$

Conservation of momentum:

$$\rho \frac{d\bar{v}}{dt} = -\bar{\nabla} p - \rho \bar{\nabla} \Phi; \tag{1.2}$$

Poisson equation:

$$\bar{\nabla}^2 \Phi = 4\pi G \rho; \tag{1.3}$$

Conservation of energy:

$$T\frac{dS}{dt} = \epsilon - \frac{1}{\rho}\bar{\nabla}\cdot\bar{F}; \tag{1.4}$$

Energy transport:

$$\bar{F} = \bar{F}_{\rm R} + \bar{F}_{\rm C} = -\kappa_{\rm rad}\bar{\nabla}T + \bar{F}_{\rm C} = -\frac{4ac}{3\kappa\rho}T^3\bar{\nabla}T + \bar{F}_{\rm C}. \tag{1.5}$$

In this set of equations, t denotes the time, ρ the mass density, $\bar{v}$ the fluid velocity, p the pressure, Φ the gravitational potential, G the gravitational constant, S the entropy, ϵ the energy production rate per unit mass, $\bar{F}$ the total flux, $\bar{F}_{\rm R}$ the radiative flux, $\bar{F}_{\rm C}$ the convective flux, $\kappa_{\rm rad}$ the radiative opacity, T the temperature, κ the Rosseland opacity, a the radiation constant and c the speed of light.

Convection will only occur when the radiative temperature gradient exceeds the adiabatic temperature gradient:

$$(\frac{d\ln T}{d\ln p})_{\rm rad} = \frac{3}{16\pi acG}\frac{\kappa Lp}{MT^4} > (\frac{\partial\ln T}{\partial\ln p})_S, \tag{1.6}$$

with L and M denoting the (local) luminosity and mass.

An oscillating star is not in equilibrium. The position, density, pressure and temperature vary around its equilibrium state. This can be described with a small perturbation to the hydrodynamic equations mentioned above. As the perturbations are small, a linear approximation is valid and the perturbed hydrodynamic equations take the following form:
Conservation of mass (continuity equation):

$$\frac{\partial\rho'}{\partial t} = -\bar{\nabla}(\rho\bar{v}'); \tag{1.7}$$

Conservation of momentum:

$$\frac{\partial^2\delta\bar{r}}{\partial t^2} = -\frac{\bar{\nabla}p'}{\rho} - \bar{\nabla}\Phi' - \frac{\rho'}{\rho^2}\bar{\nabla}p; \tag{1.8}$$

Poisson equation:

$$\bar{\nabla}^2\Phi' = 4\pi G\rho'; \tag{1.9}$$

Conservation of energy:

$$T\frac{d\delta S}{dt} = \epsilon' + \frac{\rho'}{\rho^2}\bar{\nabla}\cdot\bar{F} - \frac{\bar{\nabla}\cdot\bar{F}'}{\rho}; \tag{1.10}$$

Energy transport:

$$\bar{F}'_{\rm R} = \bar{F}_{\rm R}(3\frac{T'}{T} - \frac{\kappa'}{\kappa} - \frac{\rho'}{\rho}) - \frac{4acT^3}{3\kappa\rho}\bar{\nabla}T', \tag{1.11}$$

with δ denoting the Langrangian perturbation (for a fixed mass element) and a prime denoting the Euler perturbation (at a fixed position) of the respective parameter.

Whenever the oscillation period of the star is much shorter than the thermal timescale, the entropy can not change during the oscillation cycle. In this case one can use the adiabatic approximation, for which $\delta S = 0$. In this approximation the energy equation is decoupled from

the mass and momentum conservation, which leads to the following relation between pressure and density:

$$\frac{\delta\rho}{\rho} = \frac{1}{\Gamma_1}\frac{\delta p}{p}, \tag{1.12}$$

with $\Gamma_1 \equiv (\partial \ln p/\partial \ln \rho)_S$ the adiabatic exponent.

The equations for the perturbations can then be written as a Sturm Liouville problem, which gives rise to an infinite number of eigenvalues, each eigenvalue corresponding to a particular eigenvector $\bar{\xi}$. This can be written symbolically as:

$$-\sigma_{\rm f}^2\bar{\xi} + \mathcal{L}(\bar{\xi}) = 0, \tag{1.13}$$

with $\sigma_{\rm f}$ the eigenfrequency and $\mathcal{L}$ a Hermitian operator. Therefore, all eigenvalues $\sigma_{\rm f}^2$ are real, and eigenfunctions associated with different eigenvalues are orthogonal to each other. As $\sigma_{\rm f}^2$ is real, the temporal behaviour of the adiabatic perturbations is purely oscillatory in case $\sigma_{\rm f}^2 > 0$ or monotonic when $\sigma_{\rm f}^2 < 0$ (dynamical instability).

One can show that the angular dependence of perturbed quantities can be expressed by a single spherical harmonic $Y_\ell^m(\theta,\phi)$. The displacement eigenvector can be written as:

$$\bar{\xi} = [\xi_r\hat{e}_r + \xi_h(\hat{e}_\theta\frac{\partial}{\partial\theta} + \hat{e}_\phi\frac{1}{\sin\theta}\frac{\partial}{\partial\phi})]Y_\ell^m(\theta,\phi)e^{i\sigma_{\rm f}t}, \tag{1.14}$$

with the spherical harmonic $Y_\ell^m(\theta,\phi)$ defined as:

$$Y_\ell^m(\theta,\phi) \equiv \sqrt{\frac{2\ell+1}{4\pi}\frac{(\ell-m)!}{(\ell+m)!}}P_\ell^m(\cos\theta)e^{im\phi}, \tag{1.15}$$

with $P_\ell^m(\cos\theta)$ the associated Legendre function defined as:

$$P_\ell^m(x) \equiv \frac{(-1)^m}{2^\ell\ell!}(1-x^2)^{m/2}\frac{d^{\ell+m}}{dx^{\ell+m}}(x^2-1)^\ell, \tag{1.16}$$

with ℓ and m the angular degree and azimuthal order, respectively. The governing equations can now be reduced to differential equations of the radial order only. In case the Cowling approximation is applied, i.e. omitting Φ', which is a good approximation for higher order modes (high radial order n), the following expressions can be obtained:

$$\frac{1}{r^2}\frac{d}{dr}(r^2\xi_r) - \frac{g}{c_{\rm s}^2}\xi_r + (1-\frac{L_\ell^2}{\sigma_{\rm f}^2})\frac{p'}{\rho c_{\rm s}^2} = 0, \tag{1.17}$$

$$\frac{1}{\rho}\frac{dp'}{dr} + \frac{g}{\rho c_{\rm s}^2}p' + (N^2-\sigma_{\rm f}^2)\xi_r = 0. \tag{1.18}$$

Here g is the local gravitational acceleration, $c_{\rm s}$ is the local speed of sound, L_ℓ is the Lamb frequency and N is the Brunt-Väisälä frequency, respectively. These are defined as follows:

$$c_{\rm s}^2 \equiv \frac{\Gamma_1 p}{\rho}, \tag{1.19}$$

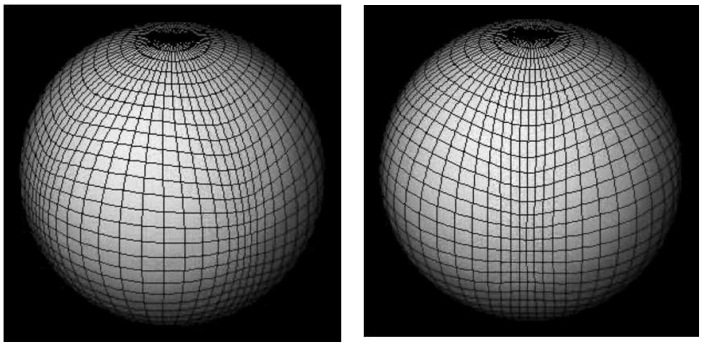

Figure 1.6: Simulation of an oscillating star in 2 different phases of an (ℓ = 4, m = -4) g-mode (Townsend 2004). The lines indicate the nominal boundaries of photospheric fluid elements.

$$L_\ell^2 \equiv \frac{\ell(\ell+1)}{r^2} c_{\rm s}^2, \tag{1.20}$$

$$N^2 \equiv g\left(\frac{1}{\Gamma_1}\frac{d\ln p}{dr} - \frac{d\ln \rho}{dr}\right) = g\left(-\frac{g}{c_{\rm s}^2} - \frac{d\ln \rho}{dr}\right). \tag{1.21}$$

Two types of oscillations are possible. Pressure (acoustic) or p-mode oscillations are propagating in case $\sigma_{\rm f}^2 > L_\ell^2, N^2$ and gravity or g-mode oscillations are propagating in case $\sigma_{\rm f}^2 < L_\ell^2, N^2$. Two different phases of an (ℓ = 4, m = -4) g-mode are shown in Figure 1.6. The restoring force for p-modes is pressure while the restoring force for g-modes is the buoyancy force. In most cases, the frequency range for p-modes is well separated from, and higher than, the frequency range of the g-modes. The propagation zone of the p-modes is in the outer envelope of the star, while the propagation zone of the g-modes is in the vicinity of the core. As the central concentration of a star increases with evolution, N^2 increases and hence the frequencies of the g-modes increase. Meanwhile the p-mode frequencies decrease as the mean density in the outer envelope decreases. When the frequency of a g-mode approaches a p-mode frequency, the two frequencies undergo an 'avoided crossing', where they exchange physical nature. At the avoided crossing the modes get a mixed character.

1.3.1 Excitation mechanism

The p-modes and g-modes are excited by different mechanisms. In some circumstances g-mode oscillations could be excited in the vicinity of the stellar core by the so-called ϵ-mechanism. In case of compression, the temperature, and hence the nuclear energy generation rate, are higher than in equilibrium, and matter gains thermal energy. Therefore, the amplitude of the expansion following this contraction will be larger than the previous one. During expansion the nuclear energy generation rate is lower than in equilibrium and hence matter loses thermal energy. Therefore, to regain this energy, the amplitude of the next contraction will increase. The amplitude of the oscillations will remain small near the centre because of the node at the centre of the star. In red giants, the amplitudes of g-modes are small at the surface and these will most likely not be observable.

P-mode oscillations can become excited by the so-called κ-mechanism. During compression, the opacity increases in partial ionisation zones, because part of the energy, released by the core, produces further ionisation rather than raising the temperature of the gas. As a result, the radiative luminosity is blocked and thus this zone gains energy during this phase. This energy

will be lost again during expansion when the opacity decreases again. Most stars in the classical instability strip oscillate due to this mechanism.

Solar-like oscillations (also pressure mode oscillations) are oscillations stochastically excited by turbulent convection near the surface. Due to the stochastic nature these oscillations undergo damping and re-excitation. It is expected that all stars cool enough to have an outer convective zone will oscillate in this manner. This presumably includes all stars from roughly the cool edge of the instability strip out to the red giants.

1.3.2 Asymptotic relation

Mode frequencies ($\nu_{n,\ell}$) for low degree p-mode oscillations are approximated reasonably well by the following asymptotic relation (Tassoul 1980):

$$\nu_{n,\ell} = \Delta\nu(n + \frac{1}{2}\ell + \epsilon_{\rm c}) - \ell(\ell+1)\frac{1}{6}\delta\nu_{02}, \tag{1.22}$$

with n the radial order, ℓ the angular degree, m the azimuthal order and $\epsilon_{\rm c}$ a constant sensitive to the surface layers (Bedding & Kjeldsen 2003). The quantity $\Delta\nu$ denotes the so-called large separation, i.e. the separation between different radial orders n with the same angular degree ℓ. It provides the inverse of the sound travel time directly through the star, i.e.

$$\Delta\nu \simeq (2\int_0^R \frac{dr}{c_{\rm s}})^{-1}. \tag{1.23}$$

Finally, $\delta\nu_{02}$ denotes the so-called small separation. It is defined as the frequency spacing between adjacent modes with $\ell = 0$ and $\ell = 2$, and is sensitive to the sound speed near the core.

1.3.3 Scaling relations

Kjeldsen & Bedding (1995) developed some scaling relations to estimate the velocity amplitudes of solar-like oscillations in different stars. They found that oscillation velocity amplitudes ($v_{\rm osc}$) scale directly with the light-to-mass ratio ($L/M_\star$) of the star, i.e.

$$v_{\rm osc} \propto L/M_\star. \tag{1.24}$$

With $g \propto M_\star/R^2$ and $L \propto R^2T_{eff}^4$ (R is the stellar radius and $T_{\rm eff}$ is the effective temperature) this leads to:

$$v_{\rm osc} \propto T_{\rm eff}^4/g = F_{\rm C}/g = F_{\rm C}H_p/T, \tag{1.25}$$

where the radiative surface flux ($\sigma_{\rm b}T_{\rm eff}^4$) is set equal to the convective flux ($F_{\rm C}$), because convection is the dominant mechanism for energy transport in the convection zone. Furthermore, $H_p \propto T/g$ is the pressure scale height, with T the mean local temperature. This equation shows that the convective flux, the scale height and the mean local temperature determine the velocity amplitude of oscillations.

With the adiabatic speed of sound $c_{\rm s}^2 \propto T$ and $\langle T\rangle \propto M_\star/R$ ($\langle T\rangle$ the average internal temperature), equation (1.23) can be adjusted to become:

$$\Delta\nu \propto (M_\star/R^3)^{1/2}. \tag{1.26}$$

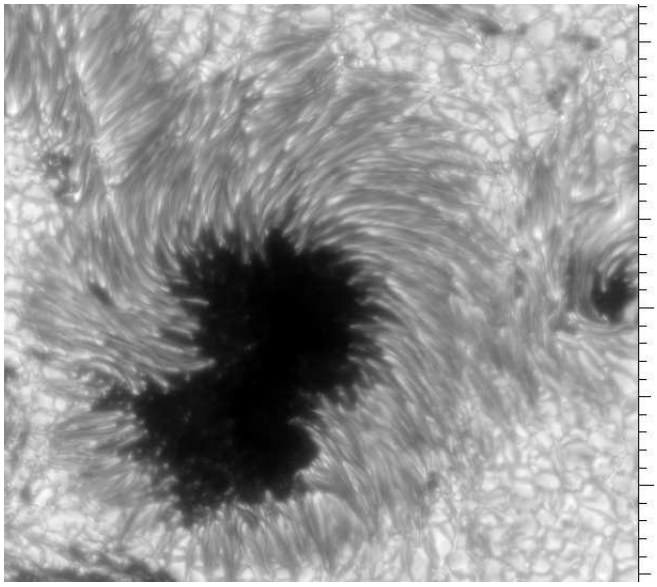

Figure 1.7: A sunspot with the umbra, plain dark patch and penumbra, filamented part surrounding the umbra. The structures outside the sunspot are granules, fluctuations caused by the turbulence in the outer atmosphere of the sun. The distance between two ticks, indicated at the right, is 1000 km.

Equation (1.26) can be interpreted as follows: the primary splitting (large separation) is directly proportional to the mean density of the star.

There is a fundamental maximum frequency for oscillations set by the acoustic cut-off frequency $\nu_{\rm ac} = c_{\rm s}/2H_p = \Gamma_1 g/c_{\rm s}$ (Christensen-Dalsgaard 2004). Like the frequency of maximum power, the acoustic cut-off frequency defines a typical dynamical timescale for the atmosphere. Therefore, it has been argued that these frequencies should be related. With $\nu_{\rm max} \propto c_{\rm s}/H_p$ and $T \propto T_{\rm eff}$ (we consider the oscillations in the photosphere, where the mean local temperature is close to the effective temperature), it is found that the frequency of maximum power is:

$$\nu_{\rm max} \propto \frac{M_\star}{R^2\sqrt{T_{\rm eff}}}. \tag{1.27}$$

This shows that stars with larger radii (giants) have their frequency with maximum power at longer periods of the order of hours, which relaxes the observing constraints compared to the ones for smaller stars (dwarfs).

1.4 STARSPOTS

Starspots are dark (or light) patches on the surface of a star, with a lower (or higher) temperature compared to the surrounding areas on the star, and strong (kG) magnetic fields. The best-studied starspots are the ones on the sun, called sunspots. These have a dark inner region, without any structure, the umbra, and an edge consisting of filaments, the penumbra. An image of a sunspot is shown in Figure 1.7. Lifetimes of relatively small spots are proportional to their sizes, while lifetimes of relatively large spots are possibly limited by the shear caused by surface differential rotation. However, in some cases, large spots are seen to survive for many years, despite differential rotation (Berdyugina 2005).

One of the most striking regularities of the 11 year sunspot cycle is that the polarities of sunspot pairs reverse from one sunspot cycle to the next, while remaining antisymmetric about

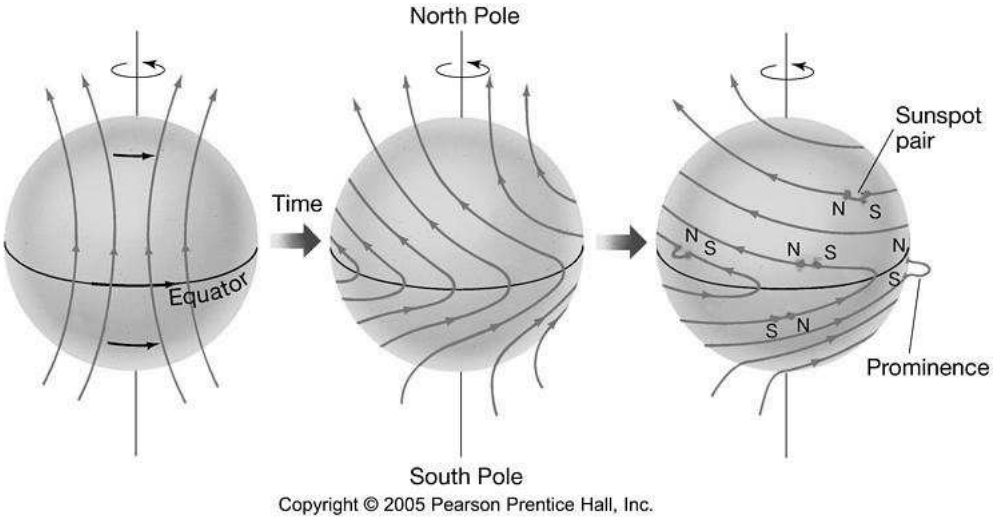

Figure 1.8: The influence of rotation on the magnetic field in a star. Left: poloidal magnetic field. Centre: differential rotation drags the ”frozen in” magnetic field lines around the star, converting the poloidal field into a toroidal field. Right: turbulent convection twists the field lines into magnetic ropes, causing them to rise to the surface as spots, the polarity of the leading spot corresponds to the original polarity of the poloidal field (Chaisson & McMillan 2005).

the equatorial plane at any given time. These regularities indicate that the solar magnetic field is present on a large spatial scale and evolves coherently spatially and temporally. At the moment, the general idea is that the solar magnetic cycle is a dynamo process involving the transformation of a poloidal magnetic field into a toroidal magnetic field and subsequent conversion of the produced toroidal field into a poloidal field of polarity opposite to the earlier one, and so on (Dikpati & Charbonneau 1999). Spots occur in the transition from a toroidal magnetic field to a poloidal magnetic field.

In the sun, a strong, large-scale toroidal field axi-symmetric around the equatorial plane is induced via the shearing action of the axi-symmetric differential rotation on a pre-existing dipolar field. A poloidal field is regenerated by twists in the field lines due to turbulent convection, creating regions of intense magnetic fields, so-called magnetic ropes. Buoyancy produced by magnetic pressure causes the ropes to rise to the surface, appearing as spots, see Figures 1.8 and 1.9. Initially, the twisting of field lines occurs at higher latitudes. As the differential rotation continues to drag the field lines along, successive groups of spots migrate toward the equator, where magnetic field reconnection re-establishes the poloidal field, but with reversed polarity.

Spot phenomena are also observed on cool stars with outer convection zones and are presumably caused by the same phenomena as sunspots.

1.5 SUB-STELLAR COMPANIONS

A companion around a star can be looked upon as a two-body problem with the centre of mass in-between them. According to Newton’s third law of reaction, an orbit of the companion induced by the gravitational force between the companion and the star will induce the star to

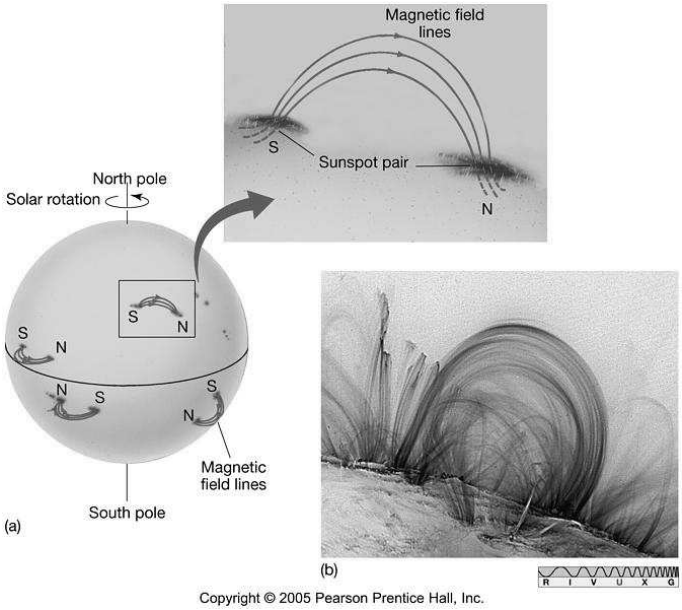

Figure 1.9: Close up of starspots, as shown in the left panel of Figure 1.8 (Chaisson & McMillan 2005).

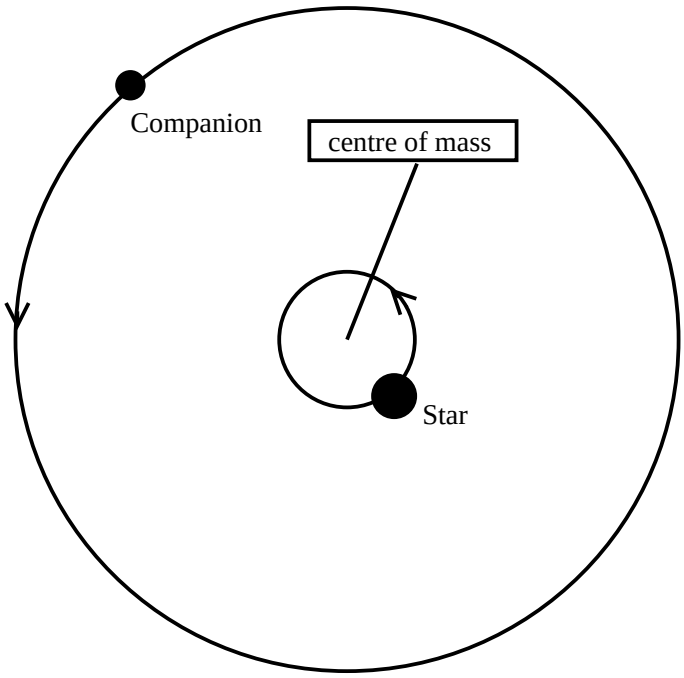

Figure 1.10: A sub-stellar companion of planetary mass orbiting a star. The orbits of both the companion and the star are indicated.

orbit with equal and opposite force. The relative distances from the centre of mass are inversely proportional to the respective masses. As the orbital period of both star and companion are equal, the velocities are also inversely proportional to the respective masses.

The reflex motion of the star in the line of sight, i.e. variation of the radial velocity, can be measured from the wavelength shift in time-sampled spectra of the star. From Kepler's third law one can derive the radial velocity variation v as a function of the true anomaly $\nu_{\rm a}$ (angle from perihelium) to be:

$$v = K(e\cos(\omega) + cos(\omega + \nu_{\rm a})), \tag{1.28}$$

$$K = \frac{2\pi a \sin i}{P\sqrt{1-e^2}} = (\frac{2\pi G}{P})^{\frac{1}{3}} \frac{m_{\rm c}\sin i}{(m_{\rm c}+M_\star)^{\frac{2}{3}}} \frac{1}{\sqrt{1-e^2}}, \tag{1.29}$$

with P the period, e the eccentricity, a the semi-major axis, $m_{\rm c}$ the mass of the companion, $M_\star$ the mass of the star, ω the periastron length, G the gravitational constant, and i the angle of inclination.

In order to calculate the radial velocity variation as a function of time one needs to compute the true anomaly from the mean anomaly $M_{\rm a}$ and eccentric anomaly $E_{\rm a}$,

$$M_{\rm a} = \frac{2\pi}{P}(t - T_{\rm p}) = E_{\rm a} - e\sin E_{\rm a}, \tag{1.30}$$

$$\tan\nu_{\rm a} = \frac{\sqrt{1-e^2}\sin E_{\rm a}}{\cos E_{\rm a} - e}, \tag{1.31}$$

with t epoch of observation and $T_{\rm p}$ periastron time.

The first sub-stellar companion around a star was discovered in 1994 (Mayor & Queloz 1995) and now more than 200 sub-stellar companions are discovered[1]. Most companions are discovered by radial velocity observations of the reflex motion of the parent star and are so-called hot Jupiters. These hot Jupiters are gas giants in orbits relatively close to their parent stars, often with large eccentricities. These discoveries initiated a great revolution in sub-stellar companion searches and formation theory, mainly because the sub-stellar companions discovered around other stars are considerably different from what is known from our solar system.

1.6 WHY CAN OSCILLATIONS, SPOTS AND COMPANIONS BE OBSERVED AS RADIAL VELOCITY VARIATIONS?

The three phenomena introduced in the previous sections, oscillations, starspots and companions, are not necessarily and not likely connected. They can occur independent from each other. They are treated here because all three can cause variations in the observed radial velocity of a star. Radial velocities are measured from the shift in wavelength of a spectrum compared to a certain standard. In case of a companion, stars indeed have a varying velocity in the radial direction due to the reflex motion of the star induced by the companion. On the other hand, oscillations and spots are phenomena intrinsic to the star, which do not really change the velocity in radial direction, but only mimic it.

[1]For updated information on sub-stellar companions see http://exoplanet.eu and http://exoplanets.org.

A spectrum of an unresolved star can be looked upon as the resultant of spectra formed at each visible surface element. In case the star is oscillating, parts of the star are slightly blue shifted, while others are slightly red shifted. At some epoch, the largest fraction of the visible surface of the star is blue shifted, and the blue part of a spectral line will be enhanced compared to the red part of a spectral line. At a later epoch, the largest part of the star may be red shifted, and, thus, the spectral line is enhanced on the red side, compared to the blue side. This mimics radial velocity variation. These variations can also be visible photometrically.

In case of a dark (light) spot on the surface, some surface elements contribute less (more) to the overall spectrum and depending on the position of the spot a spectral line is reduced (enhanced) on either the red or blue side. At a later epoch, as the star rotated and the spot is observed at a different position, another part of the spectral line is reduced (enhanced). This variation in the shape of the spectral line can also mimic radial velocity variations. Spots also cause photometric variations as they rotate in and out of view, or emerge and disappear, depending on spot lifetimes and the rotational period of the star.

For stars with an intrinsic mechanism causing the observed radial velocity variations the shape of the spectral lines will change, due to the changing contributions of each surface element to the total spectrum. This is in contrast with the case of a companion where the whole spectrum will shift, but retain its shape (except in case of a transit, which provides a spot like variation). Therefore, line profile analysis can be used to discriminate between phenomena intrinsic to the star and a companion orbiting the star.

1.7 LINE PROFILE ANALYSIS

Different line shape diagnostics are developed, and will be described here. Following the diagnostic descriptions some examples of each diagnostic in case of companions, oscillations and spots are shown.

1.7.1 Moments

The description of a line profile in terms of its moments was first introduced by Balona (1986) and further developed by Aerts et al. (1992). The nth moment of a line profile is defined as:

$$< v^n > \equiv \frac{\int_{-\infty}^{+\infty} v^n p(v) dv}{\int_{-\infty}^{+\infty} p(v) dv} = \frac{\int_{-\infty}^{+\infty} v^n f(v) * g(v) dv}{\int_{-\infty}^{+\infty} f(v) * g(v) dv}, \tag{1.32}$$

with $p(v)$ the convolution of an intrinsic profile, here assumed to be a Gaussian ($g(v)$) with the flux in the direction of the observer ($f(v)$), integrated over the visible stellar surface, and v the component of the total (oscillation and rotation) velocity field in the line of sight.

In principle, all information contained in a line profile can be reconstructed from the entire series of moments. In practice, we consider only the first three moments, which are connected to a specific property of a line profile.

- $\langle \mathrm{v} \rangle$ is the centroid of a line profile;

- $\langle \mathrm{v}^2 \rangle$ is related to the width of a line profile;
- $\langle \mathrm{v}^3 \rangle$ is a measure of the skewness of a line profile.

The moments are fully described in terms of oscillation theory, but can also be used to distinguish between different mechanisms causing line shape variations. Moments show different behaviour in the presence of spots, companions or oscillations. Comparison with simulations can reveal the origin of the variations in moments and thus of the radial velocity variations.

In case of oscillations, the observed moments can be compared with their theoretical expectations derived from oscillation theory (Aerts et al. 1992). Moments are a function of wavenumbers ℓ, m, inclination angle i, oscillation velocity amplitude $\upsilon_{\rm osc}$, projected rotational velocity $\upsilon \sin i$ and intrinsic width of the line profile σ. A comparison can be performed objectively with a discriminant (Aerts et al. (1992), Aerts (1996), Briquet & Aerts (2003)), which selects the most likely set of parameters $(\ell, m, i, \upsilon_{\rm osc}, \upsilon \sin i, \sigma)$. Due to the fact that several combinations of wavenumbers and velocity parameters result in almost the same line profile variation, the discriminant possibly gives a number of likely sets of parameters. Other diagnostics, described in the following subsections, can be used to select the best set of parameters.

Oscillation modes can only be identified from the moments in case the amplitude of the oscillation is larger than about half the equivalent width of the spectral line (Chapter 2 of this thesis). In addition, one has to take into account that it is possible that a star is looked upon in such a way that the contribution to $\langle \mathrm{v} \rangle$ of each point on the stellar disk exactly cancels out the contribution of another point on the stellar disk and no effect can be observed. Inclination angles for which this occurs are called inclination angles of complete cancellation (IACC) (Chadid et al. 2001).

1.7.2 Amplitude and phase distribution

In case a frequency of either the first moment or the radial velocity variation is known, amplitude and phase distributions across a line profile can be constructed. This is done by fitting a harmonic at each velocity point through the residual fluxes of the line profiles obtained at different times. As the frequency is known, an amplitude and phase can be obtained at each velocity point. In Figures 1.11 and 1.12 this is shown schematically for a radial mode ($\ell = 0$, $m = 0$) and a non-radial mode ($\ell = 2$, $m = 2$), respectively. Comparison between amplitude and phase distributions obtained from observations, and distributions obtained from simulations can reveal the origin of the mechanism(s) inducing the observed radial velocity variations.

1.7.3 Line bisector

A line bisector is a measure of the centre between the red and blue wing of the spectral line at each residual flux, as shown in Figure 1.13. In case of a fully symmetric line the line bisector will be vertical. Most of the time this is not the case and the line bisector will have a ”C” shape, which is indicative of the type of star at hand (Gray 2005). In case the spectrum is shifted due to a companion, the shape of the bisector does not change. However, in case of intrinsic activity in the star, such as spots or oscillations, the shape of the bisector changes over time. A parameter

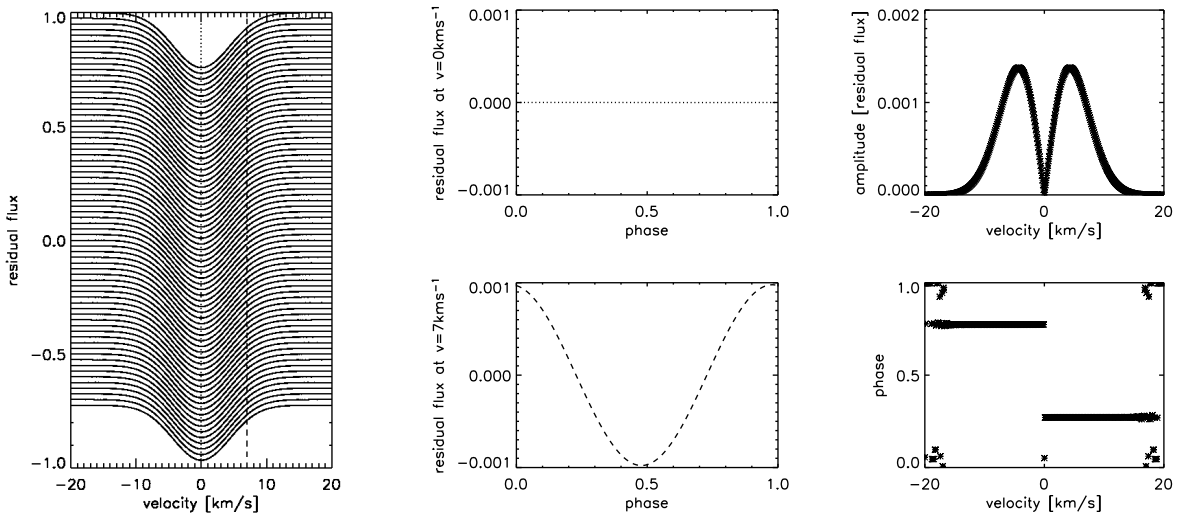

Figure 1.11: Schematic representation of the amplitude distribution across a line profile for simulated data with $(\ell, m) = (0, 0)$, an amplitude of the oscillation velocity of 0.04 km s^{-1}, an inclination angle of $35°$, and intrinsic line width of 4 km s^{-1} and a $v \sin i$ of 3.5 km s^{-1}. Left: profiles obtained at different times are shown with an arbitrary flux shift. The dashed and dotted lines indicate the two velocity values at which the harmonic fits, shown in the two centre panels, are obtained. Centre top: harmonic fit at the centre of the profiles. Centre bottom: harmonic fit at a wing of the profiles. Right top: amplitude across the whole profile. Right bottom: phase across the whole profile (Hekker et al. 2006).

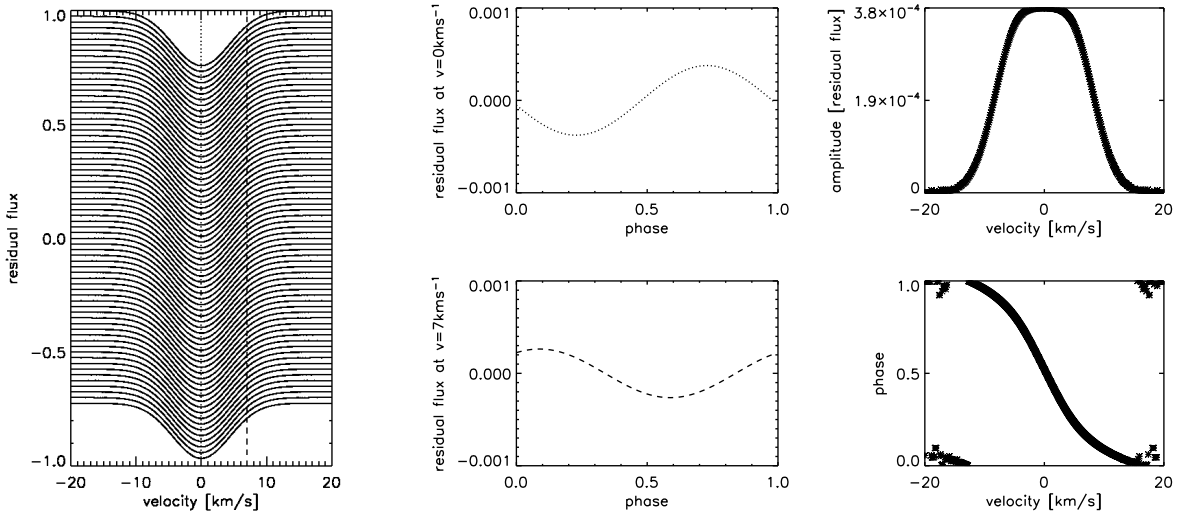

Figure 1.12: Schematic representation of the amplitude distribution across a line profile for simulated data with $(\ell, m) = (2, 2)$, an amplitude of the oscillation velocity of 0.04 km s^{-1}, an inclination angle of $35°$, and intrinsic line width of 4 km s^{-1} and a $v \sin i$ of 3.5 km s^{-1}. Left: Profiles obtained at different times are shown with an arbitrary flux shift. The dashed and dotted lines indicate the two velocity values at which the harmonic fits, shown in the two centre panels, are obtained. Centre top: harmonic fit at the centre of the profiles. Centre bottom: harmonic fit at a wing of the profiles. Right top: amplitude across the whole profile. Right bottom: phase across the whole profile (Hekker et al. 2006).

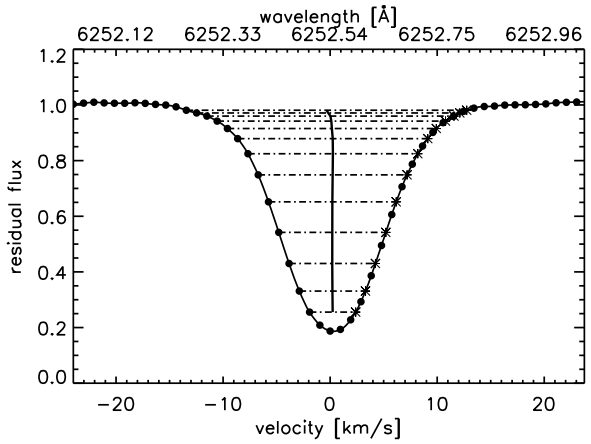

Figure 1.13: A line profile with the line bisector. The line bisector is amplified by a factor of ten to show the small deviations from the core of the line.

often used is the bisector velocity span, which is defined as the horizontal distance between the bisector positions at fractional flux levels in the top and bottom part of the line profile.

1.7.4 Line residual

A time average of a single spectral line can be determined from spectra taken at different epochs. Residuals from this averaged line at each observation epoch can reveal a mechanism inducing radial velocity variations.

1.7.5 Examples

In this section, four spectral line diagnostics, explained in the previous sections, are applied to simulated spectral lines influenced by an oscillation, a companion or a spot. The simulated oscillation and spot are large, while the companion effect is exaggerated by a factor of ten for visual purposes. These examples are meant to show differences in behaviour of the four spectral line diagnostics in the presence of different mechanisms inducing radial velocity variations.

In Figure 1.14 eight profiles, covering a full period of an oscillation with mode $\ell = 1$ and $m = 1$, are shown with an arbitrary flux offset. The oscillation velocity $v_{\rm osc}$ is 10 km s^{-1}, the inclination angle i is 50° and the rotational velocity $v \sin i$ is 10 km s^{-1}. Figure 1.15 shows the results from the moment analysis (left), bisector (centre), amplitude and phase distributions and residuals (right). Note that the bisectors also experience a displacement. They are plotted on top of each other for visual purposes and because this displacement is very hard to measure in real data. The same diagnostics, as just described, are shown in Figures 1.16 and 1.17 for the case where the spectral lines are shifted according to their first moment values to the laboratory wavelength.

Figure 1.18 shows eight lines, with an arbitrary flux offset, covering a full circular orbit of a companion with a period of 305 days, and a companion mass $m \sin i = 18.7$ M$_{\rm Jup}$ around a 2 solar mass star. The velocity shift is enlarged by a factor of ten for visual purposes. Results of the different line shape analyses are shown in Figure 1.19. In Figures 1.20 and 1.21 the spectral

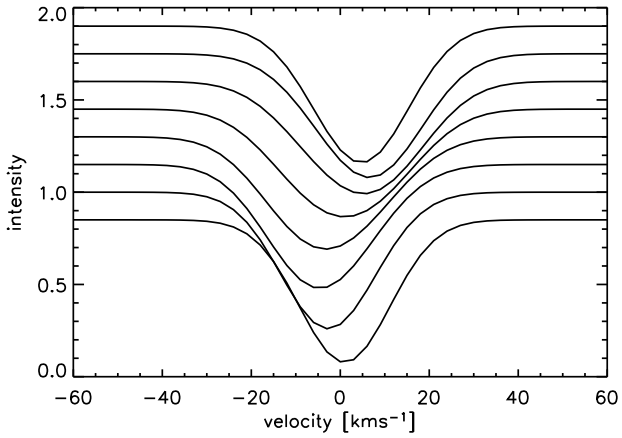

Figure 1.14: Eight line profiles with an arbitrary flux offset covering a full period of an oscillation mode with $\ell = 1$ and $m = 1$. The simulations are performed with an oscillation velocity amplitude $v_{\rm osc}$ of 10 km s^{-1}, an inclination angle of 50° and a rotational velocity $v \sin i$ of 10 km s^{-1}.

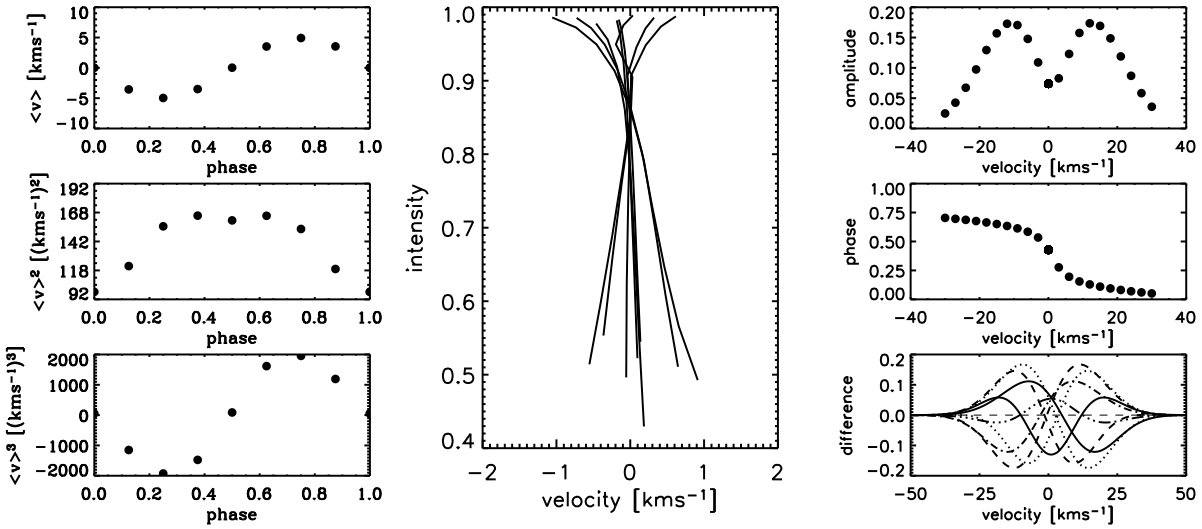

Figure 1.15: Four line shape diagnostics for the line profiles shown in Figure 1.14. Left: moments are shown as a function of phase. The top plot shows the first moment $\langle \mathrm{v} \rangle$ in km s^{-1}, the middle plot the second moment $\langle \mathrm{v}^2 \rangle$ in (km s^{-1})^2 and the third moment $\langle \mathrm{v}^3 \rangle$ in (km s^{-1})^3 is shown at the bottom. Centre: bisectors for all eight profiles, shifted on top of each other, are shown in a residual flux vs. velocity plot. Right: amplitude (top) and phase (middle) distributions are shown as a function of velocity across the line profiles. Residuals from an averaged line profile are shown as a function of velocity in the bottom panel.

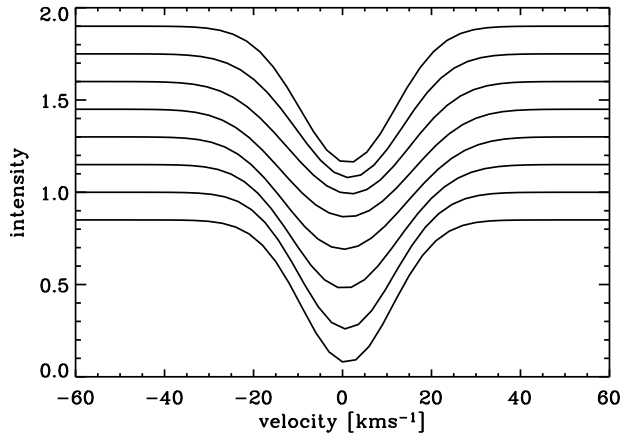

Figure 1.16: Same as Figure 1.14, but now for the case where the lines are shifted according to the first moment value (see text).

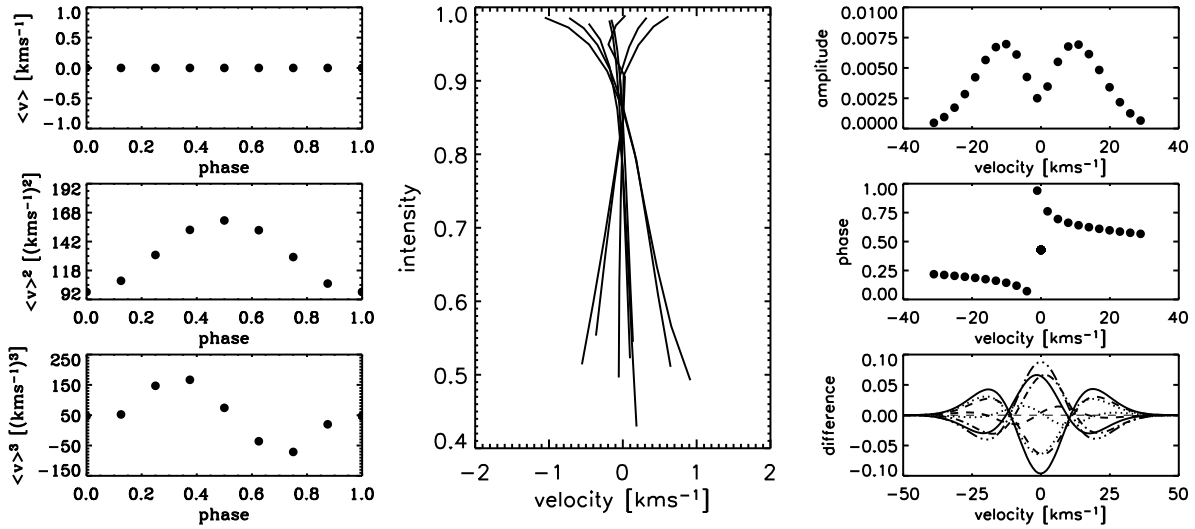

Figure 1.17: Same as Figure 1.15, but now for the case where the lines are shifted according to the first moment value.

lines and diagnostics are shown in case the lines are shifted according to the first moment value to the laboratory wavelength.

Eight profiles covering one rotation period of a star with a single spot on the equator are shown in Figure 1.22 with an arbitrary flux offset. The star is seen from an inclination angle of 50° and the spot has a radius of 45° and 0.8 relative flux. Line shape diagnostics are shown in Figure 1.23. Note that the bisectors do not show a displacement in this case. In Figures 1.24 and 1.25 the spectral lines and diagnostics are shown in case the lines are shifted according to their first moment value to the laboratory wavelength of the spectral line.

From these examples, it becomes apparent that distinguishing between intrinsic stellar features and a companion is a first step. In case the line profiles are shifted to the laboratory wavelength, none of the line shape diagnostics show variations in the presence of a companion, while they do for spots and oscillations. A more thorough analysis is needed to distinguish between oscillations and spots. The examples shown are not comparable in radial velocity am-

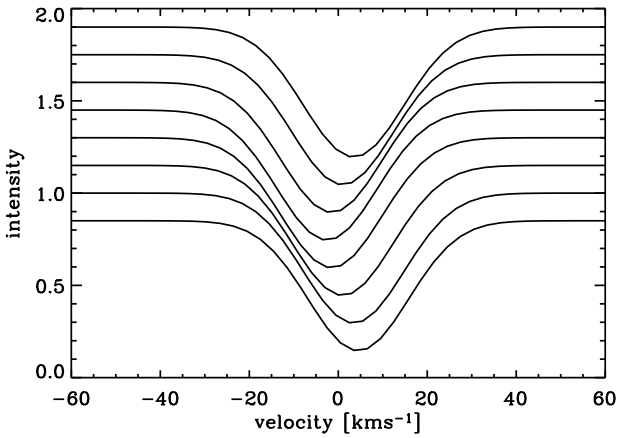

Figure 1.18: Eight line profiles with an arbitrary flux offset, covering a full circular orbit of a companion with a period of 305 days, and a companion mass $m \sin i = 18.7$ $\mathrm{M_{Jup}}$ around a 2 solar mass star. The velocity shift is enlarged by a factor of ten for visual purposes.

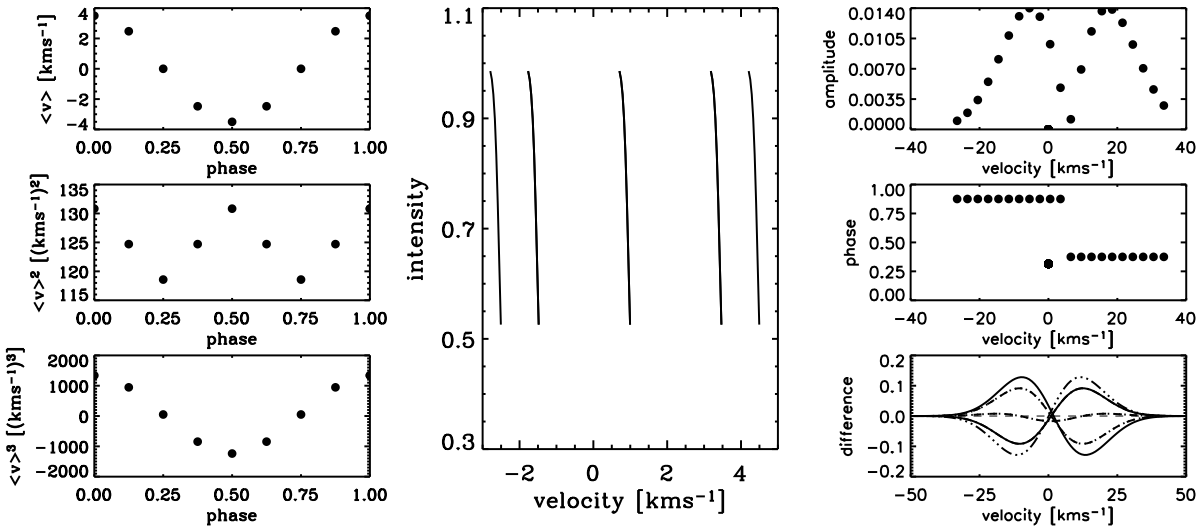

Figure 1.19: Four line shape diagnostics for the line profiles shown in Figure 1.18. Left: moments are shown as a function of phase. The top plot shows the first moment $\langle \mathrm{v} \rangle$ in $\mathrm{km\,s^{-1}}$, the middle plot the second moment $\langle \mathrm{v}^2 \rangle$ in $(\mathrm{km\,s^{-1}})^2$ and the third moment $\langle \mathrm{v}^3 \rangle$ in $(\mathrm{km\,s^{-1}})^3$ is shown at the bottom. Centre: bisectors for all eight profiles are shown in a residual flux vs. velocity plot. Right: amplitude (top) and phase (middle) distributions are shown as a function of velocity across the line profiles. Residuals from an averaged line profile as a function of velocity are shown in the bottom panel.

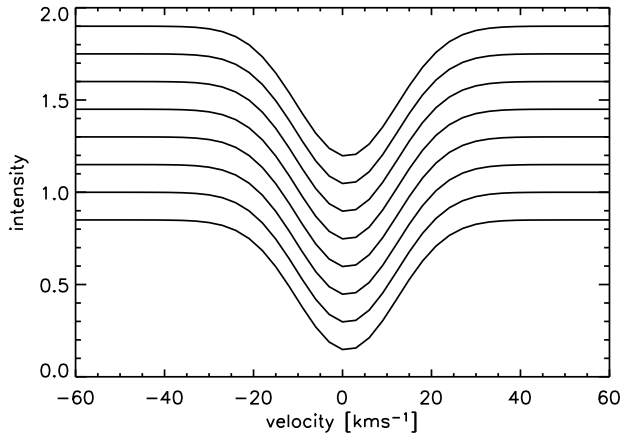

Figure 1.20: Same as Figure 1.18, but now for the case where the lines are shifted according to the first moment value.

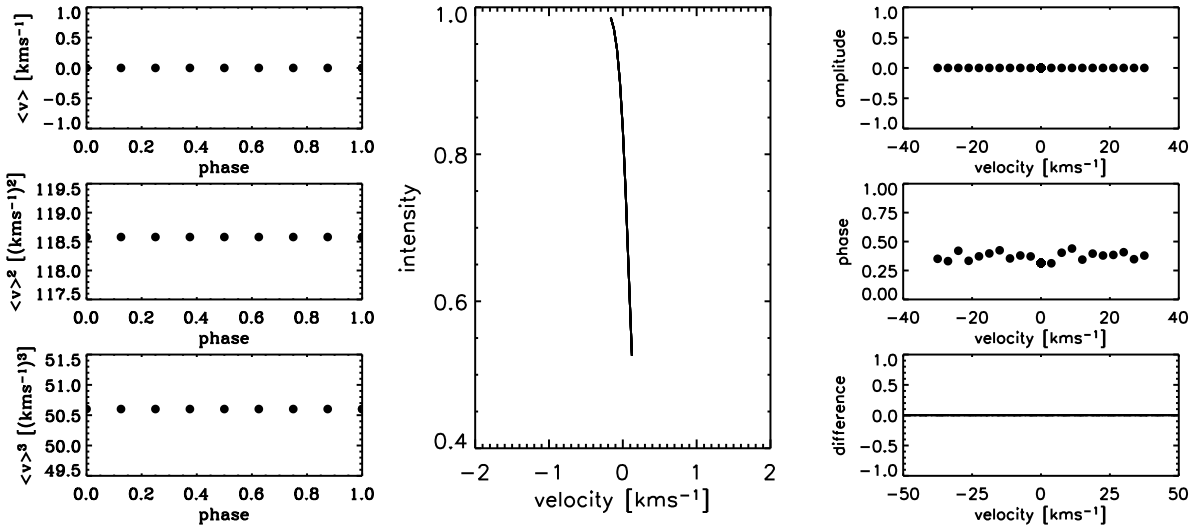

Figure 1.21: Same as Figure 1.19, but now for the case where the lines are shifted according to the first moment value.

plitude. However, it is apparent that the amplitudes of the second and third moment only differ by a factor of two in case of a spot, while they differ by nearly a factor of thousand in case of $\ell = 1$, $m = 1$ oscillations. Furthermore, the shape of the amplitude and phase distributions differs significantly for spots and oscillations. The behaviour of the diagnostics changes for different oscillation modes and different spot coverage. Therefore, simulations are needed to reveal the nature of the feature causing the variation in a spectral line.

1.8 THIS THESIS

In this thesis I will investigate radial velocity variations in red giant stars and study mechanisms, e.g. oscillations, starspots and sub-stellar companions, possibly causing these variations.

In Chapter 2 of this thesis, oscillation modes of four red (sub)giants, with known solar-like oscillations, are investigated. Data from the CORALIE spectrograph mounted on the Swiss

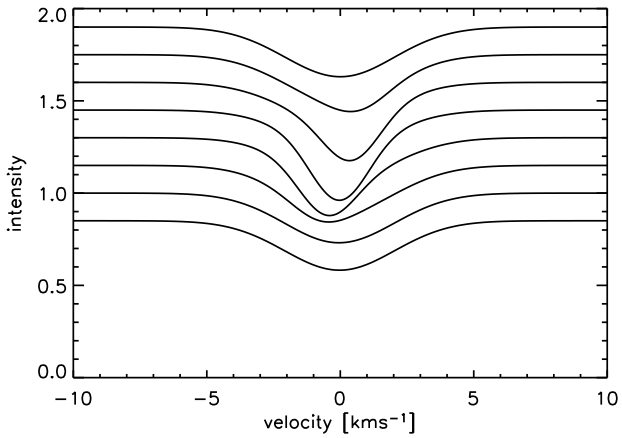

Figure 1.22: Eight line profiles with an arbitrary flux offset covering one rotation period of a star with a single spot on the equator. The star is seen from an inclination angle of 50° and the spot has a radius of 45° and 0.8 relative flux.

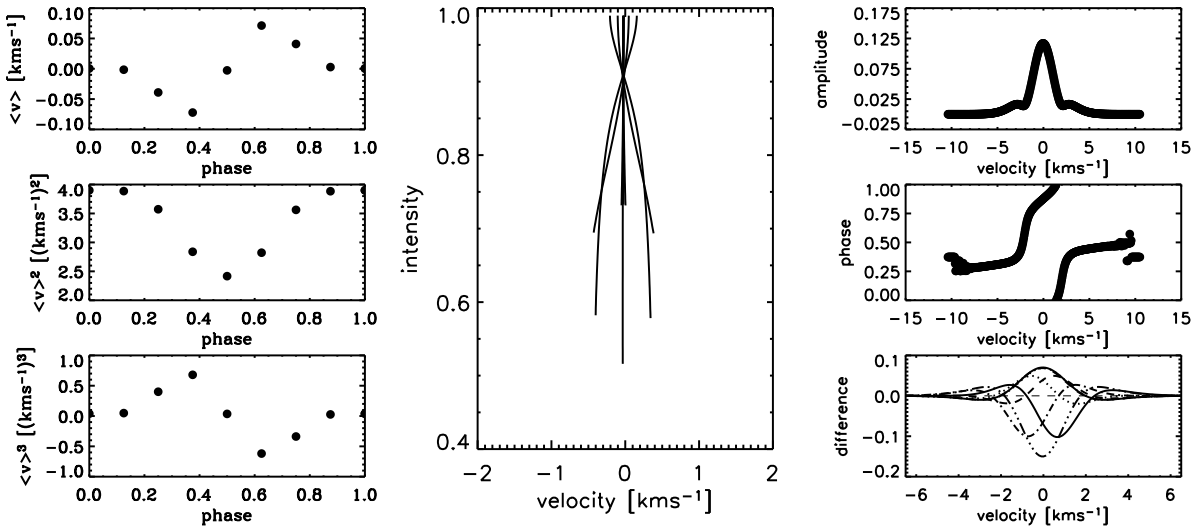

Figure 1.23: Four line shape diagnostics for the line profiles shown in Figure 1.22. Left: moments are shown as a function of phase. The top plot shows the first moment $\langle \mathrm{v} \rangle$ in km s^{-1}, the middle plot the second moment $\langle \mathrm{v}^2 \rangle$ in (km s^{-1})^2 and the third moment $\langle \mathrm{v}^3 \rangle$ in (km s^{-1})^3 is shown at the bottom. Centre: bisectors for all eight profiles are shown in a residual flux vs. velocity plot. Right: amplitude (top) and phase (middle) distributions are shown as a function of velocity across the line profiles. Residuals from an averaged line profile are shown as a function of velocity in the bottom panel.

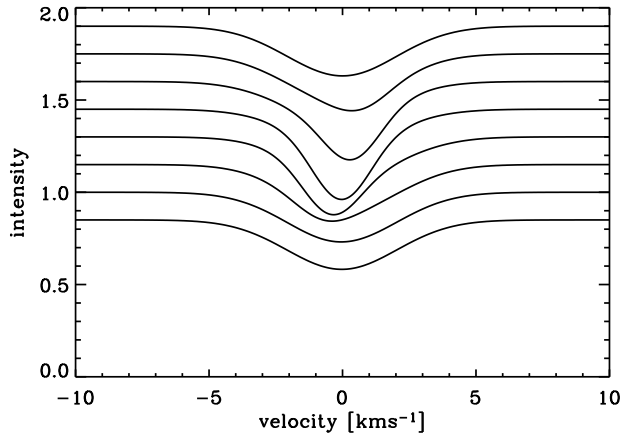

Figure 1.24: Same as Figure 1.22, but now for the case where the lines are shifted according to the first moment value.

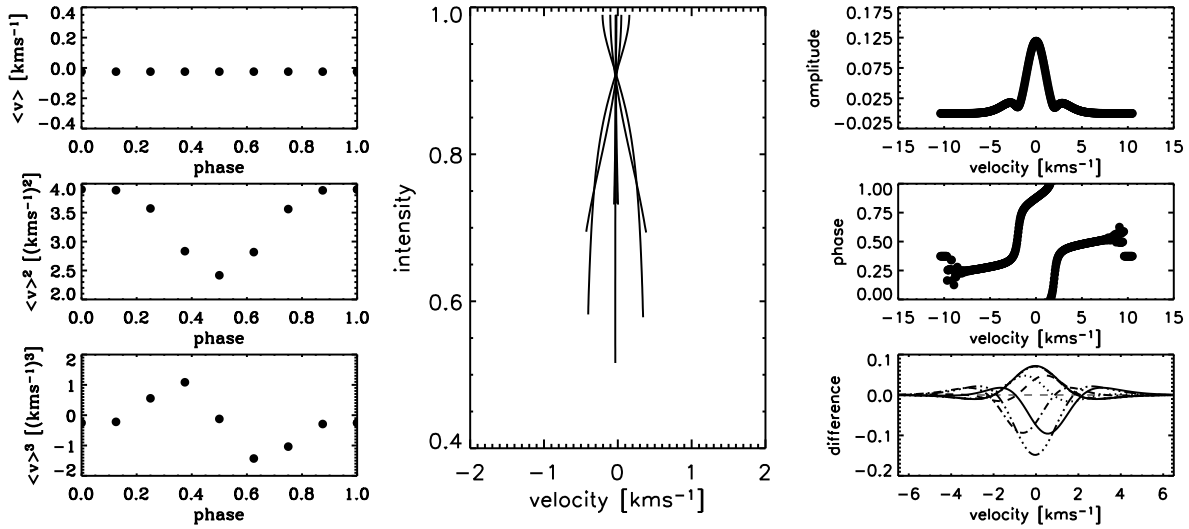

Figure 1.25: Same as Figure 1.23, but now for the case where the lines are shifted according to the first moment value.

telescope, ESO, La Silla, Chile were used and reduced with the TACOS package. Radial velocities were obtained from the cross-correlation profile. Existing line profile diagnostics were evaluated to see whether these were useful to detect the small spectral line variations in these stars in the presence of damping and re-excitation, which is not negligible in red (sub)giants. The amplitude and phase distributions of the line profiles appeared to be very useful and we were able to detect non-radial oscillation modes in these stars, while theory predicts that only radial modes would be observable in red giant stars.

In Chapters 3, 4 and 5 of this thesis, data obtained with the Coudé Auxiliary Telescope (CAT) in conjunction with the Hamilton échelle spectrograph at University of California Observatories / Lick Observatory, USA were used. This was part of a radial velocity survey on K giant stars, which is ongoing at this telescope, using observations with iodine gas in the light path. The survey started in 1999 with about 180 K giant stars, while observations for an additional sample of about 200 G and K giant stars started in 2003.

In Chapter 3, radial velocity results of stable stars obtained from the first sample of 180 K giant stars are presented. An observed radial velocity dispersion of 20 m s^{-1} is used as the stable star threshold. An area in the Hertzsprung-Russell diagram in which most of the stars are stable is identified. In addition, a trend between B-V colour and observed radial velocity variations is present.

In Chapter 4, an investigation into possible mechanisms causing the observed radial velocity variations is presented. First, a correlation was found between surface gravity and radial velocity amplitude. Second, a comparison was made between orbital parameters of inferred sub-stellar companions orbiting stars with a significant periodicity in the present sample, with those present in the literature for main sequence stars. Furthermore, a line shape analysis is performed on high-resolution spectra obtained with the SARG échelle spectrograph mounted on the Telescopio Nazionale Galileo, La Palma, Spain.

In Chapter 5, spectroscopic stellar parameters for the total sample of about 380 G and K giants observed at Lick Observatory are presented. For all stars the effective temperature, surface gravity, iron abundance and rotational velocity are determined and compared with literature values, if available.

In the Summary and Future prospects, the results of the work performed during my PhD and presented in Chapters 2–5 are summarised. Also, some suggestions and ideas for future work are presented.

REFERENCES

Aerts, C. 1996, A&A, 314, 115

Aerts, C., de Pauw, M., & Waelkens, C. 1992, A&A, 266, 294

Balona, L. A. 1986, MNRAS, 219, 111

Baranne, A., Queloz, D., Mayor, M., et al. 1996, A&AS, 119, 373

Bedding, T. R. & Kjeldsen, H. 2003, Publications of the Astronomical Society of Australia, 20, 203

Berdyugina, S. V. 2005, Living Reviews in Solar Physics, 2, 8

Briquet, M. & Aerts, C. 2003, A&A, 398, 687

Butler, R. P., Marcy, G. W., Williams, E., et al. 1996, PASP, 108, 500

Chadid, M., De Ridder, J., Aerts, C., & Mathias, P. 2001, A&A, 375, 113

Chaisson, E. & McMillan, S. 2005, Astronomy Today (Astronomy Today, 5th Edition, by E. Chaisson and S. McMillan. Prentice Hall, 2005. ISBN 0-13-144596-0.)

Christensen-Dalsgaard, J. 2004, Sol. Phys., 220, 137

Cox, J. P. 1980, Theory of stellar pulsation (Research supported by the National Science Foundation Princeton, NJ, Princeton University Press, 1980. 393 p.)

Dikpati, M. & Charbonneau, P. 1999, ApJ, 518, 508

Gray, D. F. 2005, The Observation and Analysis of Stellar Photospheres (The Observation and Analysis of Stellar Photospheres, 3rd Edition, by D.F. Gray. ISBN 0521851866. http://www.cambridge.org/us/catalogue/catalogue.asp?isbn=0521851866. Cambridge, UK: Cambridge University Press, 2005.)

Hekker, S., Aerts, C., de Ridder, J., & Carrier, F. 2006, in ESA SP-624: Proceedings of SOHO 18/GONG 2006/HELAS I, Beyond the spherical Sun

Kjeldsen, H. & Bedding, T. R. 1995, A&A, 293, 87

Marcy, G. W. & Butler, R. P. 1992, PASP, 104, 270

Marcy, G. W. & Butler, R. P. 2000, PASP, 112, 137

Mayor, M. & Queloz, D. 1995, Nature, 378, 355

Queloz, D., Mayor, M., Udry, S., et al. 2001, The Messenger, 105, 1

Saio, H. 1993, Ap&SS, 210, 61

Tassoul, M. 1980, ApJS, 43, 469

Townsend, R. 2004, in IAU Symposium, Vol. 215, Stellar Rotation, ed. A. Maeder & P. Eenens, 404

Unno, W., Osaki, Y., Ando, H., Saio, H., & Shibahashi, H. 1989, Nonradial oscillations of stars (Nonradial oscillations of stars, Tokyo: University of Tokyo Press, 1989, 2nd ed.)

Valenti, J. A., Butler, R. P., & Marcy, G. W. 1995, PASP, 107, 966

Xiong, D. R. & Deng, L. 2007, MNRAS, 378, 1270

CHAPTER 2

Pulsations detected in the line profile variations of red giants: Modelling of line moments, line bisector and line shape

S. Hekker, C. Aerts, J. De Ridder and F. Carrier

Astronomy & Astrophysics 2006, 458, 931

So far, red giant oscillations have been studied from radial velocity and/or light curve variations, which reveal frequencies of the oscillation modes. To characterise radial and non-radial oscillations, line profile variations are a valuable diagnostic. Here we present for the first time a line profile analysis of pulsating red giants, taking into account the small line profile variations and the predicted short damping and re-excitation times. We do so by modelling the time variations in the cross-correlation profiles in terms of oscillation theory. The performance of existing diagnostics for mode identification is investigated for known oscillating giants which have very small line profile variations. We modify these diagnostics, perform simulations, and characterise the radial and non-radial modes detected in the cross-correlation profiles. Moments and line bisectors are computed and analysed for four giants. The robustness of the discriminant of the moments against small oscillations with finite lifetimes is investigated. In addition, line profiles are simulated with short damping and re-excitation times and their line shapes are compared with the observations. For three stars, we find evidence for the presence of non-radial pulsation modes, while for ξ Hydrae perhaps only radial modes are present. Furthermore the line bisectors are not able to distinguish between different pulsation modes and are an insufficient diagnostic to discriminate small line profile variations due to oscillations from exo-planet motion.

2.1 INTRODUCTION

Techniques to perform very accurate radial velocity observations are refined during the last decade. Observations with an accuracy of a few $\mathrm{m\,s^{-1}}$ are obtained regularly (see e.g. Marcy & Butler (2000), Queloz et al. (2001b)) and detections of amplitudes of 1 $\mathrm{m\,s^{-1}}$ are nowadays possible with e.g. HARPS (Pepe et al. 2003). This refinement not only forced a breakthrough in the detection of extra solar planets but also in the observation of solar-like oscillations in distant stars. Solar-like oscillations are excited by turbulent convection near the surface of cool stars of spectral type F, G, K or M and show radial velocity variations with amplitudes of typically a few $\mathrm{cm\,s^{-1}}$ to a few $\mathrm{m\,s^{-1}}$, and with periods ranging from a few minutes for main sequence stars to about half an hour for subgiants and a couple of hours for giants.

For several stars on or close to the main sequence, solar-like oscillations have been detected for a decade (see e.g. Kjeldsen et al. (1995), Bouchy & Carrier (2001), Bouchy & Carrier (2003), Bedding & Kjeldsen (2003)). More recently, such type of oscillations has also been firmly established in several red (sub)giant stars. Frandsen et al. (2002), De Ridder et al. (2006b), Carrier et al. (2006), (see also Barban et al. (2004)) and Carrier et al. (2003) used the CORALIE and ELODIE spectrographs to obtain long term high resolution time series of the three red giants ξ Hydrae, ϵ Ophiuchi and η Serpentis and of the subgiant δ Eridani, respectively. They unravelled a large frequency separation in the radial velocity Fourier transform, with a typical value expected for solar-like oscillations in the respective type of star (a few μHz for giants and a few tens μHz for subgiants), according to theoretical predictions (e.g. Dziembowski et al. (2001)). It was already predicted by Dziembowski (1971) that non-radial oscillations are highly damped in evolved stars, and that, most likely, any detectable oscillations will be radial modes.

So far, red (sub)giant oscillations have only been studied from radial velocity or light variations. Line profile variations are a very valuable diagnostic to detect both radial and non-radial heat driven coherent oscillations (e.g. Aerts & De Cat (2003) and references therein), and to characterise the wavenumbers (ℓ, m) of such self-excited oscillations. It is therefore worthwhile to try and detect them for red (sub)giants with confirmed oscillations and, if successful, to use them for empirical mode identification. This would provide an independent test for the theoretical modelling of the frequency spectrum.

It is also interesting to compare the line profile diagnostics used for stellar oscillation analysis with those usually adopted to discriminate oscillations from exo-planet signatures, such as the line bisector and its derived quantities. Recently, Gray (2005) pointed out that the wide range of bisector shapes he found must contain information about the velocity fields in the atmospheres of cool stars, but that the extraction of information about the velocity variations requires detailed modelling. Here we perform such modelling in terms of non-radial oscillation theory. We do so by considering different types of line characteristics derived from cross-correlation profiles. Dall et al. (2006) already concluded that bisectors are not suitable to analyse solar-like oscillations. We confirm this finding and propose much more suitable diagnostics. We nevertheless investigate how line bisector quantities behave for confirmed oscillators, in order to help future planet hunters in discriminating the cause of small line profile variations in their data.

The main problems in characterising the oscillation modes of red (sub)giants are, first, the low amplitudes of the velocity variations, which results in very small changes in the line profile. Second, the damping and re-excitation times are predicted to be very short. Indeed, Stello et al. (2004) derived an oscillation mode lifetime in ξ Hydrae of only approximately two days.

Table 2.1: Basic stellar parameters of the four stars: Effective temperature ($T_{\rm eff}$) in Kelvin, rotational velocity ($\upsilon \sin i$) in km s^{-1}, parallax (π) in mas, distance (d) in pc, the apparent magnitude ($m_{\rm V}$) and absolute magnitude ($M_{\rm V}$) in the V band.

parameter	ϵ Ophiuchi[a]	η Serpentis	ξ Hydrae	δ Eridani
$T_{\rm eff}$ [K]	4887 ± 100	4855 ± 19^b	5010 ± 15^b	5050 ± 100^c
$\upsilon \sin i$ [km s^{-1}]	3.4 ± 0.5	2.6 ± 0.8^d	2.4^d	2.2 ± 0.9^d
π [mas]	30.34 ± 0.79	52.81 ± 0.75^e	25.23 ± 0.83^e	110.58 ± 0.88^e
d [pc]	33.0 ± 0.9	18.9 ± 0.3	39.6 ± 1.5	9.0 ± 0.1
$m_{\rm V}$ [mag]	3.24 ± 0.02	3.23 ± 0.02^e	3.54 ± 0.06^e	3.52 ± 0.02^e
$M_{\rm V}$ [mag]	0.65 ± 0.06	1.85 ± 0.05	0.55 ± 0.04	3.75 ± 0.2

[a]De Ridder et al. (2006b), [b] Taylor (1999), [c] Carrier et al. (2003), [d] Glebocki & Stawikowski (2000), [e] ESA (1997)

In general, mode lifetimes are difficult to compute for different stellar parameters from current available theory, cf. Houdek et al. (1999) versus Stello et al. (2004). Stello et al. (2006) derived the observed mode lifetime of ξ Hydrae from extensive simulations and find a large difference with theoretical predictions. The known mode identification methods from line profile variations all use an infinite mode lifetime so far. Here, we provide line profile variations simulated for stochastically excited modes, and investigate how the damping affects the behaviour of the diagnostics in this case. We apply our methodology to the four case studies of ξ Hydrae (HD100407, G7III), ϵ Ophiuchi (HD146791, G9.5III), η Serpentis (HD168723, K0III) and δ Eridani (HD23249, K0IV). Some basic properties of these stars are listed in Table 2.1.

The paper is organised as follows. In Sect. 2 the data set at our disposal and different observational diagnostics are described. In Sect. 3 the diagnostics for mode identification are described, while in Sect. 4 the damping and re-excitation effects in theoretically generated spectral lines are investigated. In Sect. 5 the results obtained from the simulations and observations are compared and in Sect. 6 some conclusions are drawn.

2.2 OBSERVATIONAL DIAGNOSTICS

2.2.1 Spectra

For all four stars we have spectra at our disposal obtained with the fibre fed échelle spectrograph CORALIE mounted on the Swiss 1.2 m Euler telescope at La Silla (ESO, Chile). The observations for ξ Hydrae were made during one full month (2002 February 18 - March 18). This is the same dataset as used by Frandsen et al. (2002) for the detection of the solar-like oscillations. For ϵ Ophiuchi and η Serpentis the solar-like observations described by De Ridder et al. (2006b) and Carrier et al. (2006) are obtained from a bi-site campaign, using CORALIE and ELODIE (the fibre fed échelle spectrograph mounted on the French 1.93 m telescope at the Observatoire de Haute Provence) during the summer of 2003. The observations of δ Eridani are obtained with CORALIE during a twelve day campaign in November 2001. For the line profile analysis, described in this paper, only the data obtained with CORALIE are used. These spectra

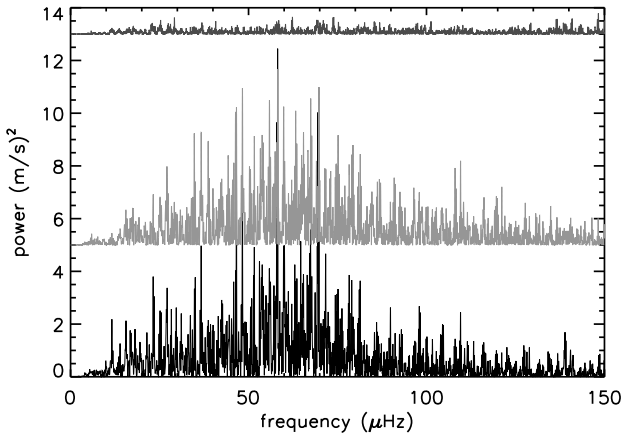

Figure 2.1: Power spectrum of ϵ Ophiuchi. The lower black one is obtained by De Ridder et al. (2006b), the grey one in the middle is obtained from $\langle \mathrm{v} \rangle$ and the top one is obtained from the bisector velocity span. For clarity the latter two are shifted.

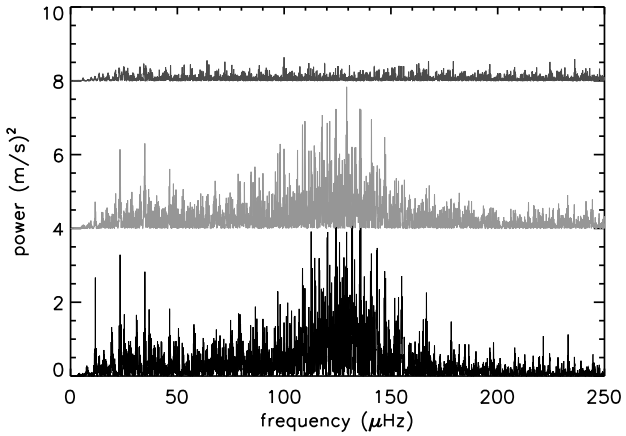

Figure 2.2: Power spectrum of η Serpentis. The lower black one is obtained by Carrier et al. (2006), the grey one in the middle is obtained from $\langle \mathrm{v} \rangle$ and the top one is obtained from the bisector velocity span. For clarity the latter two are shifted.

range in wavelength from 387.5 nm to 682 nm and the observation times were adjusted to reach a signal to noise ratio of at least 100 at 550 nm (60-120 for δ Eridani) without averaging out a too large fraction of the pulsation phase. More details about the observation strategy is available in the publications describing the first detections of the solar-like oscillations of the respective stars.

2.2.2 Cross-correlation profiles

The line profile variations of the four pulsating red (sub)giants are analysed with moments (Aerts et al. 1992) and with the line bisector (Gray 2005). The moments are often used to analyse stellar oscillations excited by a heat mechanism, while the line bisector is usually adopted to discover planet signatures. Both methods can be applied to one single spectral line, but also to a cross-correlation profile, which has an increased signal to noise ratio:

$$SNR_{\mathrm{cross-cor}} = \sqrt{M < (SNR)^2 >} \tag{2.1}$$

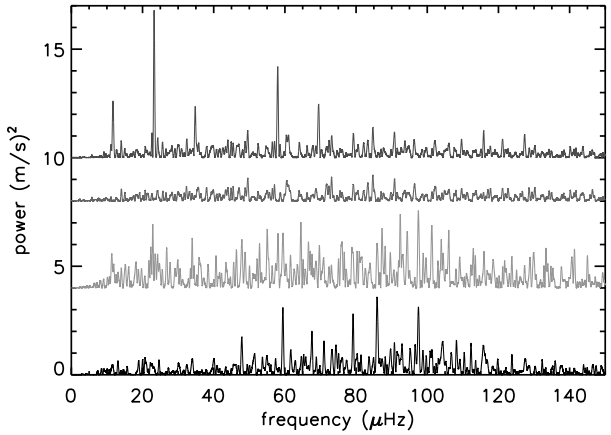

Figure 2.3: Power spectrum of ξ Hydrae. The lower black one is obtained by Frandsen et al. (2002), the grey one is obtained from $\langle \mathrm{v} \rangle$. The two top power spectra are obtained from the bisector velocity span. The top one is the original, while the lower one is corrected for the 1 c d^{-1} (11.57μHz) frequency due to the diurnal cycle. For clarity the latter three power spectra are shifted.

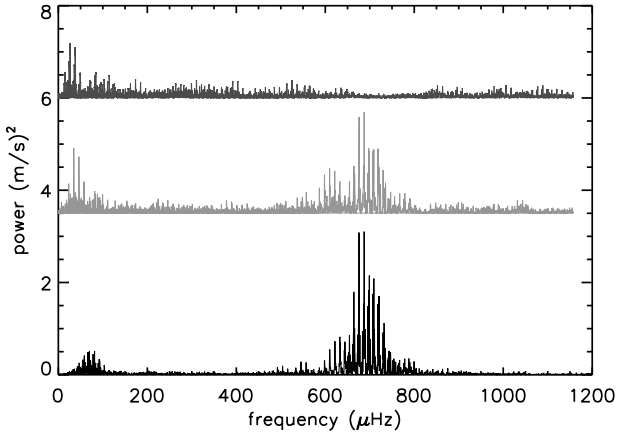

Figure 2.4: Power spectrum of δ Eridani. The lower black one is obtained by Carrier et al. (2003), the grey one in the middle is obtained from $\langle \mathrm{v} \rangle$. The top power spectrum is obtained from the bisector velocity span. For clarity the latter two power spectra are shifted.

with M the number of spectral lines used for the cross-correlation and $< (SNR)^2 >$ the average of the squared signal to noise ratios of each spectral line used. The cross-correlation profiles are constructed from a mask in such a way that the weak, strong and blended lines are excluded. They are a good representation of an average spectral line of the star whenever the lines are formed at not too different line formation regions in the atmosphere.

Mathias & Aerts (1996) and Chadid et al. (2001) already performed a line profile analysis on cross correlation profiles for a δ Scuti star using moments (Aerts et al. 1992). Compared to the analysis of a single spectral line this only introduces some additional terms in the moments for which can be corrected. Furthermore, the line bisector analysis is widely used on cross-correlation profiles (see e.g. Queloz et al. (2001a), Setiawan et al. (2003), Martínez Fiorenzano et al. (2005), Dall et al. (2006)). Dall et al. (2006) showed that the cross-correlation bisector contains the same information as single line bisectors.

The red (sub)giants analysed in the present work show low amplitude radial velocity variations, which result in very small line profile variations. The INTER-TACOS (INTERpreter for the Treatment, the Analysis and the COrrelation of Spectra) software package developed at Geneva Observatory (Baranne et al. 1996), was used to cross correlate the observed spectrum

with a mask containing atmospheric lines of red (sub)giants with a resolution of 100 m s^{-1}. On top of that we interpolated to a resolution of 10 m s^{-1} to reach the highest possible precision in the computation of the moments.

2.2.3 Frequency analysis

In order to see whether the line moments and line bisector are sensitive enough to determine the very small line profile variations present in pulsating red (sub)giants, a frequency analysis is performed and compared with the frequencies obtained previously. Frandsen et al. (2002), De Ridder et al. (2006b), Carrier et al. (2006) and Carrier et al. (2003) used radial velocity variations, obtained with the optimum weight method described by Bouchy et al. (2001), for their frequency analysis.

Moments

A line profile can be described by its moments (Aerts et al. 1992). The first moment $\langle \mathrm{v} \rangle$ represents the centroid velocity of the line profile, the second moment $\langle \mathrm{v}^2 \rangle$ the width of the line profile and the third moment $\langle \mathrm{v}^3 \rangle$ the skewness of the line profile. The quantity $\langle \mathrm{v} \rangle$ is thus a particular measure of the radial velocity and should therefore show similar frequency behaviour. We expect it to perform less well than the radial velocity measure derived from the optimum weight method (Bouchy et al. 2001) (see below), but $\langle \mathrm{v} \rangle$ is a mode identification diagnostic (Aerts et al. 1992), while other radial velocity measures are not. This is why we re-compute and re-analyse the radial velocity from $\langle \mathrm{v} \rangle$ here.

Frequencies are determined with the conventional method of iterative sinewave fitting ('prewhitening'). A Scargle periodogram (Scargle 1982) is used with frequencies between 0 and 15 cycles per day (c d^{-1}) (173.6 μHz) and with a frequency step of 0.0001 c d^{-1} (0.001 μHz) for the red giants. For the subgiant frequencies between 0 and 150 c d^{-1} and a frequency step of 0.001 c d^{-1} are used. The significance of the frequencies is calculated with respect to the average amplitude of the periodogram after prewhitening as described in Kuschnig et al. (1997). The errors in the frequency are obtained with the method described by Breger et al. (1999) and have typical values of 10^{-4} c d^{-1} ($10^{-9}\mu$Hz) for the giants and 10^{-3} c d^{-1} ($10^{-8}\mu$Hz) for the subgiant.

The frequencies of $\langle \mathrm{v} \rangle$ are compared to the frequencies obtained from radial velocities derived from the optimum weight method, mentioned in earlier publications. In Figs 2.1, 2.2, 2.3 and 2.4 the power spectra of ϵ Ophiuchi, η Serpentis, ξ Hydrae and δ Eridani are shown, respectively. The lower black power spectra are the ones obtained by De Ridder et al. (2006b), Carrier et al. (2006), Frandsen et al. (2002) and Carrier et al. (2003), while the grey ones in the middle are obtained from $\langle \mathrm{v} \rangle$ in the present work.

Although the same data is used, a comparison is made between power spectra of two different representations of the radial velocity variations, computed with different methods. The radial velocity derived from the optimum weight method is intrinsically more precise than the one from $\langle \mathrm{v} \rangle$ of the cross-correlation. It not only uses the full spectrum instead of a box shaped mask, but also relies on weights of the individual spectra. These differences influence the noise and the amplitudes in the power spectra. On top of that the reference point of each night is de-

termined by the observation with the highest signal to noise ratio in case of the optimum weight method and by the average of the night in case $\langle \mathrm{v} \rangle$ is used. As nightly reference points are effectively a high pass filter, different filters induce differences at low frequencies in the power spectra.

Despite these differences the comparison between the power spectra in the literature and obtained from $\langle \mathrm{v} \rangle$ is very good, especially for ϵ Ophiuchi and δ Eridani. For η Serpentis, the dominant frequencies obtained by Carrier et al. (2006) are slightly different. This is mainly due to the additional ELODIE data, which contains a substantial number of observations and therefore alters the time sampling of the data. In case only the CORALIE data are taken into account, the dominant frequencies match very well. For ξ Hydrae the dominant frequencies obtained by Frandsen et al. (2002) are more distinct than those obtained from $\langle \mathrm{v} \rangle$. This is due to the low amplitude of this star, which implies a larger relative difference between the different computations of the radial velocity than for the other two giants. Nevertheless, the overall shape of the power spectra obtained from the radial velocity and from $\langle \mathrm{v} \rangle$ is comparable. The fact that $\langle \mathrm{v} \rangle$ shows the same behaviour as the radial velocity obtained with the method described by Bouchy et al. (2001), indicates that this moment diagnostic is able to detect low amplitude oscillations of red (sub)giants.

The behaviour of $\langle \mathrm{v}^2 \rangle$ obtained from a cross-correlation is not exactly the same as for a single spectral line. Chadid et al. (2001) show that the constant of a sinusoidal fit through $\langle \mathrm{v}^2 \rangle$ is different in case of a cross-correlation compared to a single spectral line. Furthermore, a fit through $\langle \mathrm{v}^3 \rangle$ obtained from a cross-correlation contains a non zero constant, which is not the case for a single spectral line. This indicates that we should be very cautious in interpreting the constants of the moments. Chadid et al. (2001) attribute the different behaviour of $\langle \mathrm{v}^2 \rangle$ and $\langle \mathrm{v}^3 \rangle$ obtained from cross correlation to the influence of possible blending with very faint lines which alters the absolute values of $\langle \mathrm{v}^2 \rangle$ and $\langle \mathrm{v}^3 \rangle$, but not their variation.

For the observed red giants, $\langle \mathrm{v}^2 \rangle$ shows variations in the average value per night, which is probably caused by changing instrumental conditions. Although a correction for this behaviour is applied by shifting the values of each night to the average value of all observations, $\langle \mathrm{v}^2 \rangle$ does not behave as predicted from theory. Frequencies for $\langle \mathrm{v}^2 \rangle$ are expected to be: ν_i, $\nu_i + \nu_j$ or $\nu_i - \nu_j$, with $\nu_{i,j}$ the frequencies obtained in $\langle \mathrm{v} \rangle$ (Mathias et al. 1994), but are not found in the observations. For all four stars, the frequencies obtained for $\langle \mathrm{v}^3 \rangle$ are the same as for $\langle \mathrm{v} \rangle$, which is as expected.

Line Bisector

The line bisector is a measure of the displacement of the centre of the red and blue wing from the core of the spectral line at each residual flux. The line bisector is often characterised by the bisector velocity span, which is defined as the horizontal distance between the bisector positions at fractional flux levels in the top and bottom part of the spectral line, see for instance Brown et al. (1998). The bisector velocity span is supposed to remain constant over time in case of sub-stellar companions.

The bisector velocity span is calculated in this work as the difference between the bisector at a fractional flux level of 0.80 and 0.20. The frequencies of the bisector velocity span are determined in the same way as the frequencies of the moments.

Bisector velocity spans are calculated for simulated spectral lines of stars pulsating with

different modes, using ϵ Ophiuchi's amplitude. In case of noiseless line profiles and infinite mode lifetimes, the dominant frequency of modes with $m = 0$ is 2ν, with ν the dominant frequency obtained for $\langle \mathrm{v} \rangle$. In case $m \neq 0$, ν is obtained as the dominant frequency. For infinite mode lifetimes the dominant frequency obtained for modes with $m = 0$ is low, but at 2ν the power spectrum also shows a clear excess. For modes with $m \neq 0$ we obtained ν as the dominant frequency. This is completely in line with the behaviour expected for $\langle \mathrm{v}^2 \rangle$ (Aerts et al. 1992).

To give an estimate of the minimum signal to noise ratio needed to detect a dominant frequency, with the amplitude detected for ϵ Ophiuchi in the bisector velocity span, we added white noise to the simulated spectral lines. These simulations reveal that for pulsations with infinite as well as finite mode lifetimes with $m = 0$, a signal to noise ratio of 100 000 is not enough to reveal a frequency in the bisector velocity span, while a signal to noise ratio of order a few 10 000 would suffice for modes with $m \neq 0$. The signal to noise ratio of the cross-correlation profiles of our targets does not exceed a few 1 000 (see Equation 2.1). This signal to noise level is much less than the minimum value needed to detect the oscillations.

The top graphs in Figs 2.1, 2.2, 2.3 and 2.4 show the power spectra of the bisector velocity span for ϵ Ophiuchi, η Serpentis, ξ Hydrae and δ Eridani, respectively. The bisector velocity spans for ϵ Ophiuchi and η Serpentis do not show any dominant frequency. The power spectrum of the bisector velocity span of ξ Hydrae shows peaks at 1 c d^{-1} (11.57μHz) and at its 1 day aliases (Fig. 2.3 top). The aliases are due to the diurnal cycle and in case these are removed no dominant frequencies in the bisector velocity span can be seen (Fig. 2.3 second power spectrum from the top). For δ Eridani the bisector velocity span shows some peaks at low frequencies, but from asteroseismological considerations solar-like pulsations can not occur at these low frequencies in subgiants. These peaks are probably caused by instrumental effects. From the present test case, one can thus conclude that, at least for low amplitude oscillations, discrimination between exo-planet companions and pulsations is not possible with the bisector velocity span on data with realistic signal to noise ratio. This result is consistent with Dall et al. (2006).

2.3 THEORETICAL MODE DIAGNOSTICS

In order to characterise wavenumbers (ℓ, m) for the modes present in the red (sub)giants, the mathematical description of the line bisector (Brown et al. 1998) and of the moments (Aerts et al. 1992) are investigated.

Brown et al. (1998) introduced a mathematical description for the line bisector in terms of orthogonal Hermite functions. The Hermite coefficients h_i describe the line shapes. Information on the oscillation mode, inclination and velocity parameters of the star was obtained by Brown et al. (1998) from a comparison with theoretically generated line profile variations during a pulsation cycle, assuming infinite mode lifetimes. To obtain the wavenumbers of the oscillations, the Hermite coefficients or bisector velocity span, obtained from observations, are compared with the ones obtained from the simulated line profiles. The main drawback of this description in Hermite functions is the lack of a pulsation theory directly coupled to the Hermite coefficients or bisector velocity span. For this reason we do not use it here.

The variations in the observed moments of the line profiles are compared with their theoretical expectations derived from oscillation theory (Aerts et al. 1992). The moments are a function

of wavenumbers ℓ, m, inclination angle i, pulsation velocity amplitude $\upsilon_{\rm osc}$, projected rotational velocity $\upsilon \sin i$ and intrinsic width of the line profile σ. The comparison is performed objectively with a discriminant (Aerts et al. (1992), Aerts (1996), Briquet & Aerts (2003)) which selects the most likely set of parameters $(\ell, m, i, \upsilon_{\rm osc}, \upsilon \sin i, \sigma)$. Due to the fact that several combinations of the wavenumbers and velocity parameters result in almost the same line profile variation, the "few" best solutions resulting from the discriminant should be investigated carefully before drawing conclusions about the mode identity.

The fact that $\langle \mathrm{v} \rangle$ and $\langle \mathrm{v}^3 \rangle$ are sensitive to the very small line profile variations and the direct connection between the moments and pulsation theory makes moments, in principle, suitable for the analysis of pulsating red (sub)giants, provided that we test its robustness against small amplitudes and the finite lifetimes of the modes. This is what we have done in the present work.

2.3.1 Discriminant

In the present analysis the discriminant is determined for $\ell = 0, 1, 2$, inclination angles ranging from 5° until 85° with steps of 1°, projected rotational velocity $\upsilon \sin i$ and intrinsic width of the line profile σ between 0 and 5 km s^{-1} with steps of 0.5 km s^{-1}. Furthermore a limbdarkening coefficient $u(\lambda)$ of 0.5 is used (van Hamme 1993).

Due to the fact that the red (sub)giants show low amplitude variations, the discriminant might give inclination angles close to an inclination angle of complete cancellation (IACC) (Chadid et al. 2001). Complete cancellation occurs when the star is looked upon in such way that the contribution to $\langle \mathrm{v} \rangle$ of each point on the stellar disk exactly cancels out the contribution of another point on the stellar disk. Therefore the angles close to 0° and 90° are not taken into account, as well as solutions close to the IACC at $i = 54.7^\circ$ for $\ell = 2, m = 0$.

As the discriminant is designed for oscillations inducing moment variations larger than the equivalent width of the line (moment of order zero), a check needs to be performed whether this technique is applicable in the present work. Therefore three series of spectral line profiles with infinite lifetimes and different pulsation velocity amplitudes are generated using the 628 observation times of ϵ Ophiuchi. The dominant frequency of ϵ Ophiuchi, 5.03 c d^{-1} (58.2 μHz), is used as an input parameter at an inclination angle of $i = 35^\circ$ for wavenumbers $\ell = 0, 1, 2$ with positive m values, a projected rotational velocity $\upsilon \sin i = 3.5$ km s^{-1} and an intrinsic width $\sigma = 4$ km s^{-1}. Furthermore, the equivalent width of the spectral lines is taken to be 10 km s^{-1}, while the minimum amplitude of the pulsation velocity ($\upsilon_{\rm osc}$) is 0.04 km s^{-1} and increases with a factor of ten for the different series. For these series the moments are calculated as well as the discriminant. For a pulsation velocity amplitude of 0.04 km s^{-1}, which resembles the data best, $\langle \mathrm{v}^2 \rangle$ of modes with $m = 0$ all show the expected harmonic of the frequency (Mathias et al. 1994), but with a different constant. The discriminant values only differ by an order of 0.01 km s^{-1}. This is also the case for a pulsation velocity amplitude of 0.4 km s^{-1}, which indicates that the discriminant is not suitable for the analysis of small line profile variations with an amplitude below 1 km s^{-1}. For a pulsation velocity amplitude of 4.0 km s^{-1} the difference between the discriminant values increases and the correct mode is present among the best options. This indicates that the discriminant is a useful analysis tool for spectral line variations with amplitude larger than about half the equivalent width of the spectral line, but not for red (sub)giants.

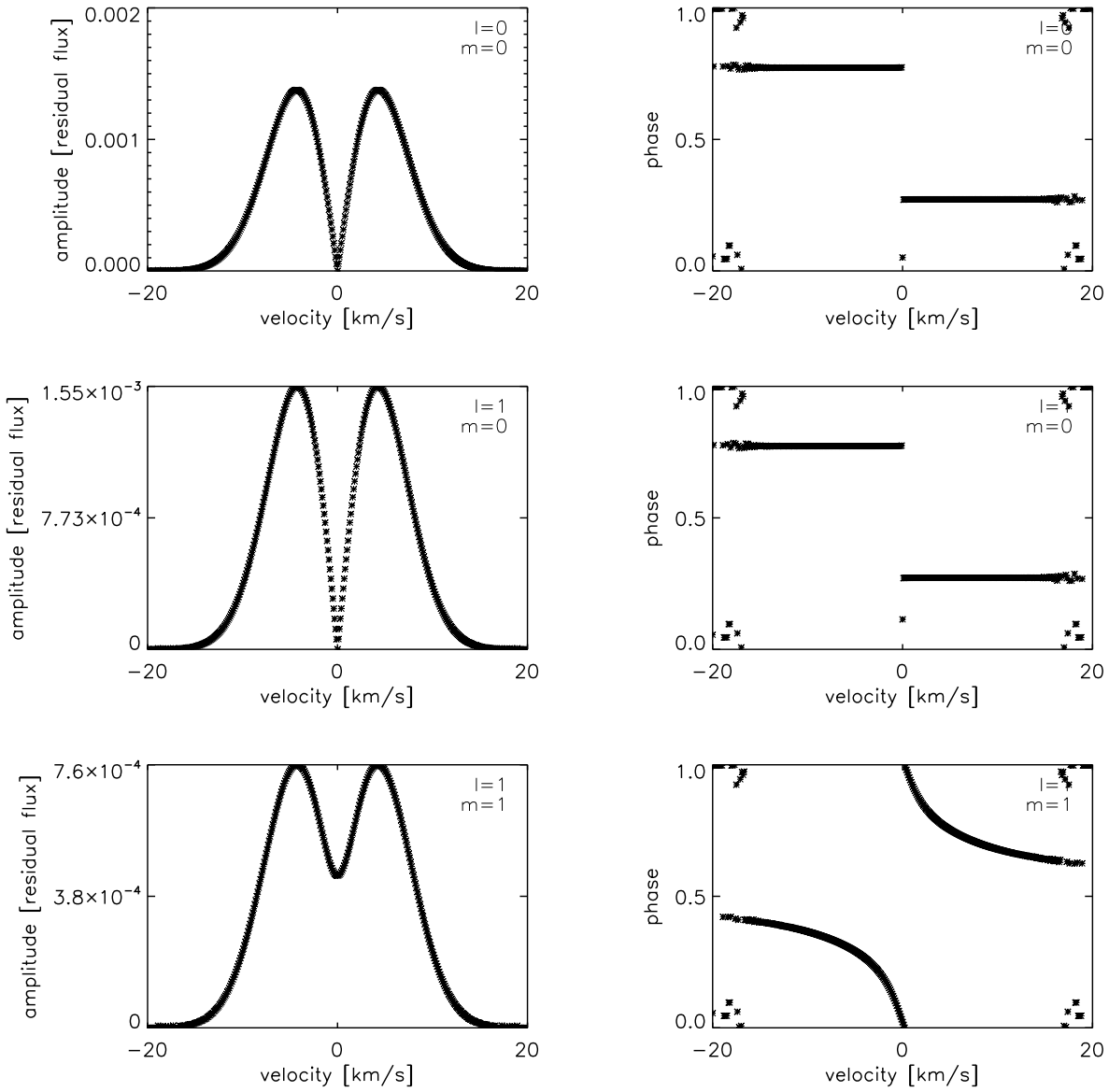

Figure 2.5: The amplitude (left) and phase (right) distributions for simulated line profiles with infinite damping time at an inclination angle of $i = 35°$. Top: $\ell = 0$, $m = 0$, middle: $\ell = 1$, $m = 0$, bottom: $\ell = 1$, $m = 1$.

2.3.2 Amplitude and phase distribution

As the discriminant is not useful in the present analysis, the spectral lines are investigated by comparing the amplitude and phase across the line profile with the ones obtained from simulations. This is the same procedure as used by Telting et al. (1997) for β Cephei and by De Cat et al. (2005) for the complex line profile behaviour due to the multi periodic gravity mode oscillations in slowly pulsating B stars. The amplitude and phase for each velocity in the cross-correlation profile are determined by fitting a harmonic function, with the dominant frequencies

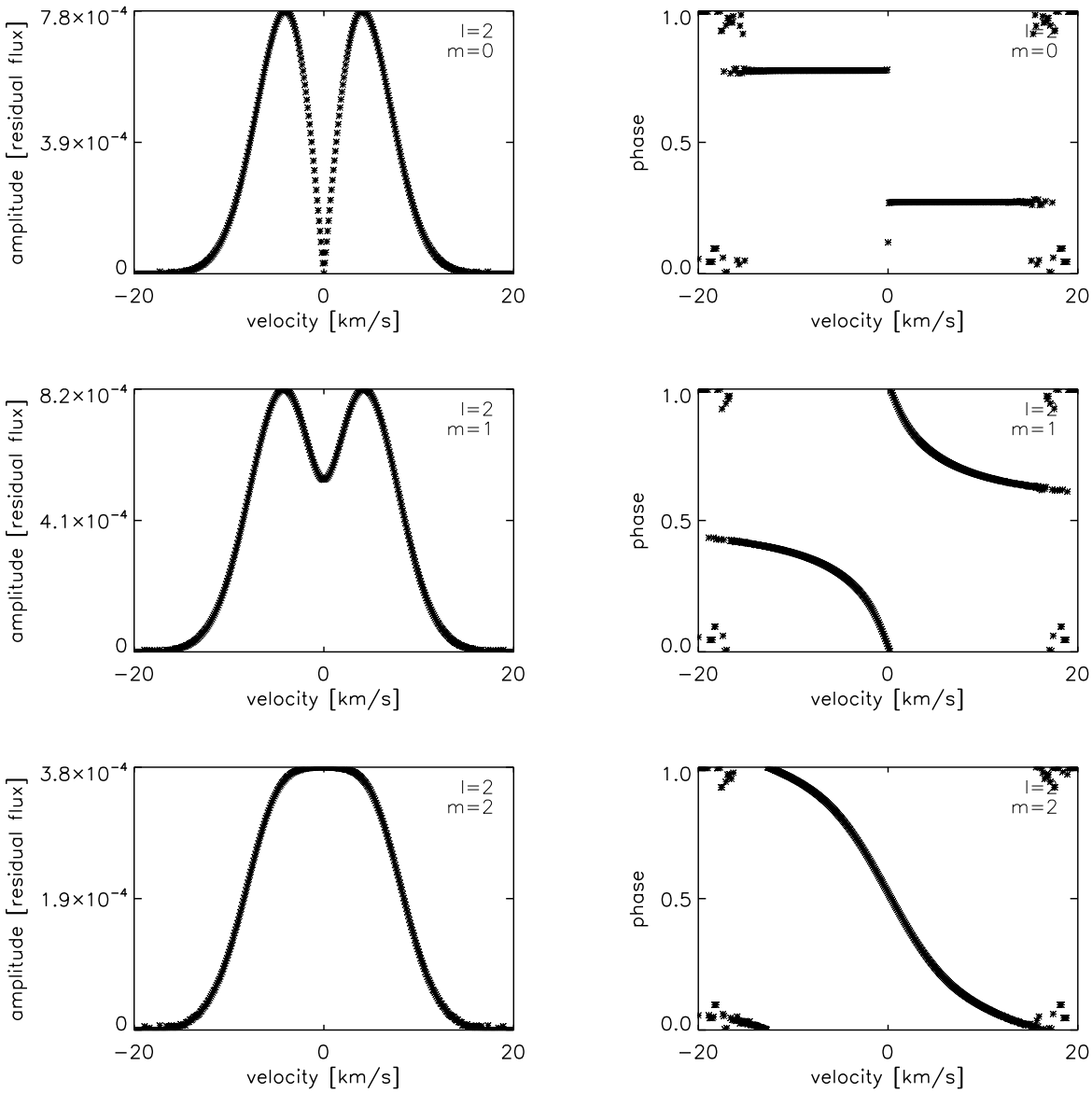

Figure 2.5: Continued. Top: $\ell = 2$, $m = 0$, middle: $\ell = 2$, $m = 1$, bottom: $\ell = 2$, $m = 2$

$\nu_{\langle \mathrm{v} \rangle}$ c d^{-1}	$\nu_{\langle \mathrm{v} \rangle}$ μHz	significance	ν^a c d^{-1}	ν^a μHz
5.03	58.2	4.69σ	5.03	58.2
5.46	63.2	3.99σ	5.44	63.0
5.83	67.5	3.98σ	5.82	67.4
			4.59	53.1
3.17	36.7	3.43σ	4.17	48.3
			4.46	51.6
			5.59	64.7
			6.19	71.7
			5.18	59.9
			6.00	69.5
			6.43	74.4

[a] De Ridder et al. (2006b)

Table 2.2: Comparison between frequencies found in $\langle \mathrm{v} \rangle$ ($\nu_{\langle \mathrm{v} \rangle}$) and the ones found by De Ridder et al. (2006b) in the radial velocity of ϵ Ophiuchi. The significance of $\nu_{\langle \mathrm{v} \rangle}$ is calculated with respect to the average amplitude of the periodogram after prewhitening as described by Kuschnig et al. (1997): $4\sigma \propto 99.9\%$ confidence interval, $3.6\sigma \propto 99\%$ confidence interval and $3.25\sigma \propto 95\%$ confidence interval.

of $\langle \mathrm{v} \rangle$, to the flux values at each velocity pixel of the time series of spectra (Schrijvers et al. 1997). The amplitudes and phases as function of velocity determined from simulated line profiles with $\ell = 0, 1, 2$, and positive m values are shown in Fig. 2.5, assuming infinite lifetimes. The simulations are shown for $i = 35^\circ$, but the shape of the amplitude and phase distribution does not change significantly with inclination angle.

The amplitude and phase distribution across the line profile of ϵ Ophiuchi, η Serpentis, ξ Hydrae and δ Eridani are shown in Figs 2.6, 2.7, 2.8 and 2.9 respectively. The dominant frequencies obtained from $\langle \mathrm{v} \rangle$ are used for the harmonic fits at each velocity in the line profile. The frequencies obtained for each star are listed in Tables 2.2, 2.3, 2.4 and 2.5. The window-function for η Serpentis changes slightly in case only CORALIE data is used compared to the one obtained from both CORALIE and ELODIE data (Carrier et al. 2006). For the CORALIE data we find an extra aliasfrequency of 0.17 c d^{-1}. The frequency 11.17 c d^{-1}, only obtained for the CORALIE data, is therefore an alias of the 10.33 c d^{-1} frequency obtained by Carrier et al. (2006). The frequency $\nu = 3.00$ c d^{-1} for δ Eridani is indicated in bold because this is an alias of the diurnal cycle of the observations and not due to solar-like oscillations.

2.4 SIMULATIONS

In order to test the robustness of moment diagnostics and the amplitude and phase behaviour across the line profiles against finite lifetimes of oscillation modes, spectral lines are generated with damped and re-excited modes. The moments of these lines are obtained and their dominant frequencies derived. Furthermore, the amplitude and phase distributions across the spectral line are investigated.

The simulations are done for a single lineforming region. Therefore, the simulated phase distributions are not necessarily comparable to the observed ones, which are averaged phase distributions over a whole range of line forming regions because they are based on a cross-correlation function. Our interpretation will therefore mainly be based on the amplitude distri-

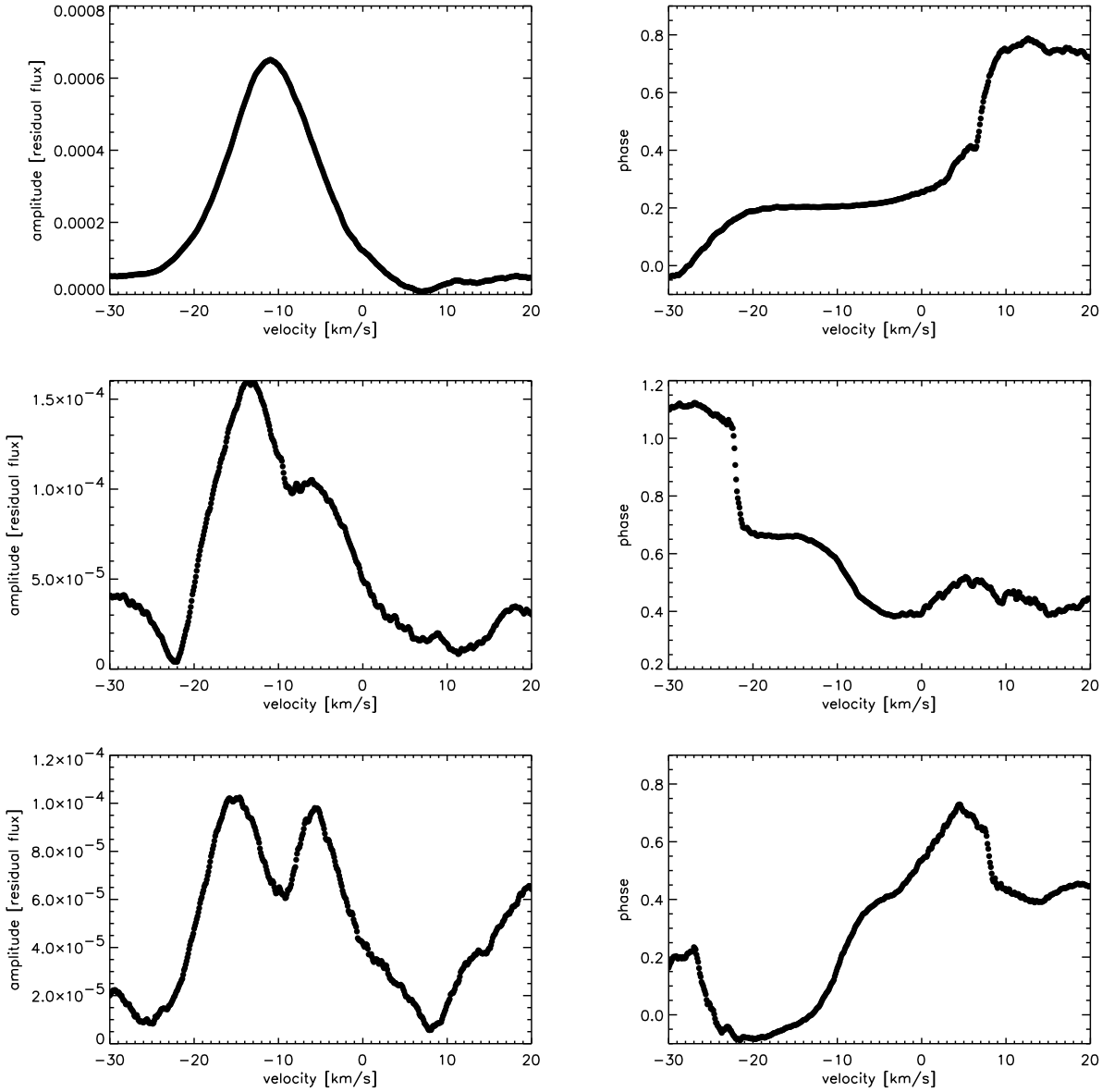

Figure 2.6: The amplitude (left) and phase (right) distributions as a function of velocity across the line profile of ϵ Ophiuchi for three significant frequencies obtained from $\langle \mathrm{v} \rangle$: $\nu_{\langle \mathrm{v} \rangle} = 5.03$ c d^{-1} (58.2μHz) (top) $\nu_{\langle \mathrm{v} \rangle} = 5.46$ c d^{-1} (63.2μHz) (middle) and $\nu_{\langle \mathrm{v} \rangle} = 5.83$ c d^{-1} (67.5μHz) (bottom). The mean radial velocity of the star, is found to be approximately -9.4 km s^{-1}.

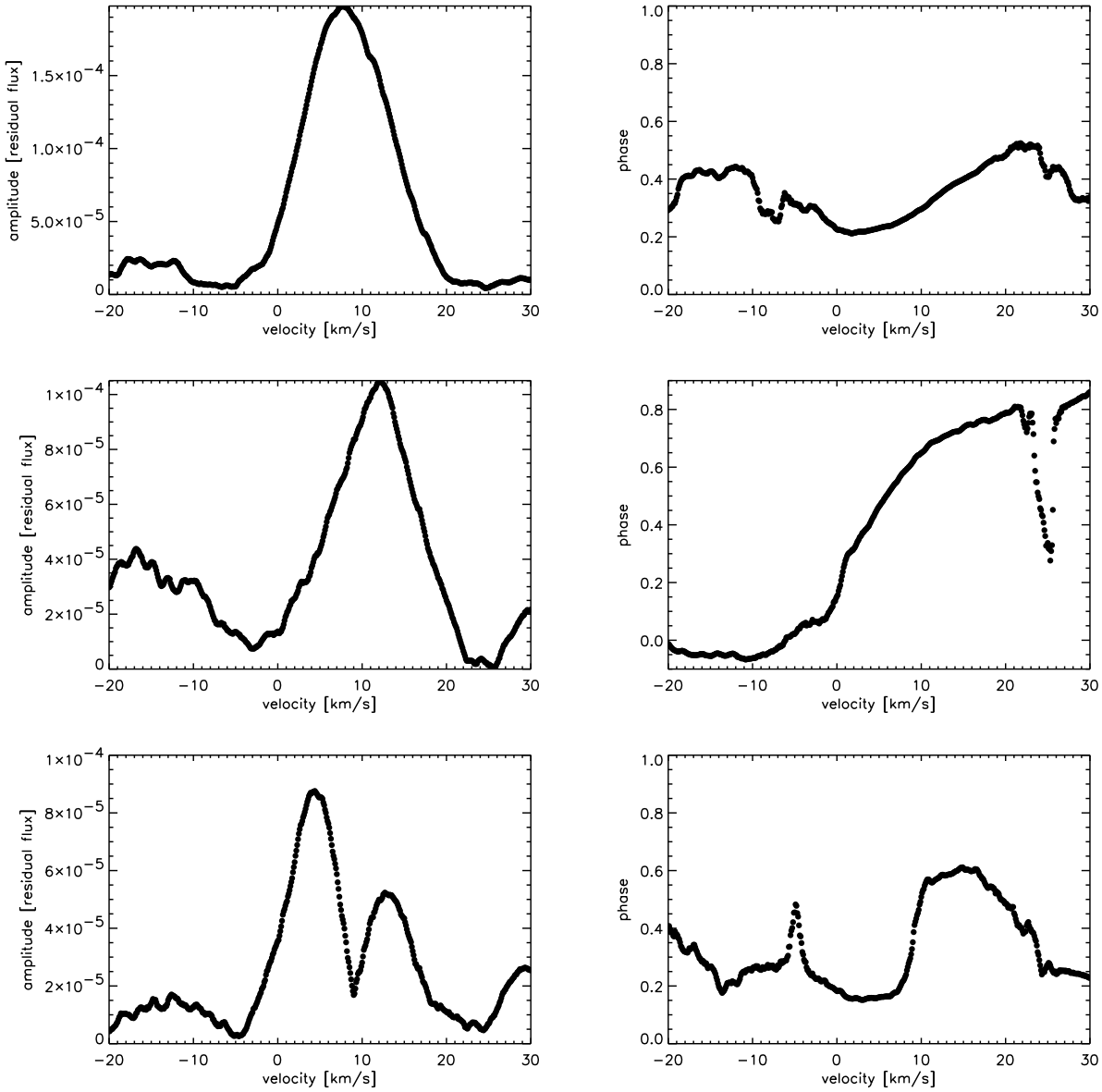

Figure 2.7: The amplitude (left) and phase (right) distributions as a function of velocity across the line profile of η Serpentis for three significant frequencies obtained from $\langle \mathrm{v} \rangle$: $\nu_{\langle \mathrm{v} \rangle} = 11.17$ c d^{-1} (129.3μHz) (top), $\nu_{\langle \mathrm{v} \rangle} = 11.71$ c d^{-1} (135.5μHz) (middle) and $\nu_{\langle \mathrm{v} \rangle} = 10.38$ c d^{-1} (120.2μHz) (bottom). The mean radial velocity of the star, is found to be approximately 9.4 km s^{-1}.

$\nu_{\langle \mathrm{v} \rangle}$ c d^{-1}	$\nu_{\langle \mathrm{v} \rangle}$ μHz	signi-ficance	ν^a c d^{-1}	ν^a μHz	ν^b c d^{-1}	ν^b μHz
11.71	135.5	3.80σ	10.74	124.3	11.74	135.9
10.38	120.2	3.61σ	10.38	120.2	10.40	120.4
					11.49	133.0
					13.27	153.6
					10.96	126.8
					10.90	126.2
11.17	129.3	4.23σ	11.17	129.3	10.33	119.6
					11.69	135.3
					7.48	86.6
					7.28	84.3
					6.20	71.8

[a]Only CORALIE data from Carrier et al. (2006).
[b]Carrier et al. (2006)

Table 2.3: Comparison between frequencies found in $\langle \mathrm{v} \rangle$ and the ones found by Carrier et al. (2006) in the radial velocity of η Serpentis. The significance of $\nu_{\langle \mathrm{v} \rangle}$ is calculated with respect to the average amplitude of the periodogram after prewhitening as described by Kuschnig et al. (1997): $4\sigma \propto 99.9\%$ confidence interval, $3.6\sigma \propto 99\%$ confidence interval and $3.25\sigma \propto 95\%$ confidence interval.

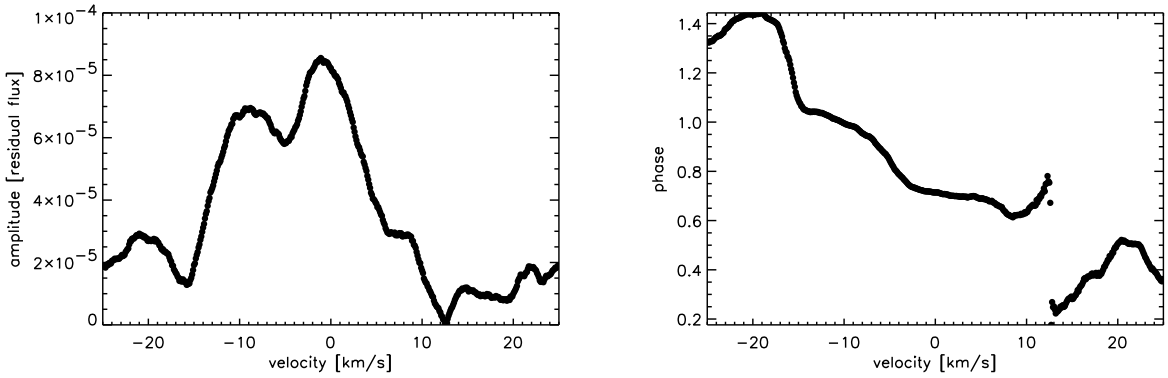

Figure 2.8: The amplitude (left) and phase (right) distributions as a function of velocity across the line profile of ξ Hydrae for the most dominant frequency obtained from $\langle \mathrm{v} \rangle$: $\nu_{\langle \mathrm{v} \rangle} = 8.42$ c d^{-1} (97.5μHz). The mean radial velocity of the star, is found to be approximately -4.6 km s^{-1}.

bution which represents an average amplitude across the whole lineforming region considered in the cross-correlation function.

2.4.1 Damping and re-excitation equations

A damped and re-excited oscillation mode is damped by a factor $e^{-\eta t}$, with η the damping rate, and re-excited before it is able to damp out. As a consequence both the amplitude (A) and the phase (ψ) of the oscillation are time dependent:

$$f(t) = A(t)\sin(2\pi\nu t + \psi(t)). \tag{2.2}$$

$\nu_{\langle \mathrm{v} \rangle}$ c d^{-1}	$\nu_{\langle \mathrm{v} \rangle}$ μHz	significance	ν^a c d^{-1}	ν^a μHz
			5.1344(26)	59.43
			6.8366(27)	79.13
8.42	97.5	3.00σ	7.4265(29)	85.96
			8.2318(32)	95.28
			9.3507(33)	108.22
			8.7399(36)	101.16
			10.0287(43)	116.07
			9.0831(44)	105.13
			8.5339(40)	98.77

[a]Frandsen et al. (2002)

Table 2.4: Comparison between frequencies found in $\langle \mathrm{v} \rangle$ and the ones found by Frandsen et al. (2002) in the radial velocity of ξ Hydrae. The significance of $\nu_{\langle \mathrm{v} \rangle}$ is calculated with respect to the average amplitude of the periodogram after prewhitening as described by Kuschnig et al. (1997). A significance of $3\sigma \propto 85\%$ confidence interval.

$\nu_{\langle \mathrm{v} \rangle}$ c d^{-1}	$\nu_{\langle \mathrm{v} \rangle}$ μHz	significance	ν^a c d^{-1}	ν^a μHz
			43.55	504.0
			47.12	545.4
			49.59	573.9
			52.73	610.3
52.68	609.7	4.84σ	54.67	632.7
			56.54	654.4
			58.06	672.0
59.40	687.5	7.45σ	58.40	675.9
			60.65	702.0
61.08	706.9	6.01σ	62.08	718.5
60.25	697.3	4.08σ	62.27	720.7
57.55	666.1	4.45σ	64.55	747.1
65.28	755.6	3.71σ	66.28	767.1
			68.07	787.9
			75.63	875.4
3.00	34.7	5.89σ		

[a]Carrier et al. (2003)

Table 2.5: Comparison between frequencies found in $\langle \mathrm{v} \rangle$ and the ones found by Carrier et al. (2003) in the radial velocity of δ Eridani. The significance of $\nu_{\langle \mathrm{v} \rangle}$ is calculated with respect to the average amplitude of the periodogram after prewhitening as described by Kuschnig et al. (1997): $4\sigma \propto 99.9\%$ confidence interval, $3.6\sigma \propto 99\%$ confidence interval and $3.25\sigma \propto 95\%$ confidence interval. $\nu_{\langle \mathrm{v} \rangle} = 3.00$ c d^{-1} is indicated in bold, because this is an alias of the diurnal cycle of the observations and not due to solar-like oscillations.

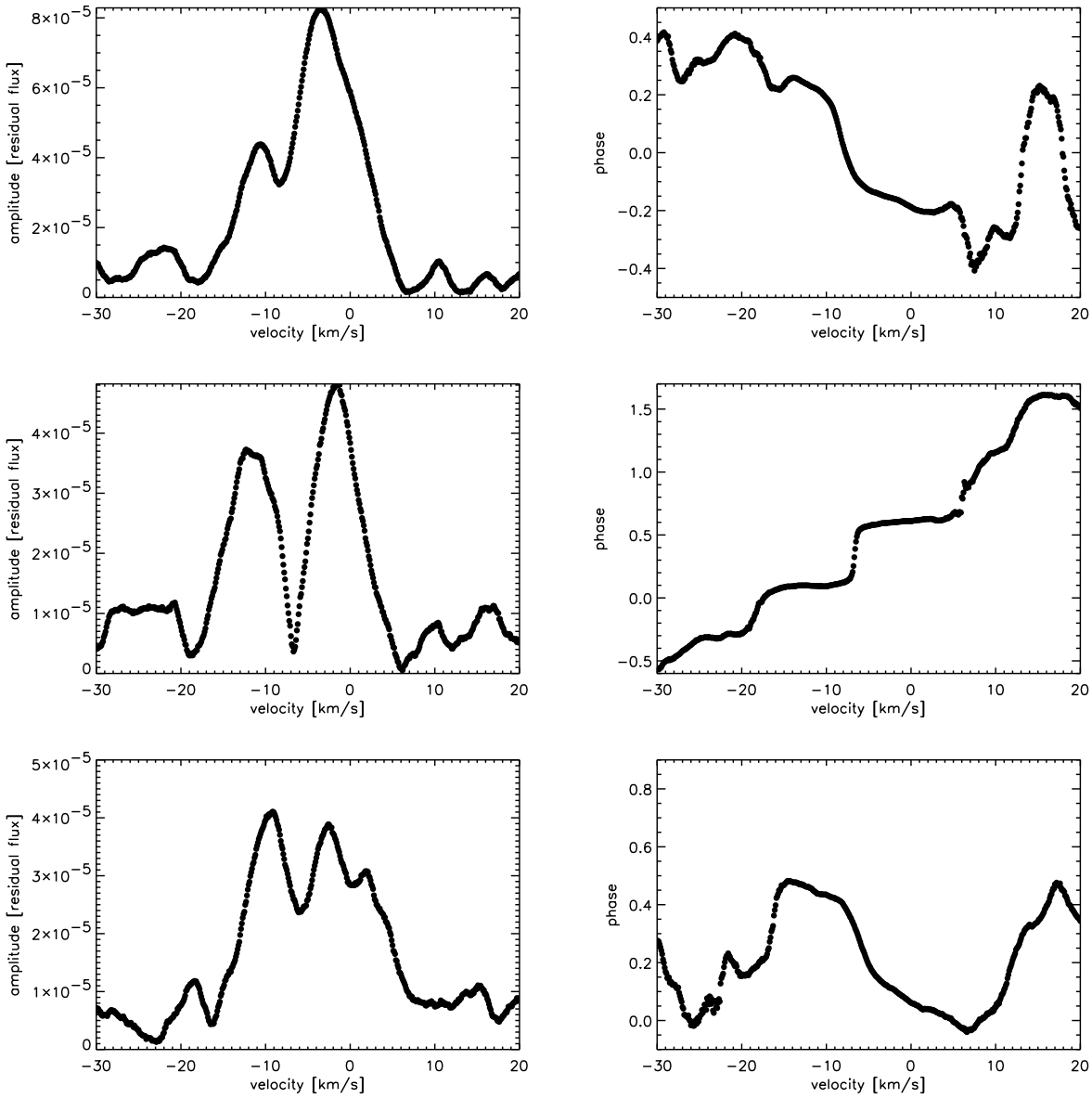

Figure 2.9: The amplitude (left) and phase (right) distributions as a function of velocity across the line profile of δ Eridani for three significant frequencies obtained from $\langle \mathrm{v} \rangle$: $\nu_{\langle \mathrm{v} \rangle} = 59.40$ c d^{-1} (687.5μHz) (top), $\nu_{\langle \mathrm{v} \rangle} = 61.08$ c d^{-1} (706.9μHz) (middle) and $\nu_{\langle \mathrm{v} \rangle} = 52.68$ c d^{-1} (609.7μHz) (bottom). The mean radial velocity of the star, is found to be approximately -6.3 km s^{-1}.

To simulate such an oscillator we follow the description of De Ridder et al. (2006a), and we compute

$$f(t) = B(t)\sin(2\pi\nu t) + C(t)\cos(2\pi\nu t), \tag{2.3}$$

where we let the amplitudes B and C vary with a first order autoregressive process in a discrete time domain with time step Δt:

$$B_n = e^{-\eta\Delta t}B_{n-1} + \varepsilon_{n+1} \tag{2.4}$$

where ε_{n+1} is a Gaussian distributed excitation kick. For more details we refer to De Ridder et al. (2006a). The above is applied to the equations for the pulsation velocity which are obtained by taking the time derivative of the displacement components mentioned in Section 3.2, Eq.(2) of De Ridder et al. (2002). Whenever rotation is neglected, the three spherical components of the pulsation velocity, i.e. υ_r, υ_θ and υ_φ, for the damped and re-exited case become:

$$\begin{aligned}\upsilon_r &= -\upsilon_{\rm osc}N_\ell^m P_\ell^m(\cos\theta) * \\ &\quad e^{-\eta(t-n\Delta t_{\rm kick})}(B_n\sin(m\varphi+2\pi\nu t) + C_n\cos(m\varphi+2\pi\nu t)),\end{aligned} \tag{2.5}$$

$$\begin{aligned}\upsilon_\theta &= -K\upsilon_{\rm osc}N_\ell^m\frac{\partial}{\partial\theta}(P_\ell^m(\cos\theta)) * \\ &\quad e^{-\eta(t-n\Delta t_{\rm kick})}(B_n\sin(m\varphi+2\pi\nu t) + C_n\cos(m\varphi+2\pi\nu t)),\end{aligned} \tag{2.6}$$

$$\begin{aligned}\upsilon_\varphi &= -mK\upsilon_{\rm osc}N_\ell^m\frac{1}{\sin\theta}P_\ell^m(\cos\theta) * \\ &\quad e^{-\eta(t-n\Delta t_{\rm kick})}(B_n\cos(m\varphi+2\pi\nu t) - C_n\sin(m\varphi+2\pi\nu t)),\end{aligned} \tag{2.7}$$

with $\upsilon_{\rm osc}$ proportional to the pulsation amplitude, N_ℓ^m the normalisation factor for the spherical harmonics $Y_\ell^m(\theta,\varphi) \equiv P_\ell^m(\cos\theta)e^{im\varphi}$ and K the ratio of the horizontal to the vertical velocity amplitude.

Line profiles with the same parameters as described in section 3.1 are generated with a damping time (η^{-1}) of two days (the estimate for ξ Hydrae by Stello et al. (2004)). The used pulsation amplitude is 0.04 km s^{-1}. The moments, with the dominant frequencies and the amplitude and phase distribution across the line profiles are investigated.

2.4.2 Frequencies

$\langle \mathrm{v} \rangle$, $\langle \mathrm{v}^2 \rangle$ and $\langle \mathrm{v}^3 \rangle$ are determined for the generated series of line profiles and the frequencies are obtained in the same way as described in section 3.1. Rather than fitting a Lorenz profile to the power spectrum, we simply used the highest peak to obtain the oscillation frequency. This implies that the obtained frequencies differ slightly from the input frequency as predicted by the Lorenzian probability distribution. The frequencies obtained from $\langle \mathrm{v}^3 \rangle$ are the same as the ones obtained for $\langle \mathrm{v} \rangle$, which is as expected from theory and also seen in the observations of the four red (sub)giants. None of the modes reveal a relation between the frequencies obtained from $\langle \mathrm{v} \rangle$ and $\langle \mathrm{v}^2 \rangle$, which is due to the small amplitudes as described in section 2.3.1.

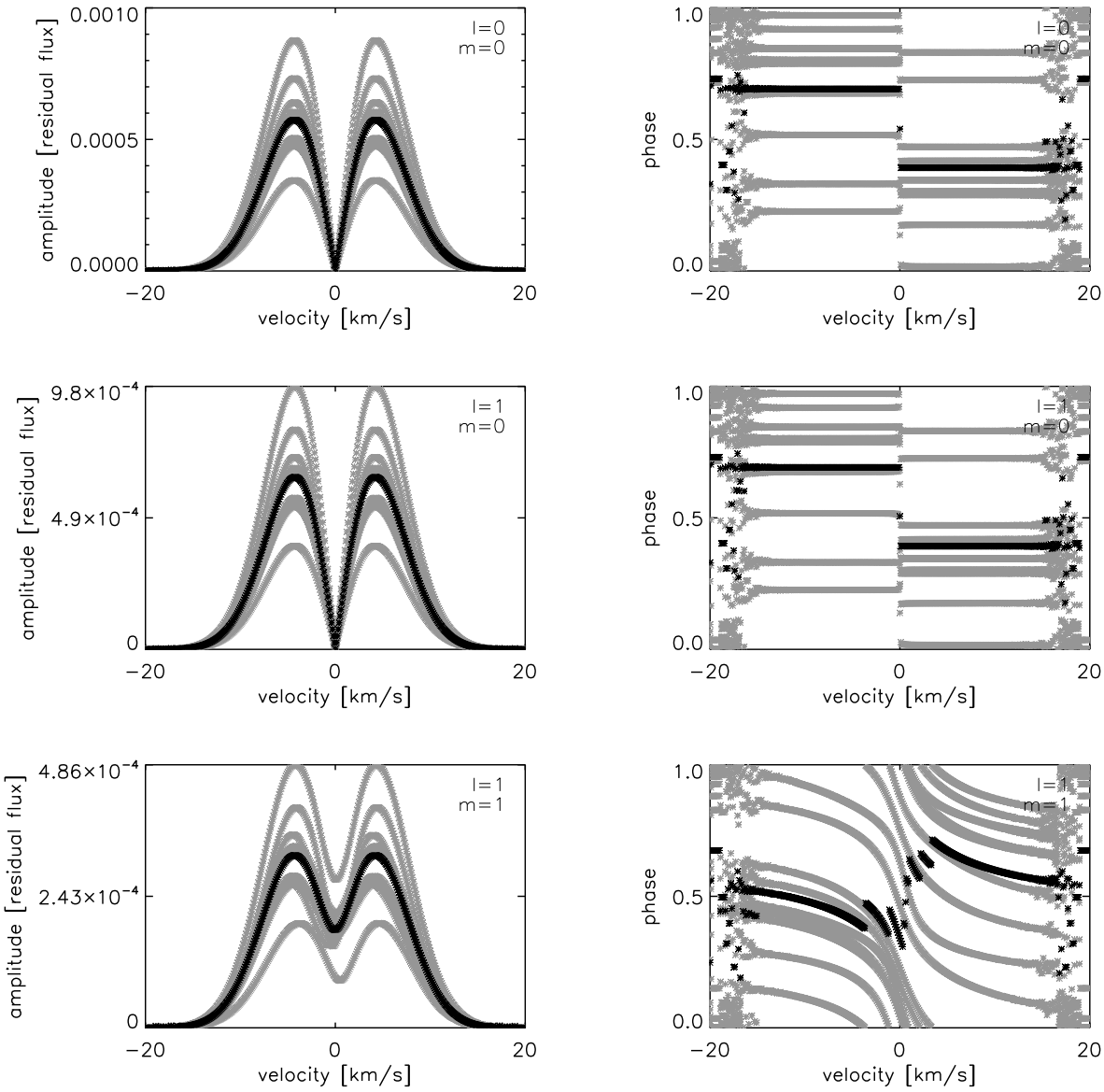

Figure 2.10: The amplitude (left) and phase (right) distributions for simulated line profiles with a two day damping time at an inclination angle of $i = 35°$. For each mode ten different realisations are shown in grey, with the average shown in black. Top: $\ell = 0$, $m = 0$, middle: $\ell = 1$, $m = 0$, bottom: $\ell = 1$, $m = 1$.

2.4.3 Amplitude and phase distribution

The amplitude and phase distribution as a function of the velocity across the line profiles are investigated for the simulated spectral lines. The profiles for the cases with $\ell = 0, 1, 2$ and positive m values, with a damping rate of $\eta = 2$ days, are shown in Fig. 2.10. The dominant frequency obtained from $\langle \mathrm{v} \rangle$ is used for the harmonic fits. This frequency is different for each realisation due to the stochastic nature of the forcing. For each mode ten realisations are shown

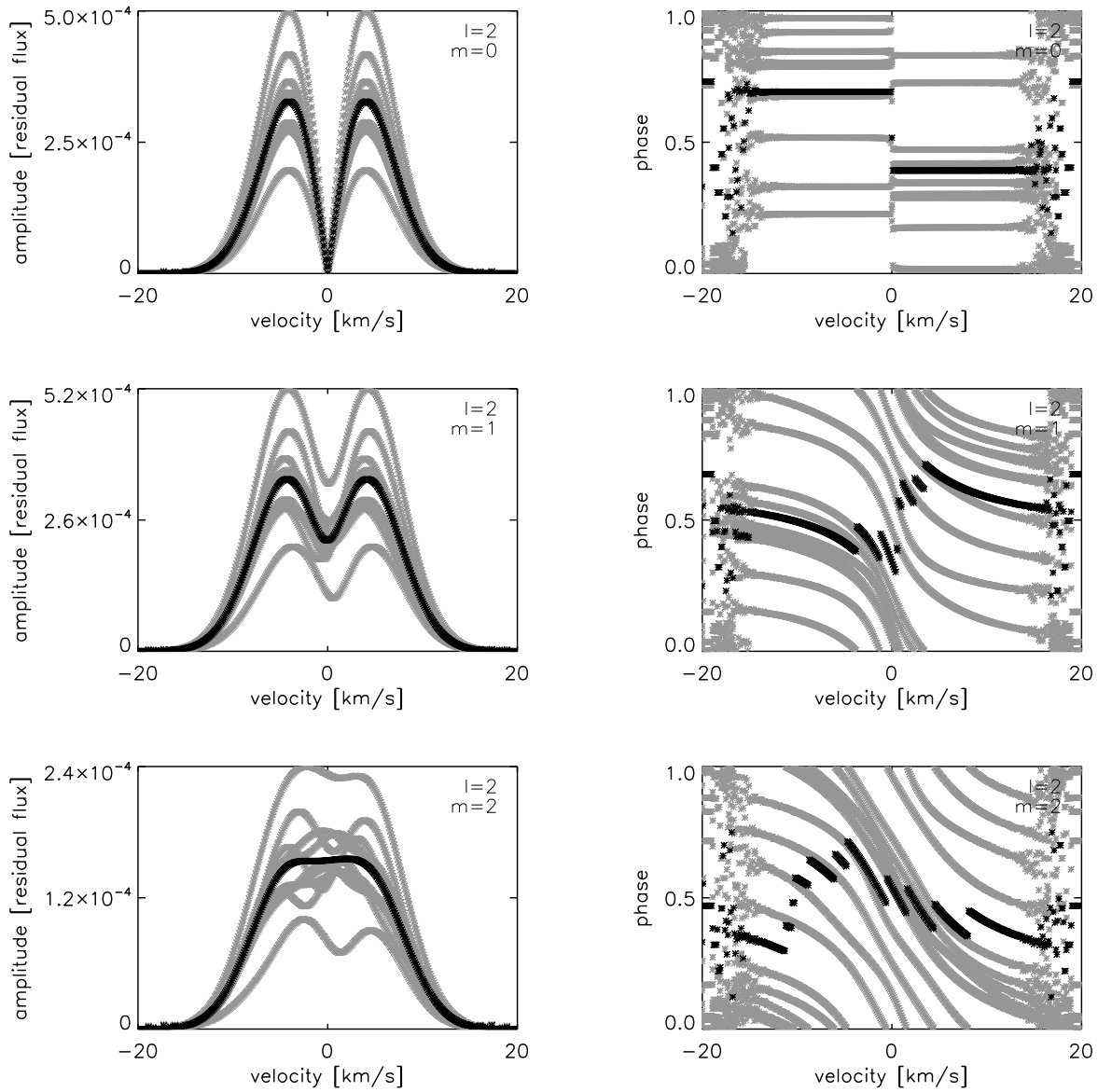

Figure 2.10: Continued. Top: $\ell = 2$, $m = 0$, middle: $\ell = 2$, $m = 1$, bottom: $\ell = 2$, $m = 2$.

in grey, with the average shown in black. The shape of the amplitude of axisymmetric and tesseral modes do not change, although the amplitudes per velocity pixel can have different values for different realisations. The drop to zero amplitude in the centre of the line is very characteristic for all the amplitude distributions. However, for the sectoral modes, the shape and value of the amplitudes may be different for different realisations and the amplitude distribution does not necessarily drop in the centre of the line for such modes. The behaviour does not change significantly with inclination angle.

2.5 INTERPRETATION

The amplitude distribution across the line profile is used for mode identification, as in Telting et al. (1997) and De Cat et al. (2005). For each star we find different distributions for different dominant mode frequencies. This clearly indicates that modes with different wavenumbers (ℓ, m) must be present in the data. Thus, we detect non-radial modes in the observed cross-correlation profiles. In order to identify the wavenumbers of the individual modes, observed amplitude distributions are compared with simulated ones, as is commonly done for mode identification. Only very recently, Zima (2006) implemented a statistical measure to quantify the identification of (ℓ, m) as a function of amplitude across the profile for modes with infinite lifetime. A similar quantitative measure in the case of damped oscillations is not yet available, but visual inspection of amplitude diagrams allows a clear discrimination between axisymmetric and non-axisymmetric modes which is what we do here, based on simulations. The averaged amplitudes over different realisations (indicated in black in Fig. 2.10) are used for this comparison, keeping in mind that the observations are single realisations. Due to the fact that single realisations of different modes are in some cases comparable, different sets of wavenumbers are occasionally likely for observed modes.

For ϵ Ophiuchi the amplitude of the first frequency $\nu = 5.03$ c d^{-1} (58.2μHz) resembles the one of modes with $\ell = 2$, $m = 2$. The mode with frequency $\nu = 5.46$ c d^{-1} (63.2μHz) resembles an $m = 1$ mode, although it does not exclude an $m = 0$ mode. The mode with $\nu = 5.83$ c d^{-1} (67.5μHz) resembles an $\ell = 2$, $m = 2$ mode.

The modes with frequency $\nu = 11.17$ c d^{-1} (129.3μHz) and $\nu = 11.71$ c d^{-1} (135.5μHz) obtained for η Serpentis resemble a realisation of the $\ell = 2$, $m = 2$ mode, while the mode with the third frequency ($\nu = 10.38$ c d^{-1} (102.2μHz)) is likely to have $m = 0$.

For ξ Hydrae the most dominant frequency $\nu = 8.42$ c d^{-1} (97.5μHz) reveals a mode with either $m = 0$ or $m = 1$.

For δ Eridani the dominant mode ($\nu = 59.40$ c d^{-1} (687.5μHz)) resembles an $m = 1$, while the second one ($\nu = 61.08$ c d^{-1} (706.9μHz)) is characteristic for an $m = 0$ mode. The third mode ($\nu = 52.68$ c d^{-1} (609.7μHz)) shows an additional dip in the second peak, but $m = 1$ as well as $m = 0$ seem to be possible.

From the comparison of the observations with the simulations we can conclude that we see modes with $m \neq 0$ and thus non-radial modes among the dominant modes in the (sub)giants. This result is robust against a change in the value of the inclination angle for the simulations.

2.6 DISCUSSION AND CONCLUSIONS

We have implemented a line profile generation code for damped and re-excited solar-like oscillations. We found that the quantities $\langle \mathrm{v} \rangle$, $\langle \mathrm{v}^3 \rangle$ and amplitude across the profile are good line diagnostics to characterise these oscillations. Our simulations were made for a single line-forming region while we compared them with cross-correlation profiles based on a mask. For this reason, the phase variations across the profile are difficult to interpret, since they are an average over the depth in the atmosphere, and this average depends on the shape of the eigenfunctions. Moreover, we learned from our simulations that the phase behaviour can be quite different for realisations, as illustrated in Fig. 2.10. More extensive simulations across the depth would be needed to interpret the observed phase behaviour in detail. In order to do so, we would need to know the shape of the excited eigenmodes as a function of depth in the outer regions of the star.

From the frequency analysis performed on the bisector velocity span, it becomes clear that it is not a good diagnostic to unravel solar-like oscillations.

Individual mode identification is not yet possible with the method used in the present work. This is not surprising because we did a first exploration of how well-working methods for modes with infinite lifetimes could be adapted for damped oscillations. The discriminant of the moments is not useful at the low amplitudes present in the (sub)giants investigated in the present work. Nevertheless, from the resemblance between the observed amplitude distribution with the simulated ones, and comparison between different modes of the same star, we presented clear observational evidence for modes with different m-values in the same star for three of our four examples, i.e. non-radial modes are present in red (sub)giants. The amplitudes for ξ Hydrae are too low to make firm conclusions, and since we see only one frequency in the line profile variations, a comparison of the amplitude shapes for different modes is not possible. Therefore we can not exclude that this star has only radial modes as proposed by Frandsen et al. (2002).

Dziembowski et al. (2001) and Houdek & Gough (2002) show theoretically that stochastically excited radial pulsation modes are most likely to be observed in red giants. They predict that, for non-radial modes, damping effects will have influence in the p-mode cavity as well as in the g-mode cavity, while for radial modes only damping in the p-mode cavity is present. Therefore, according to this theory, radial modes are less severely influenced by damping than non-radial modes. Our result pointing towards the presence of non-radial modes, calls for a re-evaluation of the theoretical predictions.

ACKNOWLEDGEMENT

SH wants to thank the staff at the Instituut voor Sterrenkunde at the Katholieke Universiteit Leuven for their hospitality during her three month visit. JDR is a postdoctoral fellow of the fund for Scientific Research, Flanders. FC was supported financially by the Swiss National Science Foundation. The authors are supported by the Fund for Scientific Research of Flanders (FWO) under grant G.0332.06 and by the Research Council of the University of Leuven under grant GOA/2003/04.

REFERENCES

Aerts, C. 1996, A&A, 314, 115

Aerts, C. & De Cat, P. 2003, Space Science Reviews, 105, 453

Aerts, C., De Pauw, M., & Waelkens, C. 1992, A&A, 266, 294

Baranne, A., Queloz, D., Mayor, M., et al. 1996, A&AS, 119, 373

Barban, C., De Ridder, J., Mazumdar, A., et al. 2004, in ESA SP-559: SOHO 14 Helio- and Asteroseismology: Towards a Golden Future, 113

Bedding, T. R. & Kjeldsen, H. 2003, Publications of the Astronomical Society of Australia, 20, 203

Bouchy, F. & Carrier, F. 2001, The Messenger, 106, 32

Bouchy, F. & Carrier, F. 2003, Ap&SS, 284, 21

Bouchy, F., Pepe, F., & Queloz, D. 2001, A&A, 374, 733

Breger, M., Handler, G., Garrido, R., et al. 1999, A&A, 349, 225

Briquet, M. & Aerts, C. 2003, A&A, 398, 687

Brown, T. M., Kotak, R., Horner, S. D., et al. 1998, ApJS, 117, 563

Carrier, F., Bouchy, F., & Eggenberger, P. 2003, in Asteroseismology Across the HR Diagram, ed. M. J. Thompson, M. S. Cunha, & M. J. P. F. G. Monteiro, 311–314

Carrier, F., Eggenberger, P., De Ridder, J., et al. 2006, A&A, in preparation

Chadid, M., De Ridder, J., Aerts, C., & Mathias, P. 2001, A&A, 375, 113

Dall, T. H., Santos, N. C., Arentoft, T., Bedding, T. R., & Kjeldsen, H. 2006, A&A, 454, 341

De Cat, P., Briquet, M., Daszyńska-Daszkiewicz, J., et al. 2005, A&A, 432, 1013

De Ridder, J., Arentoft, T., & Kjeldsen, H. 2006a, MNRAS, 365, 595

De Ridder, J., Barban, C., Carrier, F., et al. 2006b, A&A, 448, 689

De Ridder, J., Dupret, M.-A., Neuforge, C., & Aerts, C. 2002, A&A, 385, 572

Dziembowski, W. A. 1971, Acta Astronomica, 21, 289

Dziembowski, W. A., Gough, D. O., Houdek, G., & Sienkiewicz, R. 2001, MNRAS, 328, 601

ESA. 1997, VizieR Online Data Catalog, 1239, 0

Frandsen, S., Carrier, F., Aerts, C., et al. 2002, A&A, 394, L5

Glebocki, R. & Stawikowski, A. 2000, Acta Astronomica, 50, 509

Gray, D. F. 2005, PASP, 117, 711

Houdek, G., Balmforth, N. J., Christensen-Dalsgaard, J., & Gough, D. O. 1999, A&A, 351, 582

Houdek, G. & Gough, D. O. 2002, MNRAS, 336, L65

Kjeldsen, H., Bedding, T. R., Viskum, M., & Frandsen, S. 1995, AJ, 109, 1313

Kuschnig, R., Weiss, W. W., Gruber, R., Bely, P. Y., & Jenkner, H. 1997, A&A, 328, 544

Marcy, G. W. & Butler, R. P. 2000, PASP, 112, 137

Martínez Fiorenzano, A. F., Gratton, R. G., Desidera, S., Cosentino, R., & Endl, M. 2005, A&A, 442, 775

Mathias, P. & Aerts, C. 1996, A&A, 312, 905

Mathias, P., Aerts, C., De Pauw, M., Gillet, D., & Waelkens, C. 1994, A&A, 283, 813

Pepe, F., Bouchy, F., Queloz, D., & Mayor, M. 2003, in ASP Conf. Ser. 294: Scientific Frontiers in Research on Extrasolar Planets, 39–42

Queloz, D., Henry, G. W., Sivan, J. P., et al. 2001a, A&A, 379, 279

Queloz, D., Mayor, M., Udry, S., et al. 2001b, The Messenger, 105, 1

Scargle, J. D. 1982, ApJ, 263, 835

Schrijvers, C., Telting, J. H., Aerts, C., Ruymaekers, E., & Henrichs, H. F. 1997, A&AS, 121, 343

Setiawan, J., Hatzes, A. P., von der Lühe, O., et al. 2003, A&A, 398, L19

Stello, D., Kjeldsen, H., Bedding, T. R., & Buzasi, D. 2006, A&A, 448, 709

Stello, D., Kjeldsen, H., Bedding, T. R., et al. 2004, Sol. Phys., 220, 207

Taylor, B. J. 1999, A&AS, 134, 523

Telting, J. H., Aerts, C., & Mathias, P. 1997, A&A, 322, 493

van Hamme, W. 1993, AJ, 106, 2096

Zima, W. 2006, A&A, 455, 227

CHAPTER 3

Precise radial velocities of giant stars. I. Stable stars

S. Hekker, S. Reffert, A. Quirrenbach, D.S. Mitchell, D.A. Fischer, G.W. Marcy and R.P. Butler

Astronomy & Astrophysics 2006, 454, 943

FUTURE astrometric missions such as SIM PlanetQuest need very stable reference stars. K giants have large luminosities, which place them at large distances and thus the jitter of their photocenters by companions is relatively small. Therefore K giants would be best suited as references. To confirm this observationally a radial velocity survey is performed to quantify the level of intrinsic variability in K giants. From this radial velocity survey we present 34 K giants with an observed standard deviation of the radial velocity of less than 20 $\mathrm{m\,s^{-1}}$. These stars are considered "stable" and can be used as radial velocity standards. The radial velocity survey contains 179 K giants. All K giants have a declination between -30° and $+65^\circ$ and visual magnitude of $3-6$ mag. The Coudé Auxiliary Telescope (CAT) at University of California Observatories / Lick Observatory is used to obtain radial velocities with an accuracy of $5-8$ $\mathrm{m\,s^{-1}}$. The number of epochs for the 34 stable stars ranges from 11 to 28 with a total timespan of the observations between 1800 and a little over 2200 days. The observational results of the 34 "stable" stars are shown together with a discussion about their position in the M_V vs. $B-V$ diagram and some conclusions concerning the radial velocity variability of K giants. These results are in agreement with the theoretical predictions. K giants in a certain range of the M_V vs. $B-V$ diagram are suitable reference stars.

3.1 INTRODUCTION

To perform high precision astrometric observations very stable reference stars are needed. In preparation of the Space Interferometry Mission (SIM PlanetQuest), Frink et al. (2001) investigated which type of stars would be best suited as reference stars. Although known to be photospherically active, K giants appeared to be the best choice, mainly because of their large distances, brightness and sky coverage. To quantify the photospheric activity observationally, a radial velocity survey was started to measure the level of intrinsic radial velocity variability in K giant stars.

For about a decade, well known techniques have been used to perform very accurate radial velocity observations, up to a few $\mathrm{m\,s^{-1}}$ (see e.g. Marcy & Butler 2000; Queloz et al. 2001) and with HARPS (High Accuracy Radial velocity Planet Searcher on the 3.6 m telescope, La Silla Observatory, ESO Chile) even to 1 $\mathrm{m\,s^{-1}}$ (Pepe et al. 2003). Most extrasolar planets known so far have been discovered around main sequence stars using radial velocity observations. Like main sequence stars, K giant spectra contain a large number of narrow spectral lines and accurate radial velocity variations can also be obtained for these stars.

In this paper we present results for 34 K giants, from the above-mentioned survey, with an observed standard deviation of the radial velocity of less than 20 $\mathrm{m\,s^{-1}}$. These stars are considered stable and can be used as radial velocity standards.

In general the possibility of accurate radial velocity observations makes it possible and necessary to select radial velocity standards with smaller radial velocity variations. The IAU standard stars (Pearce 1955) and the suggested extensions by Heard (1968) and Evans (1968) for the northern and southern sky respectively do not yet have an accuracy of a few $\mathrm{m\,s^{-1}}$. More recently Kharchenko et al. (2004) selected 3967 stars from their "Catalog of radial velocities of galactic stars with high precision astrometric data (CRVAD)" (based on Barbier-Brossat & Figon 2000) as radial velocity standard candidates. Furthermore Udry et al. (1999a,b) present a list of CORAVEL radial velocity standard stars, and a list with proposed high-precision radial velocity standards, respectively. The stars presented in this paper are in addition to the already known radial velocity standard stars.

The paper is organized as follows. In Section 2 the observations are described, followed in Section 3 by the results for the individual stars. Section 4 contains a discussion and some conclusions concerning the radial velocity variability of K giants.

3.2 OBSERVATIONS

The sample of 179 K giants has been selected from the Hipparcos catalog (ESA 1997) based on the criteria described in Frink et al. (2001). They are all brighter than 6 mag, presumably single, and have masses ranging from about 1 to 3 solar masses. In Table 3.1 properties of the 34 stable stars are listed.

Our ongoing K giant radial velocity survey started in June 1999, with the Coudé Auxiliary Telescope (CAT) in conjunction with the Hamilton high resolution (R=60 000) échelle spectrograph. An iodine cell is placed in the light path. With integration times of up to thirty minutes for the faintest stars we reach a signal to noise ratio of about $80 - 100$, yielding a radial velocity precision of $5 - 8$ $\mathrm{m\,s^{-1}}$. This is adequate for our survey and hence no attempt has been

made to reach the 3 m s^{-1} accuracy which is in principle possible with this setup (Butler et al. 1996). The pipeline described by Butler et al. (1996) is used. A template iodine spectrum and a template spectrum of the target star obtained without an iodine cell in the lightpath are used to model the stellar observations obtained with an iodine cell in the lightpath. The Doppler shift is a free parameter in this model and determined as the shift of the template stellar spectrum to obtain the best model for the observed spectra. With this method the radial velocity itself is not measured. Only the change in the radial velocity with respect to the stellar template is obtained with a precision of a few m s^{-1}. The mean radial velocities of the stars are known with an accuracy of the order of a few tenths of km s^{-1} from for instance Famaey et al. (2005) and Barbier-Brossat & Figon (2000). The radial velocities from Famaey et al. (2005) were obtained with the CORAVEL spectrovelocimeter mounted on the Swiss 1.2 m-telescope at the Observatoire Haute Provence, France. These are more accurate than the ones from Barbier-Brossat & Figon (2000), but not available for all stars in our sample. The latter catalog is an extension of the WEB Catalog of Radial Velocities (Duflot et al. 1995).

3.3 RESULTS

34 stars out of the sample of 179 stars have an observed standard deviation of the radial velocity of less than 20 m s^{-1}. The exact value of this threshold is somewhat arbitrary. It is set by a visual inspection of the radial velocity variations observed in our sample. Stars without systematic radial velocity variations or trends all happen to have an observed standard deviation of the radial velocity of less than 20 m s^{-1}. Furthermore, selecting reference stars for SIM PlanetQuest with radial velocity variations smaller than 20 m s^{-1} would result in an acceptable 3.6% contamination of the reference star grid with binary stars (Frink et al. 2001). Plots of the radial velocity variation are shown in Figure 3.1. The numbers in the upper right corner of each frame denote the observed standard deviation ($\sigma_{\rm std}$, upper number) and the mean error ($\sigma_{\rm me}$, lower number) of the radial velocity observations. The latter is derived from the rms scatter of hundreds of individual "chunks" of the spectrum, typically 2 Ångstrom. In Table 3.2, for each of the 34 stable stars the mean error, number of observations, and timespan of the observations in this survey are listed together with the observed standard deviation, intrinsic standard deviation (which is obtained by quadratically subtracting the mean error from the total observed radial velocity scatter), and the reduced χ^2. Furthermore a flag is set to K for stars also present among the 3967 candidate standards presented by Kharchenko et al. (2004). In case the flag is set to N, there are not enough observations in Kharchenko et al. (2004) to make it a radial velocity standard candidate, but all other parameters do match their stability criteria.

All other stars in the sample show radial velocity variations larger than 20 m s^{-1}. Around one star a sub-stellar companion has been discovered (ι Draconis, Frink et al. 2002). The highly non-sinusoidal radial velocity variation observed for this star can only be induced by a companion with high eccentricity and not by stellar activity. This star also shows a long-term trend indicating a third component in the system. About 23 spectroscopic binaries are present. Some are already known in the literature, but some were not observed before and will be presented in a forthcoming paper. Furthermore, about 35 stars with sinusoidal periodic variations are present (Hekker et al. 2006), among which four show an additional long trend indicating a binary in a wide orbit. The nature of these sinusoidal periodic variations is under investigation. For at least

four stars there are strong arguments that the presence of nearly sinusoidal variations of the radial velocity are most likely caused by sub-stellar companions. Two of the stars with very large radial velocity variations of several km s^{-1} appear to be supergiants. A summary of the whole program will be presented in a forthcoming paper.

3.4 DISCUSSION AND CONCLUSIONS

To obtain more information on the type of stars that appear to be stable, all 179 stars from this survey are plotted in an $M_{\rm V}$ vs. $B-V$ diagram, see Figure 3.2. A box is drawn around the stable stars. The box contains 11 binaries, 3 variable stars with long trends indicating that they are binaries, and 73 other stars among which the 34 stable stars. The binaries and variable stars with a long trend are excluded in the further discussion.

The stable stars are not homogeneously distributed in the $M_{\rm V}$ vs. $B-V$ diagram but they all have a $B-V$ colour less than 1.2. This is shown in Figure 3.3, where the standard deviation of the radial velocity is plotted as a function of $B-V$ colour. The majority of the bluer stars show smaller variations in the radial velocity than the redder ones. This increase of the radial velocity variability with $B-V$ colour, first described by Frink et al. (2001), is consistent with similar trends of photometry and radial velocity variability with spectral type (Hatzes & Cochran (1998), Larson et al. (1999), Nidever et al. (2002)). These results are also in good agreement with the results by Henry et al. (2000). They obtained photometric observations of 187 G, K and M0 field giants and show that "stable" giants with a short-term standard deviation less than 0.0020 mag have a $B-V$ less than 1.35. They note that nearly all stable giants are on the left side of the coronal dividing line (CDL). The CDL separates the giants with hot coronae on the left from giants with cool, massive winds on the right (Linsky & Haisch 1979; Haisch 1999).

3.4.1 Statistics

In Figure 3.4, a histogram of the standard deviation of the radial velocity from the stars in the box (Figure 3.2) is shown. Nearly half of the stars have a radial velocity with a standard deviation less than 20 m s^{-1}, 90 % less than 50 m s^{-1} and 96 % less than 100 m s^{-1}. By selecting stars from the region in the colour-magnitude diagram outlined by this box, it is thus possible to construct samples of K giants with small radial velocity variations.

3.4.2 Variability

For each star the standard deviation of the observed radial velocities, although small, is significantly larger than the measurement errors, which implies that the stars show low-level radial velocity variations. To quantify this a χ^2 test is performed to obtain the probability of the reality of this variability. The reduced χ^2 values are listed in Table 3.2. 31 of the 34 stars have a $> 99.9\%$ probability of variability, for the other 3 the probability is $> 99\%$. The presence of variability is consistent with the findings of Barban et al. (2004) who detected solar-like oscillations in two red giant stars. One of these stars, HIP89962 / HD168723, is also present in our

Table 3.1: Properties of the stable stars: right ascension (ra) in "hh:mm:ss" and declination (dec) in "dd:mm:ss", both J2000.0, apparent magnitude ($m_{\rm V}$) and absolute magnitude ($M_{\rm V}$) in the V band, parallax (plx) in mas, $B-V$ colour, (rather uncertain) mass obtained with the method described by Allende Prieto & Lambert (1999) in $M_\odot$, the spectral type (SP) and the radial velocity (RV) in km s^{-1} from Famaey et al. (2005) and Barbier-Brossat & Figon (2000), respectively. The latter catalog does not give errors in the radial velocity for each star.

HIP	HD	ra	dec	$m_{\rm V}{}^a$	$M_{\rm V}$	plx^a	$B-V^a$	mass	SP^a	$RV^{\,b}$	RV^c
		hh:mm:ss	dd:mm:ss	mag	mag	mas	mag	$M_\odot$		[km s^{-1}]	[km s^{-1}]
HIP4906	HD6186	01 02 56.6	+07 53 25	4.27	0.44	17.14	0.952	2.27	K0III	7.47 ± 0.20	7.50 ± 0.2
HIP13701	HD18322	02 56 25.7	−08 53 53	3.89	0.83	24.49	1.088	1.38	K1III-IV		−20.30
HIP14838	HD19787	03 11 37.8	+19 43 36	4.35	0.79	19.44	1.033	1.91	K2III	23.05 ± 0.20	23.90 ± 0.4
HIP19388	HD26162	04 09 10.0	+19 36 33	5.51	0.76	11.21	1.077	1.39	K2III	24.75 ± 0.02	24.80
HIP21248	HD29085	04 33 30.6	−29 45 59	4.49	1.58	26.22	0.972	1.98	K0III		20.60
HIP22860	HD31414	04 55 06.8	−16 44 26	5.71	−0.11	6.85	0.953	3.01	K0II		9.80
HIP33914	HD52556	07 02 17.5	+15 20 10	5.78	−0.70	5.06	1.140	3.06	K1III	-12.85 ± 0.20	−13.50
HIP36848	HD60666	07 34 34.8	−27 00 44	5.78	0.87	10.41	1.045	1.71	K1III		-6.20 ± 0.3
HIP37447	HD61935	07 41 14.8	− 09 33 04	3.94	0.71	22.61	1.022	1.94	K0III		10.50
HIP38375	HD64152	07 51 43.0	−21 10 25	5.62	1.00	11.90	0.956	2.50	K0III		31.90
HIP43923	HD76291	08 56 50.0	+45 37 54	5.72	1.48	14.21	1.125	1.30	K1IV	53.28 ± 0.30	58.40 ± 0.3
HIP48455	HD85503	09 52 45.8	+26 00 25	3.88	0.83	24.52	1.222	0.59	K0III	13.63 ± 0.07	14.10 ± 0.3
HIP53316	HD94481	10 54 17.8	−13 45 29	5.65	0.16	7.97	0.832	2.89	K0III		5.40
HIP58181	HD103605	11 55 58.4	+56 35 55	5.83	0.90	10.34	1.101	1.45	K1III	16.91 ± 0.16	14.70 ± 1.2
HIP59847	HD106714	12 16 20.5	+23 56 43	4.93	0.52	13.12	0.957	2.27	K0III	-27.89 ± 0.13	-27.20 ± 0.5
HIP60742	HD108381	12 26 56.3	+28 16 06	4.35	0.76	19.18	1.128	1.66	K2III	3.38 ± 0.11	4.70 ± 0.3
HIP68895	HD123123	14 06 22.3	−26 40 57	3.25	0.79	32.17	1.091	1.76	K2III		27.20 ± 0.5
HIP74239	HD134373	15 10 18.6	−26 19 57	5.75	0.05	7.25	1.045	2.78	K0III		-33.10 ± 0.3
HIP75944	HD138137	15 30 40.4	−16 36 34	5.82	−0.37	5.78	1.056	2.94	K0III		−1.70
HIP78132	HD142980	15 57 14.6	+14 24 52	5.54	1.33	14.36	1.141	1.19	K1IV	-70.98 ± 0.17	−68.30
HIP78442	HD143553	16 00 61.1	+04 25 39	5.82	1.49	13.62	1.003	1.93	K0III	-7.85 ± 0.22	−4.10
HIP83000	HD153210	16 57 10.1	+09 22 30	3.19	1.09	37.99	1.160	0.78	K2III	-55.86 ± 0.19	-54.40 ± 1.3
HIP88684	HD165438	18 06 15.2	−04 45 05	5.74	3.02	28.61	0.968	1.35	K1IV		−18.90

[a] The Hipparcos and Tycho Catalogues (ESA 1997)
[b] Radial velocities for 6691 K and M giants (Famaey et al. 2005)
[c] General Catalog of mean radial velocities (Barbier-Brossat & Figon 2000)

Table 3.1: Continued.

HIP	HD	ra	dec	$m_{\rm V}{}^a$	$M_{\rm V}$	plx^a	$B-V^a$	mass	SP^a	$RV^{\,b}$	RV^c
		hh:mm:ss	dd:mm:ss	mag	mag	mas	mag	$M_\odot$		[km s^{-1}]	[km s^{-1}]
HIP89962	HD168723	18 21 18.6	−02 53 56	3.23	1.84	52.81	0.941	1.96	K0III-IV		8.90 ± 0.7
HIP90496	HD169916	18 27 58.2	−25 25 18	2.82	0.95	42.20	1.025	1.88	K1III		-43.20 ± 0.7
HIP93085	HD175775	18 57 43.8	−21 06 24	3.52	−1.77	8.76	1.151	4.58	K0II-III		-20.10 ± 0.6
HIP94779	HD181276	19 17 06.2	+53 22 06	3.80	0.91	26.48	0.950	2.87	K0III	-29.00 ± 0.30	-29.20 ± 0.6
HIP96229	HD184406	19 34 05.4	+07 22 44	4.45	1.80	29.50	1.176	0.92	K3III	-24.73 ± 0.13	-23.90 ± 0.6
HIP96459	HD185351	19 36 38.0	+44 41 42	5.17	2.13	24.64	0.928	1.82	K0III	-5.91 ± 0.11	-5.20 ± 1.0
HIP102422	HD198149	20 45 17.4	+61 50 20	3.41	2.63	69.73	0.912	1.64	K0IV	-87.55 ± 0.11	-87.90 ± 0.6
HIP106039	HD204381	21 28 43.4	−21 48 26	4.50	0.80	18.18	0.889	3.46	K0III		-20.80 ± 0.8
HIP112724	HD216228	22 49 40.8	+66 12 01	3.50	0.76	28.27	1.053	1.61	K0III	-12.59 ± 0.20	-14.20 ± 0.7
HIP115438	HD220321	23 22 58.2	−20 06 02	3.96	0.48	20.14	1.082	2.06	K0III		-6.10 ± 0.4
HIP115830	HD220954	23 27 58.1	+06 22 44	4.27	0.83	20.54	1.062	1.54	K1III	6.05 ± 0.19	6.50 ± 1.8

[a]The Hipparcos and Tycho Catalogues (ESA 1997)
[b]Radial velocities for 6691 K and M giants (Famaey et al. 2005)
[c]General Catalog of mean radial velocities (Barbier-Brossat & Figon 2000)

Table 3.2: Observational results of the 34 stable stars: the mean error of the individual observations for each star in $\mathrm{m\,s^{-1}}$, the number of observations (N), the time span of the observations in days, the standard deviation of the radial velocity (σ) in $\mathrm{m\,s^{-1}}$, the intrinsic scatter (σ_{int}) obtained by quadratically subtracting the mean error from the total observed radial velocity scatter, the reduced χ^2 and a flag. This flag is set to K for all stars also present among the 3967 candidate standards presented by Kharchenko et al. (2004). The flag is set to N for the stars with less than 4 observations in Kharchenko et al. (2004) which do otherwise match their criteria. If the flag is blank a photometric variability flag is present in the Tycho 1 catalog (ESA 1997) and these stars are therefore not included in the Kharchenko et al. (2004) candidate standard star catalog. More details about the selection method used by Kharchenko et al. (2004) are described in the text.

HIP	HD	mean error $[\mathrm{m\,s^{-1}}]$	N	timespan [days]	σ $[\mathrm{m\,s^{-1}}]$	σ_{int} $[\mathrm{m\,s^{-1}}]$	χ^2_{r}	flag
HIP4906	HD6186	5.2	19	1837	15.9	15.0	9.2	
HIP13701	HD18322	5.0	28	1806	14.9	14.0	8.6	
HIP14838	HD19787	4.7	18	1803	12.3	11.4	8.3	
HIP19388	HD26162	5.7	18	2222	16.2	15.2	7.6	K
HIP21248	HD29085	6.1	16	1832	15.7	14.5	7.5	
HIP22860	HD31414	7.8	19	2216	12.2	9.4	2.4	N
HIP33914	HD52556	6.8	20	1877	18.2	16.9	6.6	K
HIP36848	HD60666	8.4	11	1874	16.6	14.3	3.8	K
HIP37447	HD61935	5.0	14	1839	15.5	14.7	9.6	
HIP38375	HD64152	6.9	11	1897	15.9	14.3	5.8	N
HIP43923	HD76291	7.1	13	1718	14.4	12.5	4.1	K
HIP48455	HD85503	4.3	14	1458	20.0	19.5	23.6	
HIP53316	HD94481	10.3	11	1814	16.1	12.4	2.3	N
HIP58181	HD103605	6.5	13	1951	12.7	10.9	4.2	K
HIP59847	HD106714	7.5	14	1882	11.1	8.2	2.6	K
HIP60742	HD108381	5.4	16	1545	12.4	11.2	5.8	
HIP68895	HD123123	5.2	16	1688	19.8	19.1	14.9	
HIP74239	HD134373	7.7	15	1935	15.3	13.2	4.5	K
HIP75944	HD138137	7.4	16	1933	16.1	14.3	3.3	N
HIP78132	HD142980	5.6	16	1932	19.0	18.2	12.0	K
HIP78442	HD143553	5.7	16	1933	13.2	11.9	5.4	N
HIP83000	HD153210	4.5	17	1872	16.7	16.1	13.4	
HIP88684	HD165438	5.7	20	2200	17.9	17.0	10.8	N
HIP89962	HD168723	5.2	18	1876	13.4	12.4	7.0	
HIP90496	HD169916	5.0	18	1879	12.8	11.8	7.0	
HIP93085	HD175775	5.6	17	1899	17.0	16.1	8.4	
HIP94779	HD181276	4.8	18	1835	9.9	8.7	4.7	
HIP96229	HD184406	4.6	19	1843	17.0	16.4	14.3	
HIP96459	HD185351	5.6	25	2233	9.7	7.9	3.4	K
HIP102422	HD198149	5.1	20	1874	10.4	9.1	4.8	
HIP106039	HD204381	5.9	18	1908	8.8	6.5	2.1	
HIP112724	HD216228	4.4	20	1839	12.1	11.3	8.2	K
HIP115438	HD220321	5.2	21	1836	19.4	18.7	14.7	K
HIP115830	HD220954	4.7	18	1904	12.4	11.5	7.2	K

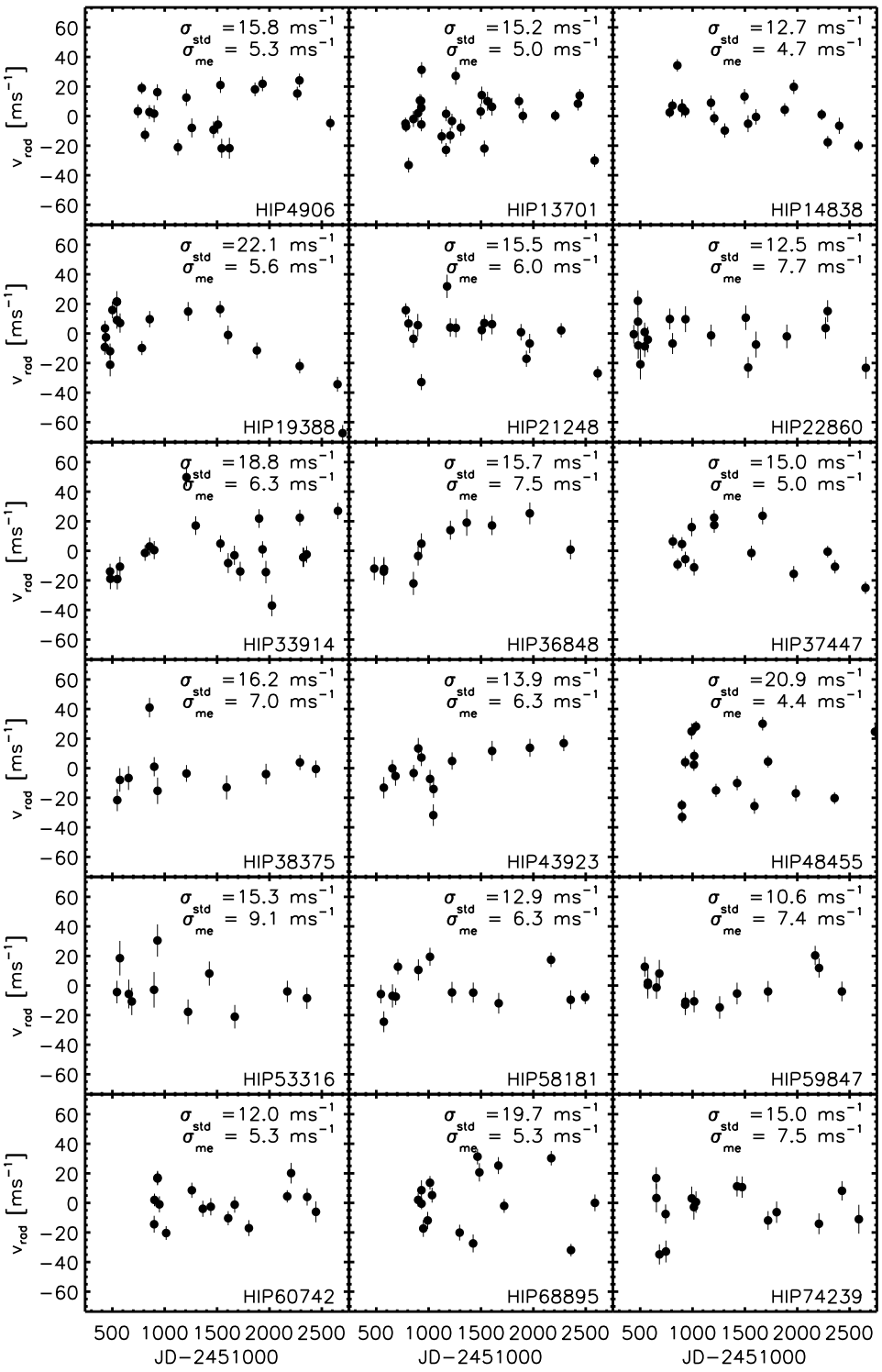

Figure 3.1: Radial velocity variations with an arbitrary zero point as a function of Julian Date for the first 21 stars. The numbers in the upper right corner of each frame are the observed standard deviation ($\sigma_{\rm std}$, upper number) and the mean error ($\sigma_{\rm me}$, lower number) of the radial velocity observations. The Hipparcos catalog number is plotted in the lower right corner of each frame.

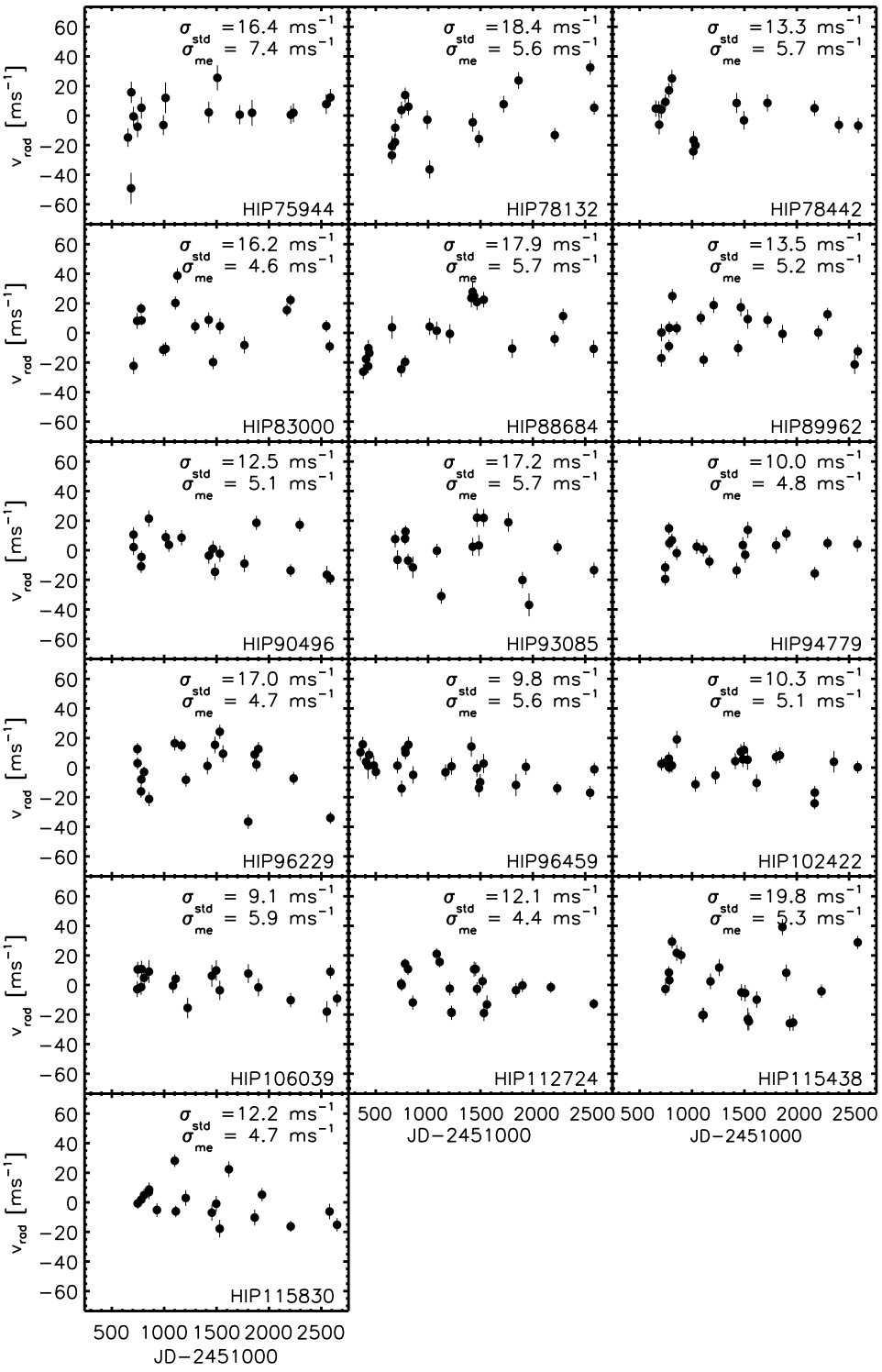

Figure 3.1: Continued.

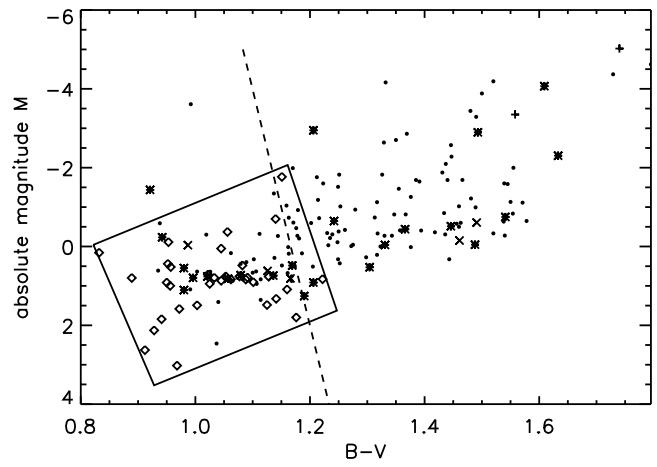

Figure 3.2: $M_{\rm V}$ vs. $B-V$ diagram with all 179 stars in the survey. The diamonds represent the stable stars, the asterisks represent the binaries, the crosses the variable stars with a long trend, the plus-signs are two supergiants with large, random radial velocity variations, and the dots are all other stars. The box is drawn around the stable stars and contains 11 binaries, 3 variable stars with a long trend, and 73 stars among which the 34 "stable" stars. The dashed line indicates the coronal dividing line (CDL) (Haisch 1999).

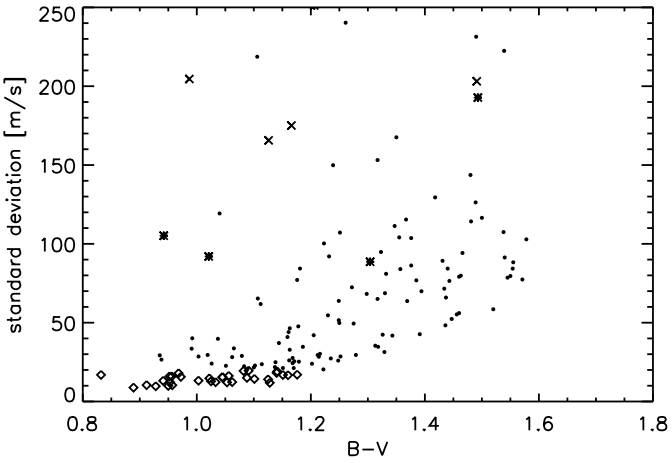

Figure 3.3: Standard deviation of the radial velocity of the stars from the survey plotted as a function of $B-V$. Most stars with $B-V<1.2$ show smaller variations in the radial velocity than the ones with $B-V>1.2$. The symbols are the same as in Figure 3.2. The stars with a standard deviation larger than 250 m s^{-1} are not shown.

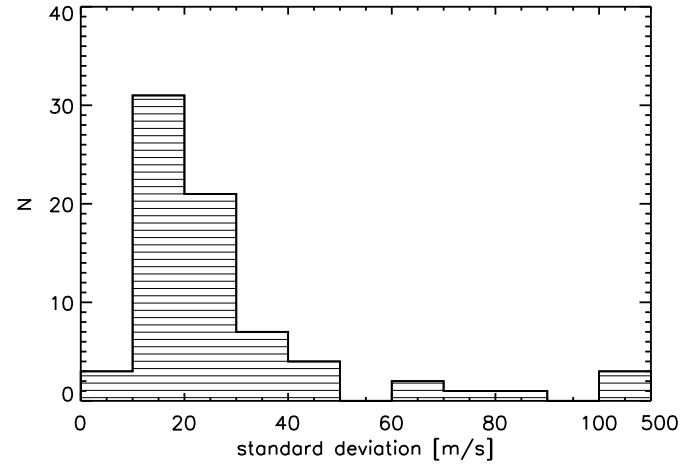

Figure 3.4: Histogram of the observed standard deviations (including the contribution of the radial velocity errors) for the stars in the box in the $M_{\rm V}$ vs. $B-V$ diagram from Figure 3.2. Binaries and the variable stars with a long trend are excluded. The stars in the highest bin have a standard deviation between 100 m s^{-1} and 500 m s^{-1}.

sample. They observed short time scale variations and interpreted these as p-mode pulsations. The radial velocity observations by Barban et al. (2004) have approximately the same amplitude as observed in the present survey. This indicates that the small radial velocity variations in the "stable" K giants are likely p-mode pulsations in the atmospheres of these stars. These pulsations are much more rapid than the typical time sampling of our observations, and thus appear as scatter in our data.

As the standard deviation is larger for all other stars in the sample (not considered in this paper), we can infer that essentially all K giants show radial velocity variations on the level of a few m s^{-1}. Furthermore since all stars with a standard deviation less than 20 m s^{-1} are found in the box in Figure 3.2 (by definition), which ranges roughly to $B - V = 1.2$, all stars redder than that show intrinsic variations larger than our threshold of 20 m s^{-1}.

3.4.3 Standard star sample

The stars presented in this paper can serve as an addition to the standard star sample presented by Udry et al. (1999a,b). Only one star (HIP19388 / HD26162) from the present survey is present in their sample. They obtained 252 observations for this star with a timespan of 6993 days and found a velocity dispersion of 0.3 km s^{-1}. This is the precision level of their observations and thus consistent with stability. The 12 stars from the present survey with a flag set to K in Table 3.2 are also present among the 3967 candidate standards listed in Table 2 of Kharchenko et al. (2004). These candidate standards are selected based on the following criteria: no multiplicity or variability flag, standard errors of equatorial coordinates $\sigma < 40$ mas, standard errors of proper motions $\sigma_{pm} < 4$ mas/yr, standard errors of V magnitude $\sigma_{m_V} < 0.05$ mag and $B-V$ colour $\sigma_{B-V} < 0.07$ mag, standard errors of radial velocity $\sigma_{RV} < 2$ km s^{-1}, and at least 4 radial velocity observations. The present observations could serve as a confirmation of their stability.

The stars for which the flag in Table 3.2 is set to N are stars which do not have enough radial velocity observations in Kharchenko et al. (2004) but do match all other criteria. The stars without a flag in Table 3.2 all have a photometric variability flag in the Tycho 1 catalog (ESA 1997), and are therefore not included in the Kharchenko et al. (2004) candidate standard star catalog. For details see the main catalog, Table 1 of the same publication. However, from the present observations no evidence for variability in the radial velocity larger than 20 m s^{-1} is found.

3.4.4 Reference stars

The results presented in this paper provide a refined answer to the question that originally motivated our radial velocity survey, namely whether K giants are suited as reference stars for the Space Interferometry Mission and other astrometric projects (see Frink et al. 2001, for details). K giants are in principle good reference stars because they are intrinsically bright. Therefore sub-stellar companions do not disturb their photocenters much, neither by contributing light to the system, nor through their gravitational influence. (Note that for a desired apparent magnitude intrinsically brighter stars can be selected at a large distance, so that the angular displacement due to companions remains small.) However, any sample of "anonymous" rather distant

K giants will contain a large fraction of binaries with stellar secondaries, which may lead to problems for astrometry. Our data demonstrate that binaries with a radial velocity amplitude of a few tens of $\mathrm{m\,s^{-1}}$ can be identified readily with only a small number of high precision spectroscopic observations, provided that the giants chosen are not too red or too luminous. This reinforces the conclusion already drawn by Frink et al. (2001) that K giants are indeed good astrometric reference stars, and validates the grid star strategy adopted by the SIM PlanetQuest project.

3.4.5 Sub-stellar companions and pulsations

The radial velocity variations on the level of a few $\mathrm{m\,s^{-1}}$ are interesting for oscillation studies. With the present observations we show that they are observable in data with a precision of a few $\mathrm{m\,s^{-1}}$. The time sampling of our observations is not suitable to obtain periods, but with campaigns taking multiple observations during each night this should be possible. Due to the fact that the oscillations appear on a level of a few $\mathrm{m\,s^{-1}}$ and with short periods it is also possible to search for (sub-stellar) companions around these stars which can have larger radial velocity variations on longer timescales.

ACKNOWLEDGEMENT

SH wants to thank Ignas Snellen for a careful reading of this manuscript and very useful suggestions. Furthermore, we would like to thank the entire staff at Lick Observatory for their untiring support.

REFERENCES

Allende Prieto, C. & Lambert, D. L. 1999, A&A, 352, 555

Barban, C., de Ridder, J., Mazumdar, A., et al. 2004, in ESA SP-559: SOHO 14 Helio- and Asteroseismology: Towards a Golden Future, 113

Barbier-Brossat, M. & Figon, P. 2000, A&AS, 142, 217

Butler, R. P., Marcy, G. W., Williams, E., et al. 1996, PASP, 108, 500

Duflot, M., Figon, P., & Meyssonnier, N. 1995, A&AS, 114, 269

ESA. 1997, VizieR Online Data Catalog, 1239

Evans, D. S. 1968, in Trans. IAU Vol XIII B, ed. L. Perek (Reidel, Dordrecht), 170

Famaey, B., Jorissen, A., Luri, X., et al. 2005, A&A, 430, 165

Frink, S., Mitchell, D. S., Quirrenbach, A., et al. 2002, ApJ, 576, 478

Frink, S., Quirrenbach, A., Fischer, D., Röser, S., & Schilbach, E. 2001, PASP, 113, 173

Haisch, B. M. 1999, in The many faces of the sun: a summary of the results from NASA's Solar Maximum Mission., 481

Hatzes, A. P. & Cochran, W. D. 1998, in ASP Conf. Ser. 154: Cool Stars, Stellar Systems, and the Sun, ed. R. A. Donahue & J. A. Bookbinder, 311

Heard, J. F. 1968, in Trans. IAU Vol XIII B, ed. L. Perek (Reidel, Dordrecht), 169

Hekker, S., Reffert, S., & Quirrenbach, A. 2006, Communications in Asteroseismology, 147, 121

Henry, G. W., Fekel, F. C., Henry, S. M., & Hall, D. S. 2000, ApJS, 130, 201

Kharchenko, N. V., Piskunov, A. E., & Scholz, R.-D. 2004, Astronomische Nachrichten, 325, 439

Larson, A. M., Yang, S. L. S., & Walker, G. A. H. 1999, in ASP Conf. Ser. 185: IAU Colloq. 170: Precise Stellar Radial Velocities, ed. J. B. Hearnshaw & C. D. Scarfe, 193

Linsky, J. L. & Haisch, B. M. 1979, ApJ, 229, L27

Marcy, G. W. & Butler, R. P. 2000, PASP, 112, 137

Nidever, D. L., Marcy, G. W., Butler, R. P., Fischer, D. A., & Vogt, S. S. 2002, ApJS, 141, 503

Pearce, J. A. 1955, in Trans. IAU Vol IX B, ed. P. Oosterhoff (Cambridge University Press, Cambridge), 441

Pepe, F., Bouchy, F., Queloz, D., & Mayor, M. 2003, in ASP Conf. Ser. 294: Scientific Frontiers in Research on Extrasolar Planets, 39

Queloz, D., Mayor, M., Udry, S., et al. 2001, The Messenger, 105, 1

Udry, S., Mayor, M., Maurice, E., et al. 1999a, in ASP Conf. Ser. 185: IAU Colloq. 170: Precise Stellar Radial Velocities, 383

Udry, S., Mayor, M., & Queloz, D. 1999b, in ASP Conf. Ser. 185: IAU Colloq. 170: Precise Stellar Radial Velocities, 367

CHAPTER 4

Precise radial velocities of giant stars. III. Variability mechanism derived from statistical properties and from line profile analysis

S. Hekker, I.A.G. Snellen, C. Aerts, A. Quirrenbach, S. Reffert, D.S. Mitchell

Astronomy & Astrophysics 2007, submitted

SINCE 1999 a radial velocity survey of about 180 K giants is ongoing at University of California Observatories / Lick Observatory. The measurements have an accuracy of 5 to 8 $\mathrm{m\,s^{-1}}$. A large fraction ($\sim$25%) of stars in this sample shows periodic radial velocity variations. The aim of this paper is to provide insight in the mechanism(s) causing radial velocity variations in K giant stars. A relation between the amplitude of the radial velocity variations and surface gravity is investigated, as well as a statistical comparison between possible sub-stellar companions orbiting K giants in this sample of 180 stars and the known sub-stellar companions orbiting F, G and K dwarfs. In addition to these statistics, a spectral line shape analysis and temperature measurements over time are performed for a sub-sample of K giants, with high resolution spectra obtained with SARG mounted on the TNG, La Palma, Spain. We find a correlation between the amplitude of the radial velocity variations and surface gravity, as suggested earlier by Hatzes & Cochran (1998). Furthermore, radial velocity variations interpreted as due to sub-stellar companions show different statistics for the orbital parameters of these companions orbiting K giant stars compared to those orbiting F, G and K dwarfs.

Significant spectral line shape variations are observed for a number of stars in the sub-sample observed with SARG, while some also show significant temperature variations. The radial velocity amplitude vs. $\log g$ correlation seems to indicate that a large fraction of the radial velocity variations observed in K giants are caused by mechanisms intrinsic to the stars. However, if the majority of the periodic radial velocity variations in K giants is interpreted as sub-stellar companions, then the orbital parameters would be considerably different from the ones observed for F, G and K dwarfs. It is likely that both phenomena, i.e. extrinsic and intrinsic motion, are at work simultaneously in several targets.

4.1 INTRODUCTION

For more than a decade, radial velocity observations with accuracies of order $\mathrm{m\,s^{-1}}$ have been within reach (see for instance Marcy & Butler (2000) and Queloz et al. (2001)). Even accuracies of less than 1 $\mathrm{m\,s^{-1}}$ (Pepe et al. 2003) are possible now. With these type of observations, more than 200 sub-stellar companions have been discovered by measuring the reflex motion of a star. Most of these sub-stellar companions have been detected around F, G and K main sequence stars, but detections around an A star (Galland et al. 2006) and several subgiants (Johnson et al. (2006), Johnson et al. (2007)) have also been reported recently. Moreover, 9 giant stars were reported to have sub-stellar companions (ι Draconis (K2III) Frink et al. (2002), HD104985 (G9III) Sato et al. (2003), HD47526 (K1III) Setiawan et al. (2003), HD13189 (K2II-III) Hatzes et al. (2005), HD11977 (G5III) Setiawan et al. (2005), Pollux (K0III) Hatzes et al. (2006), Reffert et al. (2006), 4UMa (K1III) Doellinger et al. (2007), and recently NGC2423 No3 and NGC4349 No127 Lovis & Mayor (2007))[1]. In addition to searches for extra solar companions, radial velocity observations prove to be very useful for detecting solar-like oscillations in stars with turbulent atmospheres, such as the dwarf α Cen A (e.g. Bedding et al. (2006)), the subgiant Procyon (e.g. Eggenberger et al. (2004) and Martić et al. (2004)) and the giant ϵ Ophiuchi (e.g. De Ridder et al. (2006)).

With techniques for accurate radial velocity observations at hand, a survey was started in 1999 to verify whether K giants are stable enough to be used as astrometric reference stars for SIM PlanetQuest (Space Interferometry Mission) (Frink et al. 2001). This survey contains 180 stars and uses the Coudé Auxiliary Telescope (CAT) at University of California Observatories / Lick Observatory, in conjunction with the Hamilton échelle spectrograph. The survey has recently been expanded to about 380 giants and is still ongoing.

From this survey, companions have been announced for ι Draconis (Frink et al. 2002) and Pollux (Reffert et al. 2006). Stars with radial velocity variations of less than 20 $\mathrm{m\,s^{-1}}$ have been presented as stable stars by Hekker et al. (2006b) (Chapter 3). In addition, some binaries discovered with this survey, as well as an extensive overview of the sample, will be presented in forthcoming papers. Apart from the stable stars and the binary systems, a large percentage of stars show either random or often periodic (sinusoidal) variations.

In this paper we investigate whether the periodic radial velocity variations, observed in $\sim 25\%$ of the stars in our sample, are in general caused by companions or by processes intrinsic to the star, such as pulsations or spots. In Section 2, the radial velocity observations are de-

[1]For updated information on sub-stellar companions, see http://exoplanet.eu and http://exoplanets.org.

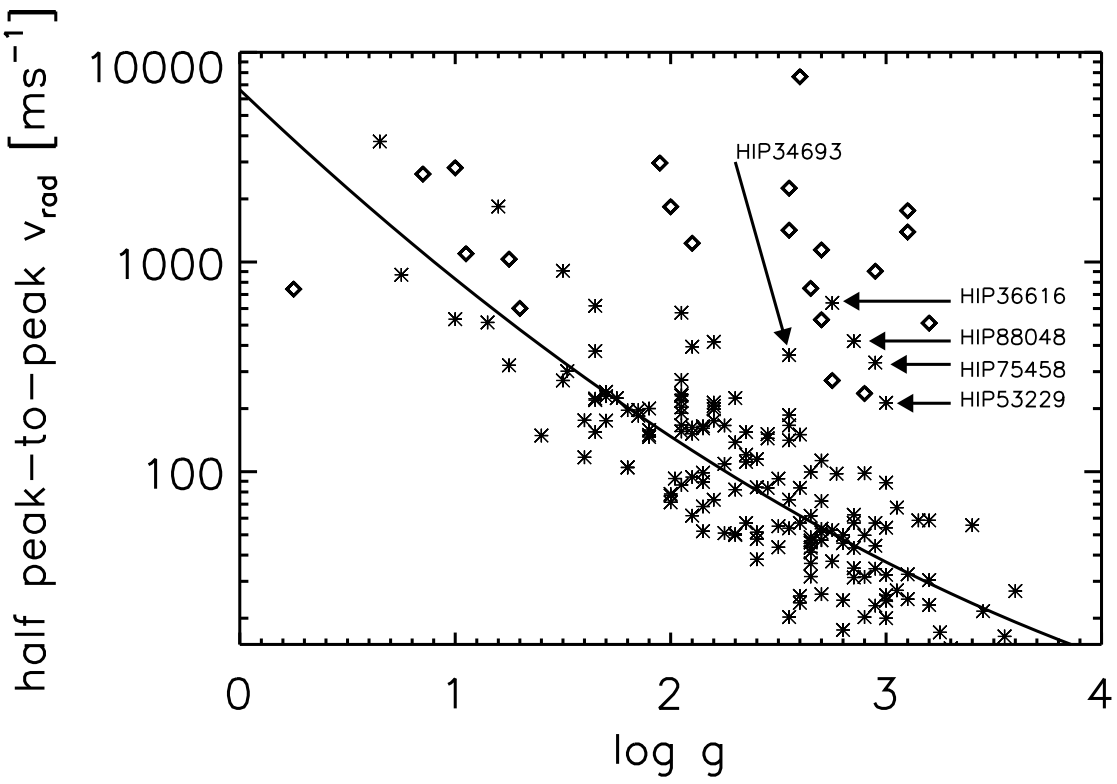

Figure 4.1: Half of the peak-to-peak variation of the radial velocity as a function of surface gravity ($\log g$). The single stars are indicated with an asterisk, while stellar binaries (companion mass > 100 M_{Jup}) are indicated with diamond symbols. Stars with a higher radial velocity amplitude than expected based on their $\log g$ value are indicated by arrows. The solid line is the best fit through the single stars.

scribed in detail. In Section 3, the relation between the observed radial velocity amplitude and surface gravity is investigated, while in Section 4 we assume that the radial velocity variations are caused by sub-stellar companions, and compare the inferred orbital parameters with those obtained for sub-stellar companions orbiting main sequence stars. In Section 5 line shape analysis is described together with results for stars observed with SARG, the high resolution échelle spectrograph mounted on the Telescopio Nazionale Galileo, La Palma, Spain. Our conclusions are presented in Section 6.

4.2 RADIAL VELOCITY OBSERVATIONS

For the radial velocity survey a sample of about 180 K giants has been selected from the Hipparcos catalog (Perryman & ESA 1997), based on the criteria described by Frink et al. (2001). The selected stars are all brighter than 6 mag, are presumably single and have photometric variations < 0.06 mag in V. The survey started in 1999 at Lick Observatory using the Coudé Auxiliary Telescope (CAT) in conjunction with the Hamilton échelle spectrograph (R=60 000). The system with an iodine cell in the light path has been developed as described by Marcy &

Butler (1992) and Valenti et al. (1995). With integration times of up to thirty minutes for the faintest stars ($m_{\rm V}$ = 6 mag) we reach a signal to noise ratio of about $80 - 100$ at $\lambda = 5500$ Å, yielding a radial velocity precision of $5 - 8$ m s^{-1}. As we are looking for radial velocity variations of order 10 to 100 m s^{-1}, this is adequate and hence no attempt has been made to reach the 3 m s^{-1} accuracy which is in principle possible with this setup (Butler et al. 1996). For the determination of the radial velocities the pipeline described by Butler et al. (1996) is used. In this pipeline, a template iodine spectrum and a template spectrum of the target star obtained without an iodine cell in the lightpath are used to model the stellar observations with a superposed iodine spectrum. The Doppler shift is a free parameter in this model. Note that, with this method the absolute radial velocity is not measured, but the radial velocity relative to the stellar template is obtained.

4.3 RADIAL VELOCITY AMPLITUDE - SURFACE GRAVITY RELATION

Hatzes & Cochran (1998) already investigated the origin of the observed radial velocities in K giant stars. Although their sample contained only 9 stars, they suggested that the amplitude of the radial velocity increases with decreasing surface gravity ($\log g$). In lower surface gravity it takes longer to decrease the velocity of a moving parcel which results in larger amplitudes and the relation suggested by Hatzes & Cochran (1998) would therefore be evidence for pulsations or rotational modulation as the mechanism for these long period radial velocity variations.

For the present sample, $\log g$ values are determined spectroscopically by imposing excitation and ionisation equilibrium of iron lines through stellar models. We estimate the error to be 0.22 dex from the scatter found in a comparison with literature values. A more detailed description and stellar parameters for individual stars is presented by Hekker & Meléndez (2007) (Chapter 5).

In Figure 4.1, we show half of the peak-to-peak value of the observed radial velocity variations as a function of $\log g$ for K giants in our sample. A clear trend is visible between increasing radial velocity variations, regardless of periodicity, and decreasing $\log g$, which provides a strong indication that, at least for a large fraction of stars in our sample, the observed radial velocity variations are induced by a mechanism intrinsic to the star. Five stars have a higher radial velocity amplitude than expected based on their $\log g$ value and are indicated with arrows in Figure 4.1. The radial velocity variation observed for HIP53229 may be due to a stellar companion in a wide orbit, with a period much longer than the observation time span. Due to this long period the companion mass, and, therefore, the (sub-)stellar nature, is still very uncertain. The observed radial velocity variations for HIP36616 and HIP88048 can be fitted very accurately with two Keplerian orbits, while HIP75458 can be explained by an eccentric sub-stellar companion (Frink et al. 2002) and an additional linear trend, indicating a companion in a wide orbit. HIP34693 can be fitted very accurately with a Keplerian orbit of a single nearly sinusoidal sub-stellar companion. The latter 3 stars are investigated more extensively, in Section 5.

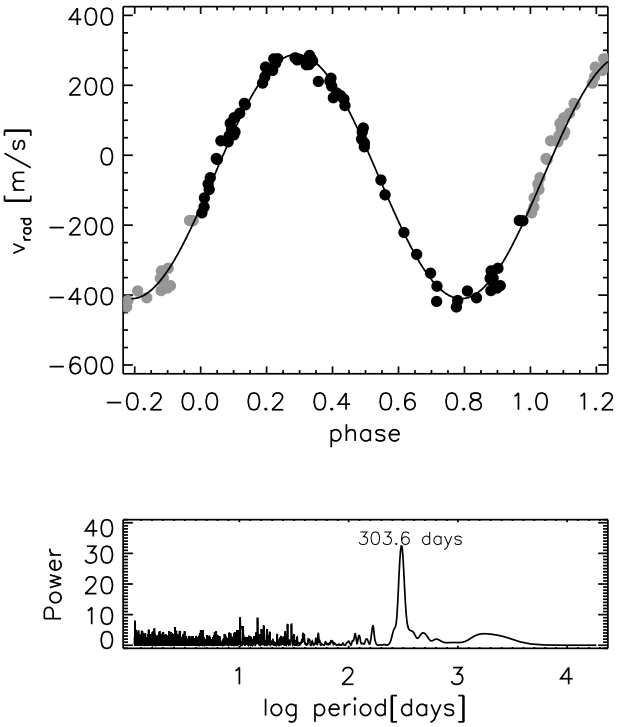

Figure 4.2: Radial velocity variations as a function of phase for a star with a highly significant period (top), with its periodogram (bottom).

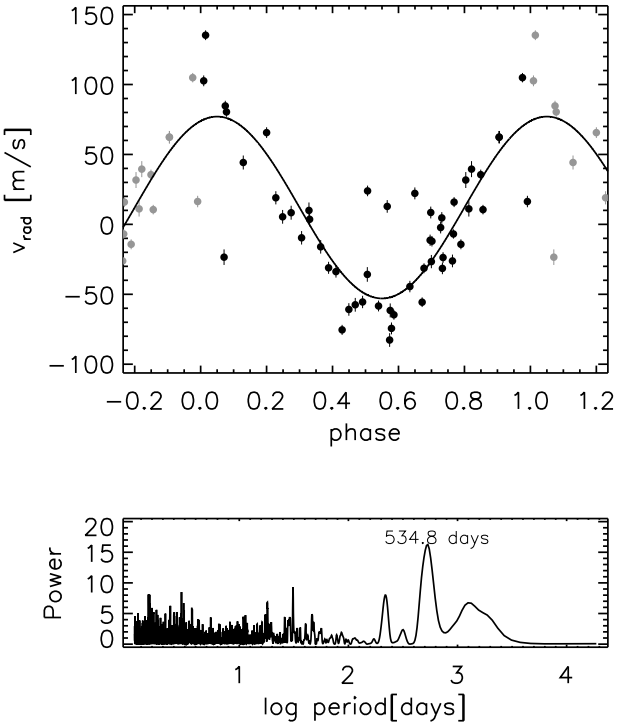

Figure 4.3: Radial velocity variations as a function of phase for a star with a a period close to the significance threshold (top), with its periodogram (bottom).

4.4 COMPANION INTERPRETATION

Although the above analysis supports the interpretation that the observed radial velocity variations are likely caused by mechanisms intrinsic to the star, we assume here the alternative possibility that the periodic radial velocity variations in K giant stars are caused by sub-stellar companions. We investigate the statistical properties of the orbital parameters of the sample and compare these with the statistical properties of companions orbiting F, G and K dwarfs.

For the analysis of the radial velocity variations we used the software package developed by Laughlin (see http://www.oklo.org), based on the analyses used in Laughlin & Chambers (2001). For radial velocity variations with a significant periodicity, we calculated orbital parameters for an inferred companion. Periods with a false alarm probability (FAP) $< 10^{-3}$, as provided by the software package, are considered significant. This is comparable with a 6σ significance determined from the average power of the residual Scargle periodogram (Scargle 1982) with frequencies between 0 and 0.03 cycles per day (c d^{-1}) (0.35 μHz) and a frequency step of 0.00001 c d^{-1} ($0.12 \cdot 10^{-3}$ μHz) (Kuschnig et al. 1997). In Figures 4.2 and 4.3 the radial velocity variation as a function of phase is shown for two stars. The period of the star in Figure 4.2 is highly significant, while the one in Figure 4.3 is close to the significance threshold. Periodograms are shown in the bottom panels of these figures.

According to our analysis, 51 stars in the sample would have a single companion, and 13 stars multiple companions. Twenty-two (21 single and 1 in a multiple system) of these companions have $m \sin i$ larger than 100 $M_{\rm Jup}$ and should be interpreted as stellar binaries. By advancing the multiple sub-stellar systems forward in time via a Runga-Kutta integration, we investigated the stability of the systems, taking into account the mutual interactions of the companions. We found that 10 of the 12 inferred sub-stellar multiple systems would be 'likely unstable', with a change in semi-major axis $> 1\%$ and $< 10\%$, or 'unstable' with a change in semi-major axis $> 10\%$ on a time scale of 100 years due to companion-companion interaction.

The stability depends, e.g., on the starting epoch of the computations, as well as on the orbital parameters, which might change with an increasing number of observations. Furthermore, there is no guarantee that the obtained χ^2 minimum is a global minimum. Therefore, stars with multiple inferred sub-stellar companions that seem to be unstable, might also have stable solutions. One could also use the equations for dynamical stability described by Gladman (1993) and Marcy et al. (2001). Gladman (1993) also notes that the Hill stability criteria for companions in initially eccentric orbits may not be met, but that the systems may still be found to be empirically quite stable for a long period of time. In order to draw a firm conclusion on the stability of a particular system, a more thorough investigation is needed, as well as data with a longer time base, which is beyond the scope of this paper.

For all stars with periodic radial velocity variations, we checked the Hipparcos (Perryman & ESA 1997) photometry. We checked periodograms for significant frequencies close to the obtained radial velocity period, and plotted the photometric values phased with the radial velocity period. None of the stars show photometric variations related to the observed radial velocity variations.

The mass distribution of our K giant sample is largely unknown. The stellar masses are typically between 1 and 4 $M_\odot$. Hence most of their main sequence progenitors should have been of A or F spectral class. The distribution of orbital parameters of sub-stellar companions orbiting A and F main sequence stars is still unknown. The orbital distribution may be similar

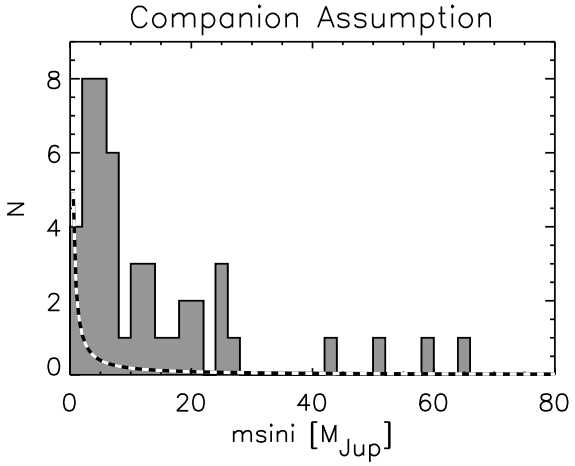

Figure 4.4: A histogram of $m \sin i$ of inferred companion masses orbiting K giants in our sample. The dashed line indicates the rise of planet masses $M^{-1.05}$ from 10 $M_{\rm Jup}$ down to Saturn masses for sub-stellar companions around main sequence stars (Marcy et al. 2005), normalised to the number of stars in our sample.

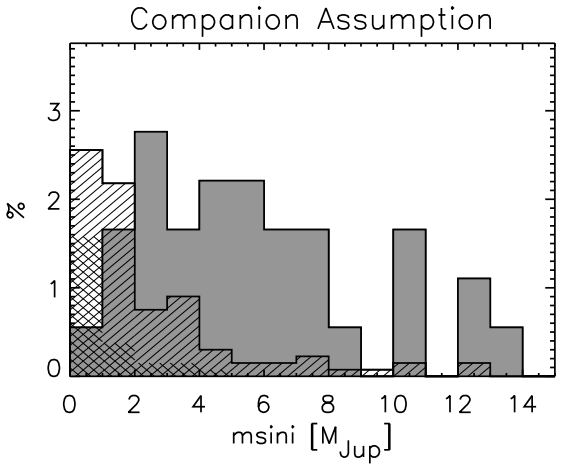

Figure 4.5: Zoom in on the low end of the companion mass distribution of inferred sub-stellar companions orbiting K giant stars in our survey, shown as percentage of the total number of stars in the sample (filled histogram). The hatched histogram shows the distribution of companion masses orbiting main sequence stars as shown in Figure 1 of Marcy et al. (2005), as a percentage of the total number of stars in their sample. The cross hatched area are main sequence stars with companions at a semi-major axis smaller than 0.3 AU (see Figure 4.6).

to the orbital distributions for F, G and K dwarfs, but changes with stellar mass are possible. Also, the evolution of these stars may have influence on the orbital parameter distribution of the companions orbiting the K giants.

Since the data presented here span ~ 2500 days, radial velocity variations with longer periods are uncertain, and, therefore, not taken into consideration. Companions with periods exceeding the observation time span are also excluded from the F, G, and K main sequence star statistics.

4.4.1 Mass distribution

Figure 4.4 shows the distribution of inferred companion masses of our K giant sample. First, notice that 30% of the inferred companions would have masses in the brown dwarf regime 15 $M_{\rm Jup} < m \sin i < 80$ $M_{\rm Jup}$. This is in sharp contrast to the brown dwarf statistics around F,

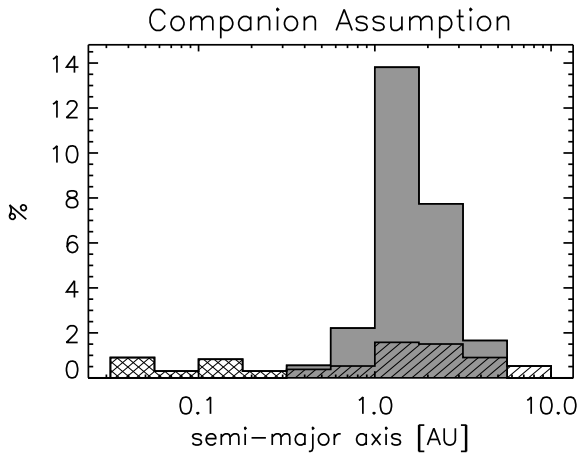

Figure 4.6: Semi-major axis distribution of inferred K giant companions in our sample (filled histogram), shown as a percentage of the total number of stars in the sample. The hatched histogram shows the distribution for F, G and K main sequence stars as shown in Figure 2 of Marcy et al. (2005), as a percentage of the total number of stars in their sample. The main sequence stars with a companion orbiting at a semi-major axis smaller than 0.3 AU are cross-hatched. These are also indicated in Figures 4.5 and 4.7.

G and K main sequence stars for which only very few companions are found with $m \sin i > 15$ M_{Jup} around more than thousand stars. This is known as the brown dwarf desert and is possibly caused by migration and merging of brown dwarfs in a viscous disk with a mass at least comparable to the brown dwarf mass (Armitage & Bonnell 2002).

The dashed line in Figure 4.4 indicates the rise of sub-stellar companion masses $M^{-1.05}$ from 10 M_{Jup} down to Saturn masses for main sequence stars (Marcy et al. 2005), normalised to the number of stars in our sample. We use a two-sided Kolmogorov-Smirnov test (Press et al. 1992) (hereafter KS-test) to compare the $M^{-1.05}$ fit and the mass distribution ($m \sin i < 80$ M_{Jup}) of our sample and find a probability of 0.05% (0.002% for $m \sin i < 28$ M_{Jup}) that these are identical. This reveals that inferred sub-stellar companions around K giants in our sample have higher masses compared to companions around F, G and K main sequence stars.

Figure 4.5 shows the low mass companion distribution of our survey. This reveals that most K giant companions would have inferred masses between 2 and 8 M_{Jup}, while the fraction of companions orbiting F, G and K dwarfs strongly decreases with increasing $m \sin i$.

4.4.2 Semi-major axis distribution

The distribution of the companion's semi-major axis is shown in Figure 4.6. No inferred companions with semi-major axis smaller than 0.3 AU are present in the K giant sample, possibly due to increased stellar radii of giants. The fraction of stars with an inferred companion with a semi-major axis between 1 and 3 AU is much higher among the K giants compared to the F, G and K dwarfs. A comparison between the two distributions with a KS-test reveals a probability for the 2 distributions to be identical of 11%. This increases to 32%, when omitting the main sequence stars with semi-major axis < 0.3 AU. The increasing incompleteness beyond 3 AU, due to the limited time span of surveys, is present in both samples as the surveys span a comparable amount of time. This incompleteness can not cause the significant difference in the peak between 1 and 3 AU.

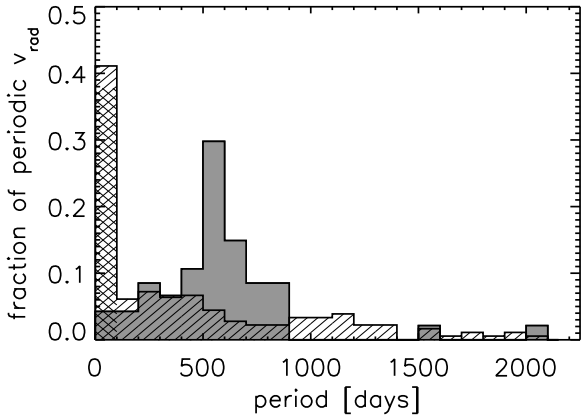

Figure 4.7: Period distribution of the observed radial velocity variations shown as a fraction of all significant periods (filled histogram). The period distribution of main sequence stars (Butler et al. 2006) is shown in the hatched histogram, as a fraction of the total number of observed companions. The cross hatched area are main sequence stars with a semi-major axis smaller than 0.3 AU (see Figure 4.6).

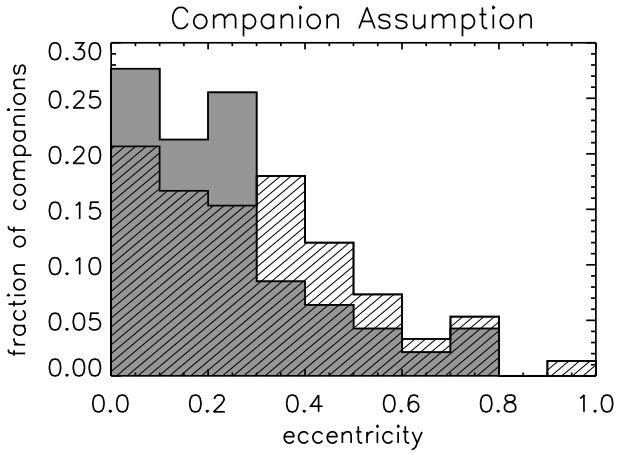

Figure 4.8: Distribution of eccentricities for possible companions around K giants in our sample (filled histogram) shown as a fraction of all possible sub-stellar companions in the sample. The hatched histogram is the eccentricity distribution of companions around main sequence stars (Butler et al. 2006) shown as a fraction of all companions around main sequence stars. Companions with periods shorter than 20 days are excluded from the latter sample as these might be tidally circularised.

4.4.3 Period distribution

In Figure 4.7 the period distribution of the observed radial velocity variation is shown and compared with the companion period distribution of dwarfs. The large fraction of F, G and K dwarf companions with orbital periods shorter than 100 days corresponds to the ones with semi-major axis smaller than approximately 0.3 AU. The close-in short period companions are not present around K giants, while about 80% of these stars with observed radial velocities have periods ranging between 400 and 800 days. A KS-test reveals a probability of less than 0.0001% for the 2 distributions to be identical. The probability remains below this level, when omitting the companions orbiting main sequence stars with a semi-major axis < 0.3 AU.

4.4.4 Eccentricity distribution

Figure 4.8 shows the distribution of companion eccentricities for K giants in our sample and for dwarfs. Companions of dwarfs with periods less than 20 days are excluded, as these might be

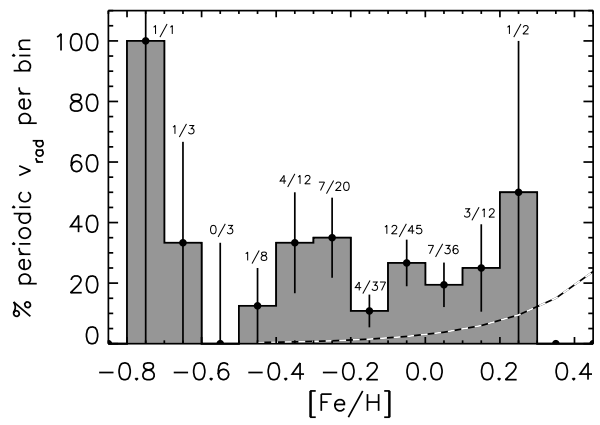

Figure 4.9: Iron abundance [Fe/H] distribution of K giant stars with periodic radial velocity variations shown as a percentage of the total number of observed stars with iron abundance in the same interval. The numbers above each bar on the histogram indicate the ratio of stars with a significant periodic radial velocity variation to the total number of stars in each bin. The error bars are calculated assuming Poisson statistics (i.e. the percentage of stars with periodic radial velocities divided by the square root of the number of stars with periodic radial velocities). The dashed line is the power law derived for the increasing trend in the fraction of stars with companions as a function of metallicity of F, G and K main sequence stars (Fischer & Valenti 2005).

tidally circularised.

The fraction of companion eccentricities < 0.3 for the giants is 75% compared to 50% for companions orbiting F, G and K dwarfs. The KS-test shows that these distributions are nearly identical (97%).

4.4.5 Iron abundance

Companion occurrence correlates strongly with the abundance of heavy elements (see for instance Gonzalez (1997), Fischer & Valenti (2005) and Santos et al. (2005)), such that F, G, and K dwarf stars with supersolar abundance are more likely to harbour sub-stellar companions (about 50% of the stars with $0.3 <$ [Fe/H] < 0.5). The increase of the fraction of F, G and K dwarfs harbouring companions with increasing metallicity is well fitted with a power law, yielding a probability for such a star to harbour a companion to be: P = 0.03·$[(N_{\rm Fe}/N_{\rm H})/(N_{\rm Fe}/N_{\rm H})_{\odot}]^{2.0}$ (Fischer & Valenti 2005).

In Figure 4.9 the iron abundance distribution of stars with periodic radial velocity variations is shown as a percentage of the total number of observed stars with iron abundance in the same interval. The iron abundance is determined spectroscopically by imposing excitation and ionisation equilibrium in iron lines and is described in Hekker & Meléndez (2007) (Chapter 5). The maximum iron abundance of a K giant star in our sample is 0.29 and, therefore, we do not probe the high metallicity region in which F, G and K dwarfs are most likely to harbour a companion.

The mean metallicity of the K giants in the entire sample is -0.12 dex, while the mean metallicity of the stars with periodic radial velocity variations, presented in Figure 4.9, is -0.13

dex. This means that the metallicities of stars with inferred companions are similar to the mean metallicity of the total sample. Fischer & Valenti (2005) find that companion parent stars are more metal rich by 0.13 dex relative to their overall dwarf sample. This metallicity enhancement is also valid for giants with announced companions, see Hekker & Meléndez (2007) (Chapter 5).

4.4.6 Summary companion interpretation

Based on the statistics shown in this section, where we assumed that the radial velocity variations in K giants are caused by sub-stellar companions, we conclude that, if the majority of the observed radial velocity variations are due to sub-stellar companions, the orbital parameters of these companions orbiting K giants are considerably different from those orbiting F, G and K dwarfs. The 25% fraction of K giants that would harbour a sub-stellar companion with $m \sin i > 1$ $M_{\rm Jup}$ is extremely high compared to the approximately 5% of the 1330 F, G and K main sequence stars investigated by Marcy et al. (2005). This would be consistent with the analysis presented by Lovis & Mayor (2007), who also find a high frequency of massive sub-stellar companions around intermediate mass stars. Furthermore, they show that more massive stars form more massive planetary systems than lower mass stars. Note that they exclude pulsations based on bisector analysis, but as shown by both Dall et al. (2006) and Hekker et al. (2006a) (Chapter 2), the line bisector is not a suitable diagnostic to characterise stellar oscillations.

The formation of sub-stellar companions orbiting different stellar masses is investigated theoretically, by i.e. Laughlin et al. (2004) and Ida & Lin (2005), using the core accretion model. These investigations emphasise more the lower mass dwarfs ($M<M_{\odot}$), as radial velocity observations are ongoing at large scales for these stars. The theoretical investigations show that lower mass stars are more likely to have lower mass sub-stellar companions, e.g. Neptune mass companions are more likely to orbit M dwarfs, while Jupiter mass companions are more likely to orbit F, G and K dwarfs. These results seem to indicate that higher mass stars would have higher mass companions, consistent with our finding.

The mean metallicity of companion hosting stars would be similar to the mean metallicity of the total sample, which would be different from F, G and K dwarfs, where companion hosting stars are more metal-rich than a total sample of dwarfs (Fischer & Valenti 2005). Also, this metallicity enhancement seems to be present for giants with announced companions (Hekker & Meléndez 2007) (Chapter 5).

4.5 LINE SHAPE ANALYSIS

The analyses described in the previous sections indicate that the observed radial velocity variations may be induced by processes intrinsic to the star. To investigate the behaviour of individual stars, a spectral line shape analysis is performed for a sub-sample of stars. Line shape variations indicate a mechanism intrinsic to the star, while no line variations, but only line shifts, could indicate the presence of a companion.

Measuring line profile changes over time can be done on single line profiles or on cross-correlation profiles. The Fe I line at 6252.57 Å is explored as the best unblended sensitive line

suitable for line shape analysis (see for instance Gray (2005) and Dall et al. (2006)). Dall et al. (2006) investigated other spectral lines and cross-correlation profiles for line shape analysis. They concluded that a cross-correlation is useful for line shape analysis, provided that lines formed at approximately the same depth in the star are taken into account. However, they could not find any other single spectral line suitable for line shape analysis.

Some of the most commonly used diagnostics for line shape analysis are a line bisector and moments. A line bisector is a measure of the displacement of the centre of the red and blue wing from the core of the spectral line at each residual flux. A line bisector is often characterised by the bisector velocity span, which is defined as the horizontal distance between the bisector positions at fractional flux levels in the top and bottom part of the spectral line, see for instance Brown et al. (1998). Variations in the bisector velocity span indicate line shape variations, but as shown by both Dall et al. (2006) and Hekker et al. (2006a) (Chapter 2), the line bisector is not a suitable diagnostic to characterise stellar oscillations.

A line profile can also be described by its moments (Aerts et al. 1992). The first moment $\langle \mathrm{v} \rangle$ represents the centroid velocity of the line profile, the second moment $\langle \mathrm{v}^2 \rangle$ the width of the line profile and the third moment $\langle \mathrm{v}^3 \rangle$ the skewness of the line profile. The moments are fully described in terms of pulsation theory (Aerts et al. (1992), Aerts (1996), Briquet & Aerts (2003)). Pulsation modes can be identified from the moments in case the pulsation phase is well covered and the amplitude of the pulsation is larger than about half the equivalent width of the spectral line (Hekker et al. 2006a) (Chapter 2), which is not the case for the stars in this paper.

Apart from the more quantitative line shape diagnostics described above, some qualitative diagnostics can also be used to identify whether the line shape is changing. Plotting the residual of each line profile with respect to a time averaged profile can show variations in depth. These depth variations accompany radial velocity variations in case of pulsations or spots. Examples of the diagnostics described here for pulsations, companions and spots are further discussed and illustrated in Chapter 1.7.5. It is notably that Lovis & Mayor (2007) excluded pulsations from a line bisector analysis, but as shown by both Dall et al. (2006) and Hekker et al. (2006a) (Chapter 2), the line bisector is not a suitable diagnostic to characterise stellar oscillations. Therefore, we have chosen to consider other diagnostics that are more sensitive to oscillations.

4.5.1 Lick data

In order to investigate a correlation between the radial velocity variations and possible line shape variations, it would be ideal to use the observations obtained at Lick Observatory for line shape analysis. However, data of this signal to noise ratio and resolution, contaminated with iodine lines and without an accurate wavelength calibration do not allow a line shape analysis with the required accuracy.

In order to investigate spectral line shapes, observations without iodine contamination are performed for a sub-sample of stars with the SARG spectrograph mounted on the Telescopio Nazionale Galileo (TNG) at La Palma, Spain. For the SARG observations mainly stars with (nearly) sinusoidal radial velocity variations were selected, but also some with random variations and ι Draconis (Frink et al. 2002) and Pollux (Reffert et al. 2006) with announced sub-stellar companions.

4.5.2 SARG data

For 47 stars of the initial sample observed at Lick observatory, observations are performed with the high resolution spectrograph SARG. A 0”27x5”3 slit is used for a resolution of 164 000. Furthermore the ’yellow’ cross-disperser is used which has a wavelength range of 462 - 792 nm spread over 54 orders. Each run lasted only one (half) night and we have data of 10 runs over the period November 2003 until May 2006. 42 stars with 3 or more observation epochs are taken into account in the present analysis.

The raw spectra were bias corrected and flat fielded with the calibration images taken prior to the stellar observations. For the calibrated images we extracted and normalised each order. Thorium-Argon images (usually 2, also taken prior to the stellar observations) are used for wavelength calibration. Unfortunately, the spectrograph is not stabilised and, therefore, the wavelength calibration is not accurate at $\mathrm{m\,s^{-1}}$ level. This makes it impossible to obtain the radial velocity variations of the star with $\mathrm{m\,s^{-1}}$ accuracy, but, because of the high resolution and high signal to noise ratio of about 200, the line shapes of single spectral lines can be analysed.

Because the spectra are shifted due to an inaccurate wavelength calibration (inaccuracies of a few hundred $\mathrm{m\,s^{-1}}$), we calculated the first moments of the Fe I line at 6252.57 Å for each star at every epoch and shifted these lines to their laboratory wavelength. As we have a scarce time coverage, a quantitative measurement of the line shape variations is difficult. Therefore, a qualititative measurement is performed, i.e. for each star the residual of a single spectral line from a time averaged profile is calculated. With this measure we are able to see whether the lines change in depth and thus in shape. For the companion interpretation, we do not expect any shape variations (see Chapter 1.7.5 for some examples). The variance of the residual line is obtained from the line residuals in the V I line at 6251.83 Å. At each pixel, the variance of the residual of both spectral lines is calculated. The maximum variance is used as an estimate for the error in the residual Fe I profile.

The point spread function (PSF) variation from one observation to another can influence the spectral line depth variations to a large extent. Therefore, we investigated the extreme values of the line depth variation per night, i.e. we looked whether maximum (minimum) values of the residuals for all stars observed in one night were systematically higher or lower than the ones observed during other nights. No trends were visible. Furthermore, some of our stars do not show line depth variations exceeding the noise. The lack of nightly correlations and non-detections of the line depth variations show that line depth ratios are not largely influenced by the PSF, and can therefore be a valuable diagnostic for qualitative spectral line shape analysis.

In addition to the PSF, the continuum calibration might have influence on the spectral line depth variations. Therefore, this is considered very carefully. A local continuum calibration around the Fe I line is performed and each spectrum is checked by visual inspection.

For radial oscillation modes of considerable amplitude, one would expect to see photometric and / or temperature variations. The observations of Hipparcos (Perryman & ESA 1997) are used to search for photometric variations, while a line depth ratio of the V I line at 6251.83 Å to the Fe I line at 6252.57 Å is used to evaluate temperature variations. These lines are close together, minimising continuum errors, have similar strengths in K giants and are sensitive in the K giant temperature range (Gray (2005), Gray & Brown (2001)). As described by Gray & Brown (2001) and Biazzo et al. (2007), a line depth ratio is also sensitive to magnetic fields, metallicity, rotational velocity and luminosity of a star. These complicated dependencies are

Table 4.1: Line shape parameters for stars observed three or more times with SARG. Star name, half of the peak-to-peak value of the radial velocity variation (Δv_{rad}), in $m\,s^{-1}$, average temperature (<T>) determined from the line depth ratios, temperature range (ΔT) observed over time per star with its error (err_ΔT), all in [K], and the maximum variation in spectral line depth (Δresidual) with errors in the residuals (err_residual), both in continuum units.

star		Δv_{rad} $m\,s^{-1}$	<T> K	ΔT K	err_ΔT K	Δresidual continuum units	err_residual continuum units
HIP3179	HD3712	50.5	4806	5	12	0.035	0.023
HIP3419	HD4128	67.4	4874	17	12	0.028	0.021
HIP5364	HD6805	98.2	4525	14	13	0.049	0.013
HIP7884	HD10380	205.7	4307	13	14	0.054	0.025
HIP13905	HD18449	61.6	4478	17	14	0.032	0.016
HIP19011	HD25723	72.4	4760	12	12	0.033	0.019
HIP23015	HD31398	514.9	4337	17	14	0.038	0.017
HIP23123	HD31767	148.8	4498	17	14	0.030	0.015
HIP30720	HD45433	184.9	4339	22	14	0.031	0.022
HIP31700	HD47442	49.9	4700	21	13	0.027	0.012
HIP33160	HD50778	272.2	4225	35	15	0.030	0.017
HIP34693	HD54719	359.7	4443	17	14	0.046	0.021
HIP36616	HD59686	138.5	4617	5	13	0.030	0.017
HIP37826	HD62509	58.9	4824	13	12	0.038	0.026
HIP38253	HD63752	533.8	4489	15	14	0.036	0.012
HIP39177	HD65759	273.7	4470	27	14	0.038	0.010
HIP40526	HD69267	234.3	4266	22	15	0.045	0.025
HIP46390	HD81797	164.7	4303	18	14	0.031	0.013
HIP47959	HD84561	230.1	4240	10	15	0.045	0.016
HIP53261	HD94247	224.3	4355	29	14	0.039	0.012
HIP54539	HD96833	73.5	4630	23	13	0.047	0.011
HIP69673	HD124897	375.9	4458	9	14	0.037	0.010
HIP73133	HD131918	168.4	4290	10	14	0.035	0.019
HIP73620	HD133165	47.1	4802	10	12	0.051	0.018
HIP74732	HD135534	166.1	4337	21	14	0.033	0.014
HIP75458	HD137759	317.6	4477	19	14	0.049	0.016
HIP79540	HD145897	144.2	4373	10	14	0.034	0.016
HIP80693	HD148513	132.6	4227	35	15	0.042	0.015
HIP83254	HD153834	175.1	4573	18	13	0.022	0.015
HIP84671	HD156681	394.2	4241	7	15	0.036	0.014
HIP85355	HD157999	301.4	4464	18	14	0.427	0.207
HIP85693	HD158899	166.2	4288	7	14	0.041	0.028
HIP87808	HD163770	321.4	4639	11	13	0.037	0.023
HIP87933	HD163993	58.6	4972	16	11	0.038	0.014
HIP88048	HD163917	304.3	4872	11	11	0.034	0.020
HIP88636	HD165683	56.9	4641	13	13	0.021	0.008
HIP89826	HD168775	43.6	4575	17	13	0.026	0.010

Table 4.1: Continued.

star		Δv_{rad} $m\,s^{-1}$	<T> K	ΔT K	err_ΔT K	Δresidual continuum units	err_residual continuum units
HIP107315	HD206778	1032.5	4507	46	14	0.043	0.013
HIP109068	HD209747	146.3	4201	24	15	0.034	0.026
HIP113562	HD217303	908.2	4651	13	13	0.035	0.010
HIP114855	HD219449	113.0	4690	16	13	0.045	0.017
HIP117567	HD223559	1838.9	4208	30	15	0.037	0.018

indeed important to obtain an accurate temperature, but need not be taken into account for our purpose, which is only to detect the occurrence of temperature variations.

The line depths used for the temperature measurements are determined by fitting a second order polynomial through the 11 points with lowest flux value in the core of the line. The minimum flux value of this fit is taken as the line depth. Errors in the line depth are calculated from the signal to noise value (200 in the continuum) and combined in the standard manner to get the error in the ratio. For the conversion from line depth ratio to temperature, the coefficients for unbroadened giant stars from Biazzo et al. (2007) are used.

4.5.3 Results

In this section we present the results obtained from the line shape analysis performed with SARG as described in the previous subsection. In Table 4.1, the results for all stars with three or more observations with SARG are listed. To illustrate the results in Table 4.1, we, first of all, show examples of stars for which non-periodic radial velocity variations are observed (HIP54539 and HIP3179). We continue with examples of stars with periodic radial velocity variations, which can be fit with a Keplerian orbit. The radial velocity variations of these examples are shown in the left panels of Figures 4.10 - 4.11 as a function of Julian Date and in Figures 4.12 - 4.15 as a function of phase. In Figure 4.13 the longest period is removed for this phase plot, and in Figure 4.15 the observed linear trend is omitted. For periodic radial velocity variations, Keplerian orbits (two in case of multiple systems) are fit through the radial velocity variations and, in those cases, the residuals between the fit and the observations are plotted in the bottom left panel of these figures. The top right part of Figures 4.10 - 4.15 shows temperature variations obtained for each observation from the line ratio of V I at 6251.83 Å and Fe I at 6252.57 Å as a function of Julian Date in Figures 4.10 and 4.11, and as a function of phase in Figures 4.12 - 4.15. The phase is derived from the period obtained from the radial velocity variations. In case multiple periods are present in the radial velocities, the shortest period, which is always the most significant one, is used to determine the phase. The lower right panel of Figures 4.10 - 4.15 shows the residuals of the Fe I line at 6252.57 Å, taken at different epochs (indicated with different line styles), with respect to a time averaged profile as a function of wavelength. The vertical lines in this panel indicate the extent of the spectral line in wavelength. An error estimate, for the residual flux, is indicated with the thick error bar in the continuum on the left side of the spectral line. Stellar parameters for each star are shown in Tables 4.2 - 4.7. Orbital parameters will be presented in a forthcoming paper.

star	
spectral type[a]	K1III
$m_{\rm V}{}^a$ [mag]	3.00
$B-V^a$	1.144 ± 0.004
π^a [mas]	22.21 ± 0.68
distance [pc]	45.0 ± 1.4
$M_{\rm V}$ [mag]	-0.27 ± 0.07
mass[b] [$M_\odot$]	1.8
temperature[c] [K]	4655
$\log g^c$	2.55
Fe/H[c]	7.35
$v \sin i^c$ [km s^{-1}]	3.4
number of observations (Lick)	33
observed dispersion [m s^{-1}]	37.1

Table 4.2: Stellar parameters of HIP54539.

[a]Perryman & ESA (1997), [b] Allende Prieto & Lambert (1999), [c] Hekker & Meléndez (2007) (Chapter 5)

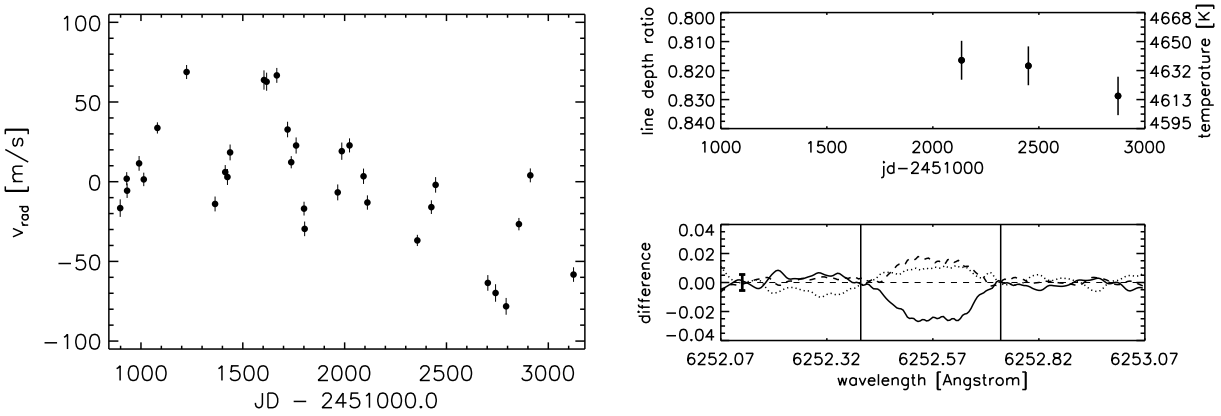

Figure 4.10: Left: radial velocity variations of HIP54539 as a function of Julian Date. No significant periodicity is found in these data. Right: The top panel shows the temperatures obtained for each observation from the line ratio of V I at 6251.83 Å and Fe I at 6252.57 Å as a function of Julian Date. The lower panel shows the residual of the Fe I line at 6252.57 Å, taken at different epochs (indicated with different line styles), with respect to a time averaged profile, as a function of wavelength. The vertical lines in this panel indicate the spectral line in wavelength. An error estimate is indicated with the thick error bar on the left side of the spectral line.

Examples of stars with non-periodic radial velocity variations

HIP54539 is a nearby K1 giant just outside the stable star box in the $M_{\rm V}$ vs. $B-V$ diagram indicated by Hekker et al. (2006b) (Chapter 3). Stellar parameters are listed in Table 4.2. The observed dispersion of 37 m s^{-1} is almost twice that adopted for stable stars (20 m s^{-1}). The observed radial velocity variations are plotted in Figure 4.10. No periodicity $<$ 2500 days was

star	
spectral type[a]	K0II-IIIvar
$m_{\rm V}{}^a$ [mag]	2.24
$B-V^a$	1.170 ± 0.000
π^a [mas]	14.27 ± 0.57
distance [pc]	70.1 ± 2.9
$M_{\rm V}$ [mag]	-1.99 ± 0.09
mass[b] [$M_\odot$]	4.7
temperature[c] [K]	4625
$\log g^c$	2.30
Fe/H[c]	7.29
$v \sin i^c$ [km s^{-1}]	6.7
number of observations (Lick)	64
observed dispersion [m s^{-1}]	22.2

Table 4.3: Stellar parameters of HIP3179.

[a]Perryman & ESA (1997), [b] Bertelli et al. (1994), [c] Hekker & Meléndez (2007) (Chapter 5)

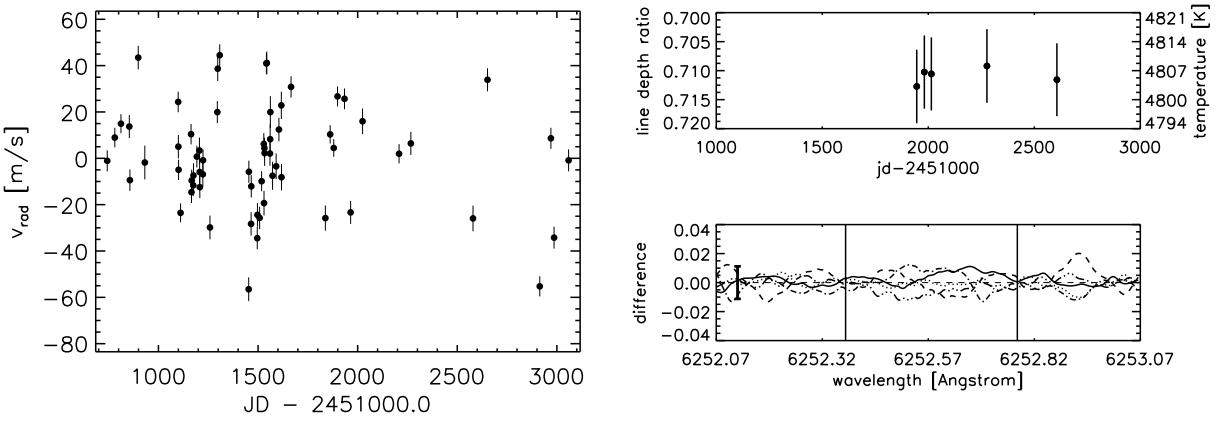

Figure 4.11: As Figure 4.10 but for HIP3179.

found and, therefore, the random variations are most likely induced by some mechanism intrinsic to the star. The temperatures obtained from the line ratios and the line depth with respect to a time average are shown in Figure 4.10. Temperature as well as spectral line depth variations accompany the random radial velocity variations and, although based on only 3 observations, provide additional information in favour of a mechanism intrinsic to the star inducing the observed radial velocity variations.

HIP3179 is a nearby K0 (bright) giant with$B-V$= 1.17 mag and an absolute magnitude of -1.99 mag, which places the star in the stable star region indicated by Hekker et al. (2006b) (Chapter 3). The observed dispersion of 22.2 m s^{-1} is only slightly higher than that adopted for stable stars (20 m s^{-1}). Stellar parameters are listed in Table 4.3 and the radial velocity observations are plotted in Figure 4.11. No periodicity was found in these data. The temperature

star	
spectral type [a]	K2III
$m_{\rm V}$ [a] [mag]	4.41
$B-V$ [a]	1.261 ± 0.000
π [a] [mas]	10.81 ± 0.97
distance [pc]	92.5 ± 9.1
$M_{\rm V}$ [mag]	-0.42 ± 0.2
mass [b] [$M_\odot$]	2.0
temperature [c] [K]	4500
$\log g$ [c]	2.55
Fe/H [c]	7.63
$v \sin i$ [c] [km s^{-1}]	3.0
number of observations (Lick)	71
residual rms scatter around fit [m s^{-1}]	18.8

Table 4.4: Stellar parameters of HIP34693.

[a]Perryman & ESA (1997), [b] Bertelli et al. (1994), [c] Hekker & Meléndez (2007) (Chapter 5)

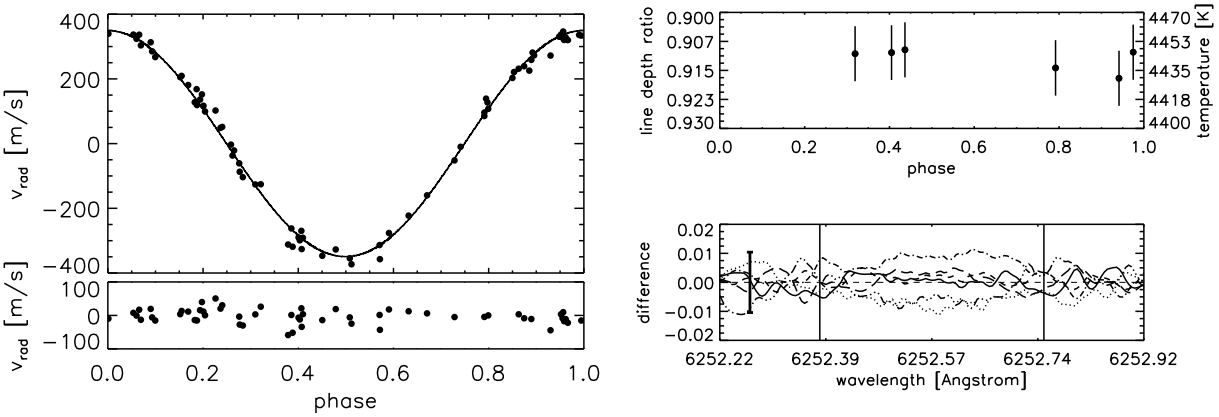

Figure 4.12: Left: radial velocity variations of HIP34693 as a function of phase. Residuals are shown in the lower part. Right: The top panel shows the temperatures obtained for each observation from the line ratio of V I at 6251.83 Å and Fe I at 6252.57 Å as a function of phase derived from the period obtained from the radial velocity variations. The lower panel shows the residual of the Fe I line at 6252.57 Å, taken at different epochs (indicated with different line styles), with respect to a time averaged profile as a function of wavelength. The vertical lines in this panel indicate the spectral line in wavelength. An error estimate is indicated with the thick error bar on the left side of the spectral line.

obtained from the line ratios and line depth are shown in Figure 4.11. Both diagnostics are constant within the error. The measurement errors prevent us from detecting small temperature or line depth variations, if any. Therefore, we cannot derive any conclusions regarding the mechanism inducing the observed radial velocity variations.

star	
spectral type[a]	K0III
$m_{\rm V}$[a] [mag]	3.32
$B-V$[a]	0.987 ± 0.035
π[a] [mas]	21.35 ± 0.79
distance [pc]	46.8 ± 1.2
$M_{\rm V}$ [mag]	-0.033 ± 0.008
mass[b] [$M_\odot$]	2.6
temperature[c] [K]	4900
$\log g$[c]	2.85
Fe/H[c]	7.55
$v \sin i$[c] [km s^{-1}]	3.0
number of observations (Lick)	107
residual rms scatter around fit [m s^{-1}]	9.8

Table 4.5: Stellar parameters of HIP88048.

[a]Perryman & ESA (1997), [b] Allende Prieto & Lambert (1999), [c] Hekker & Meléndez (2007) (Chapter 5)

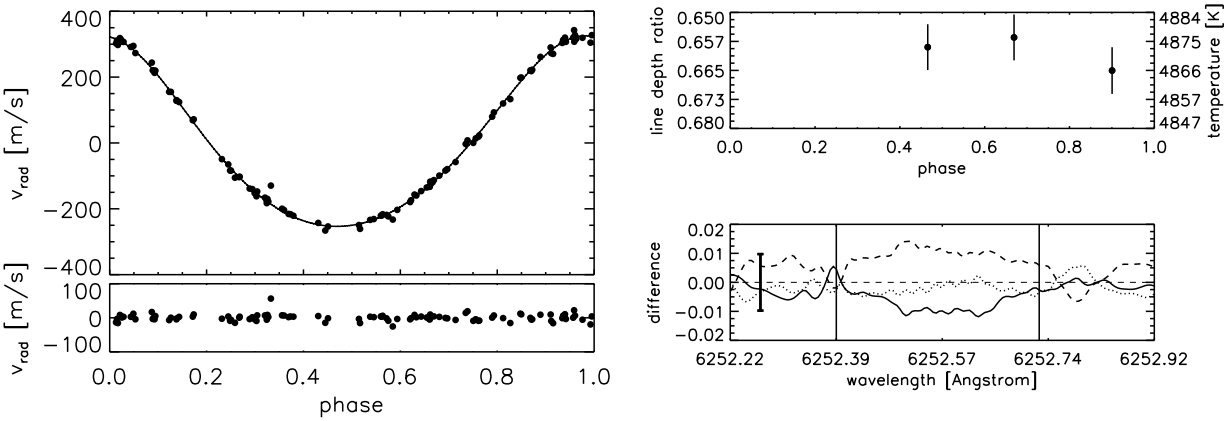

Figure 4.13: As Figure 4.12, but for HIP88048

Examples of stars with periodic radial velocity variations

HIP34693 is a K2 giant with a visual magnitude of 4.4 mag and a parallax of 10.81 mas. This means that the star has an absolute magnitude -0.43 at a distance of 92.5 pc. With $B-V$ of 1.261 the star is on the red side of the stable star region, indicated by Hekker et al. (2006b) (Chapter 3) and the scatter in the radial velocity variation is expected to be larger than 20 m s^{-1}. The star has 71 radial velocity observations spanning about 8 years which covers nearly 8 cycles. The radial velocity variations, shown in Figure 4.12, remain very consistent over this period, while no photometric variations are present in the Hipparcos photometry (Perryman & ESA 1997).

The orbit is nearly circular and the mass of the possible companion is in the brown dwarf regime. Stellar parameters of HIP34693 are listed in Table 4.4. The results of the temperature and line shape analysis are shown in the right panel of Figure 4.12. The temperatures are con-

stant within their errors, and although variations in spectral line depth seem to be present, they do not exceed the error. These features, together with the fact that this star is located above the radial velocity variation vs. $\log g$ relation (Figure 4.1) implies that the observed radial velocity variations are likely due to a sub-stellar companion. Note that this sub-stellar companion would be a brown dwarf.

HIP88048 is a nearby (d $\approx$ 47 pc) K0 giant. The colour ($B-V$ = 0.987) and absolute magnitude ($M_{\rm V}$=$-$0.033 mag) reveal that this star is in the stable star region indicated by Hekker et al. (2006b) (Chapter 3). The observed velocity dispersion of about 800 m s^{-1} can be fitted very accurately by two Keplerian orbits. Both companions would have an eccentric orbit. The rms scatter around the fit is less than 10 m s^{-1}, which would be consistent with the stable star hypothesis. The system is gravitationally stable, i.e. the companion - companion interaction does not disrupt this system. The observed radial velocities are shown in Figure 4.13. The stellar parameters are listed in Table 4.5. The Hipparcos photometry does not show periodicity comparable with the radial velocity periods. The temperatures measured from line ratios are shown in Figure 4.13. Only half a period is covered, but it seems that the temperature is not constant. Because we do not have data covering a full period it is not yet possible to draw any conclusion from this. Moreover, the residuals of the single Fe I line show variations, as can be seen in Figure 4.13, but these do not exceed the error. This star is located above the radial velocity amplitude vs. $\log g$ graph in Figure 4.1. These features, together with the very accurate two Keplerian orbits fit through the radial velocity variations provide some evidence that the radial velocity variations are caused by companions. The companions would both have $m \sin i$ in the brown dwarf region. Orbital parameters for the sub-stellar companions orbiting HIP34693 and HIP88048 will be presented in a forthcoming paper.

HIP7884 is a K3 giant with a visual magnitude of 4.45 mag at a distance of 112.9 pc. The absolute magnitude of $-$0.81 and $B-V$ of 1.347 places this star on the red side of the stable star region indicated by Hekker et al. (2006b) (Chapter 3). The observed velocity dispersion of nearly 400 m s^{-1} can be fit with a Keplerian orbit, as indicated in Figure 4.14. The rms scatter around the fit is 57.6 m s^{-1}, which is indeed larger than the 20 m s^{-1} adopted for stable stars. The temperature and line shape variations are shown in Figure 4.14. Variations in the line depth are visible, which indicate a mechanism intrinsic to the star. Due to the scarce time sampling of the SARG data, we can not correlate the periodicity of the radial velocity variations and the line shape variations. Therefore, we are not able to determine whether the intrinsic variability is causing the full observed radial velocity variation, or whether the intrinsic variability is superposed to a companion variability. The stellar parameters of HIP7884 are listed in Table 4.6.

HIP75458 (ι Draconis) is a nearby K2 giant. The colour ($B-V$ = 1.166) and absolute magnitude ($M_{\rm V}$=0.81 mag) reveal that this star is not in the stable star region indicated by Hekker et al. (2006b) (Chapter 3). The radial velocity variations are of order 700 m s^{-1} with a very regular pattern. Frink et al. (2002) published a sub-stellar companion for this star after the first full period. No line shape analysis was performed as the high eccentricity provided evidence for a companion to induce the radial velocity variation, and not some intrinsic mechanism i.e. this eccentricity is very hard to explain with pulsations or spots solely. We continued to observe HIP75458, which confirmed the periodicity and revealed a trend for a possible second

star	
spectral type[a]	K2III
$m_{\rm V}{}^a$ [mag]	4.45
$B-V^a$	1.347 ± 0.048
π^a [mas]	8.86 ± 0.77
distance [pc]	112.9 ± 10.7
$M_{\rm V}$ [mag]	-0.81 ± 0.20
mass[b] [$M_\odot$]	2.1
temperature[c] [K]	4300
$\log g^c$	2.2
Fe/H[c]	7.22
$v \sin i^c$ [km s^{-1}]	3.0
number of observations (Lick)	63
residual rms scatter around fit [m s^{-1}]	57.6

Table 4.6: Stellar parameters for HIP7884.

[a]Perryman & ESA (1997), [b] Bertelli et al. (1994), [c] Hekker & Meléndez (2007) (Chapter 5)

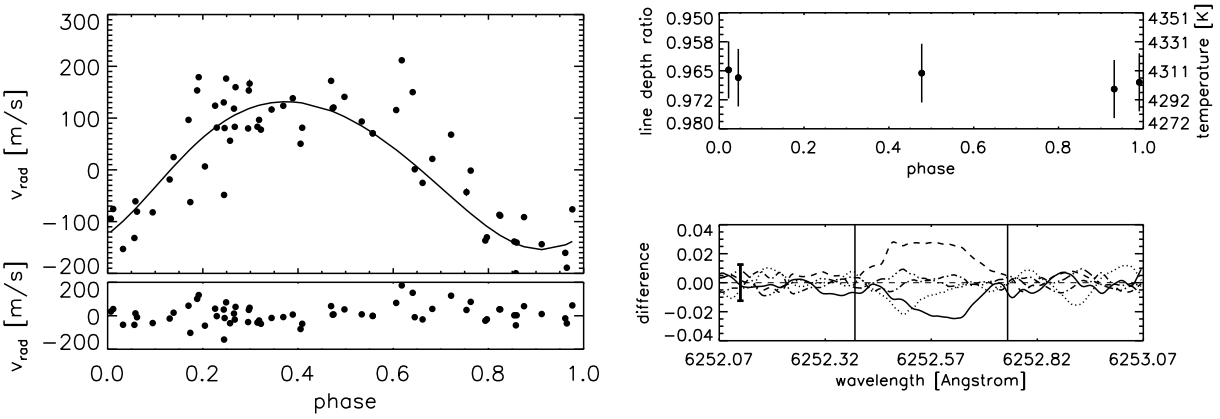

Figure 4.14: As Figure 4.12, but for HIP7884

companion in a wide orbit. The observed radial velocity variations are shown in Figure 4.15, together with results for the temperature measurements from the line ratios and spectral line depth variations. The temperature is, within the errors, constant over time, but the line depth shows variations over time, exceeding the error. The line depth variations provide an indication that at least part of the variations are caused by an intrinsic mechanism in the star, possibly superposed to the companion variability. We are unable to quantify this more precisely as we have too few line profile measurements. Therefore, it is at present impossible to disentangle intrinsic and companion variations for this star.

star	
spectral type[a]	K2III
$m_{\rm V}$[a] [mag]	3.29
$B-V$[a]	1.166 ± 0.007
π[a] [mas]	31.92 ± 0.51
distance [pc]	31.3 ± 0.5
$M_{\rm V}$ [mag]	0.81 ± 0.03
mass[b] [$M_\odot$]	1.0
temperature[c] [K]	4605
$\log g$[c]	2.95
Fe/H[c]	7.60
$v \sin i$[c] [km s^{-1}]	3.9
number of observations (Lick)	132
residual rms scatter around fit [m s^{-1}]	12.8

Table 4.7: Stellar parameters for HIP75458.

[a]Perryman & ESA (1997), [b] Allende Prieto & Lambert (1999), [c] Hekker & Meléndez (2007) (Chapter 5)

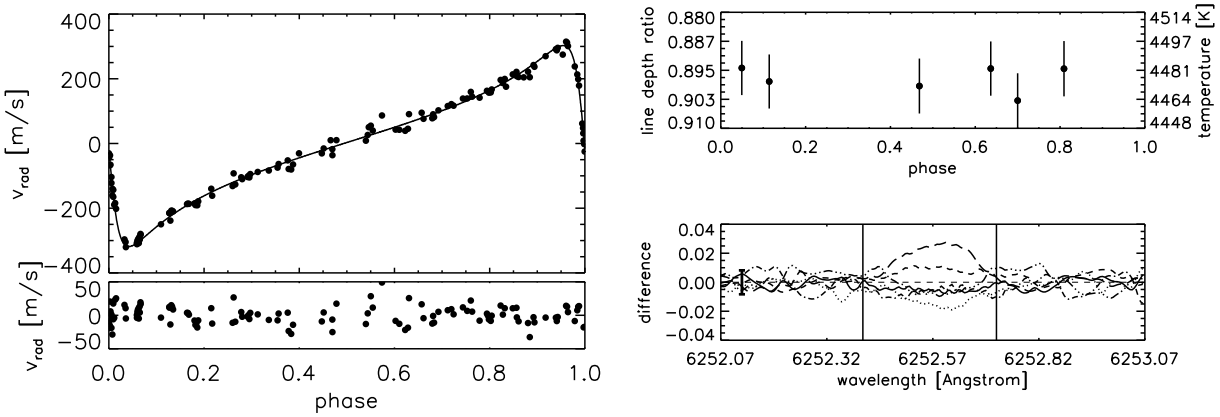

Figure 4.15: As Figure 4.12, but for HIP75458

4.5.4 Discussion of the line profile analysis

We investigated line depth variations, which are, potentially, a suitable diagnostic to detect whether the observed radial velocity variations are induced by an external or intrinsic mechanism. However, from the example of HIP3179, it is clear that a lack of observed line depth variations does not automatically mean that an external mechanism is responsible for the radial velocity variations and additional diagnostics are needed to unravel the cause of the variability.

Temperature variations are only observed for some of the stars in the sub-sample observed with SARG. This can be due to several reasons. First, if non-radial oscillation modes induce the radial velocity variations, contracting and expanding parts of the star are observed simultaneously and temperature differences between these parts may have only a very small effect on the observed quantities. Furthermore, in case of radial pulsations, the difference in radius

between the star in expanded and contracted state may yield a temperature variation below the observational errors.

For some examples (HIP34693 and HIP88048) with very accurate Keplerian fits, for which companions were expected, we add evidence for this with our line shape analysis. In cases with high eccentricity of the Kepler fit, the line shape variations may indicate intrinsic variability superposed to companion motion, as shown for HIP75458. In HIP7884 an intrinsic mechanism seems to be at work, but due to the scarce data we can not determine whether this is superposed to a companion or solely causes the observed radial velocity variations.

A more extensive time series with a time span of at least 1 full radial velocity period of temperature and line depth variations could in principle reveal a correlation between periodicities in the different diagnostics. For these data sets, it would then be possible to disentangle intrinsic and companion variations from the difference in periodicity.

4.6 CONCLUSIONS

The tight correlation we found between $\log g$ and half of the peak-to-peak radial velocity variations, seems to indicate that a large fraction of the observed radial velocity variations in our sample of K giants are induced by mechanism(s) intrinsic to the stars. On the other hand, if we assume that the radial velocity variations are caused by the reflex motion of sub-stellar companions, then the orbital parameters are considerably different from the ones observed for companions orbiting F, G and K dwarfs:

- About 25% of the stars in our sample have radial velocity variations with significant periodicity, and could possibly harbour a sub-stellar companion with $m \sin i > 1$ $\mathrm{M_{Jup}}$, while approximately only 5% of the 1330 F, G and K main sequence stars investigated by Marcy et al. (2005) have a sub-stellar companion with $m \sin i > 1$ $\mathrm{M_{Jup}}$. This is consistent with Lovis & Mayor (2007) and possibly with the theoretical predictions from the core accretion models.

- The mass, semi-major axis and period distributions differ significantly from the values obtained for sub-stellar companions orbiting F, G, and K dwarfs, e.g. higher masses, larger semi-major axis and longer periods.

- The metallicity of the companion hosting giants would be similar to the total sample mean metallicity, while a metallicity enhancement is found for companion hosting dwarfs.

The variation in line depth, measured for individual stars in the sub-sample observed with SARG, seems a potentially useful tool to identify line shape variations and deduce a possible mechanism inducing observed radial velocity variations. For three stars located above the relation in Figure 4.1, line shape analysis reveals that 2 of them may harbour brown dwarf companions, while for the third star a companion was already announced. For the latter star the companion variability is likely accompanied by processes intrinsic to the star.

A more detailed interpretation of the radial velocity and line shape variability, in terms of physical mechanisms, requires far more extensive spectroscopic time series than those assembled so far.

ACKNOWLEDGEMENT

We thank Debra Fischer, Geoff Marcy and Paul Butler for useful discussions and the development of the instrumentation and software for the determination of the radial velocities at Lick Observatory. In addition, we would like to thank the entire staff at Lick Observatory and the TNG staff for their excellent support. The observations using the TNG have been partly funded by the Optical Infrared Coordination network (OPTICON), a major international collaboration supported by the Research Infrastructures Programme of the European Commission's Sixth Framework Programme.

REFERENCES

Aerts, C. 1996, A&A, 314, 115

Aerts, C., de Pauw, M., & Waelkens, C. 1992, A&A, 266, 294

Allende Prieto, C. & Lambert, D. L. 1999, A&A, 352, 555

Armitage, P. J. & Bonnell, I. A. 2002, MNRAS, 330, L11

Bedding, T. R., Butler, R. P., Carrier, F., et al. 2006, ApJ, 647, 558

Bertelli, G., Bressan, A., Chiosi, C., Fagotto, F., & Nasi, E. 1994, A&AS, 106, 275

Biazzo, K., Frasca, A., Catalano, S., & Marilli, E. 2007, A&A, in preparation

Briquet, M. & Aerts, C. 2003, A&A, 398, 687

Brown, T. M., Kotak, R., Horner, S. D., et al. 1998, ApJS, 117, 563

Butler, R. P., Marcy, G. W., Williams, E., et al. 1996, PASP, 108, 500

Butler, R. P., Wright, J. T., Marcy, G. W., et al. 2006, ApJ, 646, 505

Dall, T. H., Santos, N. C., Arentoft, T., Bedding, T. R., & Kjeldsen, H. 2006, A&A, 454, 341

De Ridder, J., Barban, C., Carrier, F., et al. 2006, A&A, 448, 689

Doellinger, M. P., Hatzes, A. P., Pasquini, L., et al. 2007, A&A, in press

Eggenberger, P., Carrier, F., Bouchy, F., & Blecha, A. 2004, A&A, 422, 247

Fischer, D. A. & Valenti, J. 2005, ApJ, 622, 1102

Frink, S., Mitchell, D. S., Quirrenbach, A., et al. 2002, ApJ, 576, 478

Frink, S., Quirrenbach, A., Fischer, D., Röser, S., & Schilbach, E. 2001, PASP, 113, 173

Galland, F., Lagrange, A.-M., Udry, S., et al. 2006, A&A, 452, 709

Gladman, B. 1993, Icarus, 106, 247

Gonzalez, G. 1997, MNRAS, 285, 403

Gray, D. F. 2005, The Observation and Analysis of Stellar Photospheres (The Observation and Analysis of Stellar Photospheres, 3rd Edition, by D.F. Gray. ISBN 0521851866. Cambridge, UK: Cambridge University Press, 2005.)

Gray, D. F. & Brown, K. 2001, PASP, 113, 723

Hatzes, A. P. & Cochran, W. D. 1998, in Astronomical Society of the Pacific Conference Series, Vol. 154, Cool Stars, Stellar Systems, and the Sun, ed. R. A. Donahue & J. A. Bookbinder, 311

Hatzes, A. P., Cochran, W. D., Endl, M., et al. 2006, A&A, 457, 335

Hatzes, A. P., Guenther, E. W., Endl, M., et al. 2005, A&A, 437, 743

Hekker, S., Aerts, C., De Ridder, J., & Carrier, F. 2006a, A&A, 458, 931

Hekker, S. & Meléndez, J. 2007, A&A, submitted

Hekker, S., Reffert, S., Quirrenbach, A., et al. 2006b, A&A, 454, 943

Ida, S. & Lin, D. N. C. 2005, ApJ, 626, 1045

Johnson, J. A., Fischer, D. A., Marcy, G. W., et al. 2007, ApJ, in press

Johnson, J. A., Marcy, G. W., Fischer, D. A., et al. 2006, ApJ, 652, 1724

Kuschnig, R., Weiss, W. W., Gruber, R., Bely, P. Y., & Jenkner, H. 1997, A&A, 328, 544

Laughlin, G., Bodenheimer, P., & Adams, F. C. 2004, ApJ, 612, L73

Laughlin, G. & Chambers, J. E. 2001, ApJ, 551, L109

Lovis, C. & Mayor, M. 2007, A&A, 706, in press

Marcy, G., Butler, R. P., Fischer, D., et al. 2005, Progress of Theoretical Physics Supplement, 158, 24

Marcy, G. W. & Butler, R. P. 1992, PASP, 104, 270

Marcy, G. W. & Butler, R. P. 2000, PASP, 112, 137

Marcy, G. W., Butler, R. P., Vogt, S. S., et al. 2001, ApJ, 555, 418

Martić, M., Lebrun, J.-C., Appourchaux, T., & Korzennik, S. G. 2004, A&A, 418, 295

Pepe, F., Bouchy, F., Queloz, D., & Mayor, M. 2003, in ASP Conf. Ser. 294: Scientific Frontiers in Research on Extrasolar Planets, 39

Perryman, M. A. C. & ESA, eds. 1997, ESA Special Publication, Vol. 1200, The HIPPARCOS and TYCHO catalogues. Astrometric and photometric star catalogues derived from the ESA HIPPARCOS Space Astrometry Mission

Press, W. H., Teukolsky, S. A., Vetterling, W. T., & Flannery, B. P. 1992, Numerical recipes in C. The art of scientific computing (Cambridge: University Press, Ic1992, 2nd ed.)

Queloz, D., Mayor, M., Udry, S., et al. 2001, The Messenger, 105, 1

Reffert, S., Quirrenbach, A., Mitchell, D. S., et al. 2006, ApJ, 652, 661

Santos, N. C., Israelian, G., Mayor, M., et al. 2005, A&A, 437, 1127

Sato, B., Ando, H., Kambe, E., et al. 2003, ApJ, 597, L157

Scargle, J. D. 1982, ApJ, 263, 835

Setiawan, J., Hatzes, A. P., von der Lühe, O., et al. 2003, A&A, 398, L19

Setiawan, J., Rodmann, J., da Silva, L., et al. 2005, A&A, 437, L31

Valenti, J. A., Butler, R. P., & Marcy, G. W. 1995, PASP, 107, 966

CHAPTER 5

Precise radial velocities of giant stars. IV. Stellar parameters

S. Hekker and J. Meléndez

Astronomy & Astrophysics 2007, submitted

A radial velocity survey of about 380 G and K giant stars is ongoing at Lick observatory. For each star we have a high signal to noise ratio template spectrum, which we use to determine spectroscopic stellar parameters. The aim of this paper is to present spectroscopic stellar parameters, i.e. effective temperature, surface gravity, metallicity and rotational velocity for our sample of G and K giant stars. Effective temperatures, surface gravities and metallicities are determined from the equivalent width of iron lines, by imposing excitation and ionisation equilibrium through stellar atmosphere models. Rotational velocities are determined from the full width at half maximum (FWHM) of moderate spectral lines. A calibration between the FWHM and total broadening (rotational velocity and macro turbulence) is obtained from stars in common between our sample and the sample from Gray (1989). Macro turbulence is determined from the macro turbulence vs. spectral type relations from Gray (2005). The metallicity we derive is essentially equal to the literature values, while the effective temperature and surface gravity are slightly higher by 56 K and 0.15 dex, respectively. A method comparison is performed with 72 giants in common with Luck and Heiter (2007), which shows that both methods give similar results. Our rotational velocities are comparable with the ones obtained by Gray (1989), but somewhat higher than the ones obtained by de Medeiros & Mayor (1999), which is consistent with the different diagnostics used to determine them.

We are able to determine spectroscopic stellar parameters for about 380 G and K giant stars in a uniform way (112 stars are being analysed spectroscopically for the first time). For stars available in the literature, we find reasonable agreement between literature values and values determined in the present work. In addition, we show that the metallicity enhancement of companion hosting stars might also be valid for giant stars.

5.1 INTRODUCTION

For the determination of spectroscopic stellar parameters, one needs high resolution spectra with high signal to noise ratio. These spectra are available from radial velocity surveys and often used to determine stellar parameters. For instance, properties of cool stars from the Keck, Lick and AAT planet search are described by Valenti & Fischer (2005). Atmospheric parameters for stars observed by the N2K consortium (Fischer et al. 2005) are described by Robinson et al. (2007). Santos et al. (2004) and Santos et al. (2005) present stellar parameters and metallicities from the planet search using ESO facilities and the ELODIE spectrograph at the 1.93 m telescope at the Observatoire de Haute Provence. Also, basic stellar parameters for 72 evolved stars, previously studied for radial velocity variations, are presented by da Silva et al. (2006). Some of these results are not only interesting in terms of the stellar parameters, but also reveal which stars are most likely to harbour sub-stellar companions. As first shown by Gonzalez (1997), and confirmed with larger samples by Fischer & Valenti (2005) and Santos et al. (2005), metal rich stars are more likely to harbour companions than metal poor ones.

Spectroscopic stellar parameters are most commonly determined by fitting the observed spectrum directly, see for instance Valenti & Fischer (2005), or by imposing excitation and ionisation equilibrium for metal lines, using an LTE analysis and a grid of model atmospheres, see for instance Santos et al. (2004) and (2005), da Silva et al. (2006), Takeda et al. (2002) and Luck & Heiter (2007).

Rotational velocity and macro turbulence can only be determined directly with the Fourier transform technique, see for instance Gray (1989). Benz & Mayor (1981) have shown that accurate rotational velocities can also be deduced for dwarfs from a cross correlation function, by performing a calibration with the direct measurements of Gray (1989). de Medeiros & Mayor (1999) extended this technique for giant stars. Fekel (1997) used the full width at half maximum of weak to moderate spectral lines to determine rotational velocities, also by performing a calibration with the results of Gray (1989).

In 1999 a radial velocity survey of about 180 K giant stars was started at University of California Observatories / Lick Observatory, USA. This ongoing survey has recently been expanded to about 380 G and K giants. From the initial sample of 180 stars, companions have been announced for ι Draconis (Frink et al. 2002) and Pollux (Reffert et al. 2006). Stars with radial velocity variations of less than 20 $\mathrm{m\,s^{-1}}$ have been presented as stable stars by Hekker et al. (2006) (Chapter 3), and an investigation in the mechanism(s) causing the radial velocity variations is presented by Hekker et al. (2007) (Chapter 4). Some binaries discovered with this survey, as well as an extensive overview of the sample, will be presented in forthcoming papers.

In this paper we determine stellar parameters, i.e. effective temperature ($T_{\rm eff}$), surface gravity ($\log g$) and metallicity ([Fe/H]), as well as rotational velocity ($\upsilon \sin i$) for all stars in the sample. In section 2, we describe the observations. In section 3 and 4, we present the methodes

used, and results for the stellar parameters and rotational velocity, respectively. In section 5 a summary of our results is presented.

5.2 OBSERVATIONS

For the radial velocity survey, giants have been selected from the Hipparcos catalog (Perryman & ESA 1997), based on the criteria described by Frink et al. (2001). The selected stars are all brighter than 6 mag, are presumably single and have photometric variations < 0.06 mag. The survey started in 1999 at Lick observatory using the Coudé Auxiliary Telescope (CAT) in conjunction with the Hamilton échelle spectrograph (R = 60 000). The radial velocity measurements are performed with an iodine cell in the light path as described by Marcy & Butler (1992) and Valenti et al. (1995). Radial velocities are determined from the comparison of a stellar spectrum obtained with an iodine cell in the light path, and the convolution of a template iodine spectrum and a template stellar spectrum obtained without an iodine cell in the light path (Butler et al. 1996). For each target star we have a high signal to noise ratio template spectrum. These templates are used for the determination of the stellar parameters described in this paper. Thorium-Argon images taken at the beginning and end of each night are used for wavelength calibration.

5.3 EFFECTIVE TEMPERATURE, SURFACE GRAVITY, AND METALLICITY

Spectroscopic stellar parameters ($T_{\rm eff}$, $\log g$ and [Fe/H]) are determined by measuring the equivalent width (EW) of iron lines. The iron lines used in this work are listed in Table 5.1. The lines were carefully selected in order to avoid blends by atomic and CN lines. CN blends were visually inspected by comparing a synthetic spectrum computed with laboratory CN lines (Meléndez & Barbuy 1999) with the high resolution visible atlas of the cool giant Arcturus (Hinkle et al. 2000). The $\log gf$ values are based on laboratory works, in some cases with small adjustments using the Arcturus atlas. For Fe I, they are from the Oxford group (e.g. Blackwell et al. (1995)), Hannover group (e.g. Bard & Kock (1994)), O'Brian et al. (1991), May et al. (1974) and Milford et al. (1994). For Fe II, the $\log gf$ values are from the laboratory normalisation performed by Meléndez et al. (2006).

It is very time consuming to determine EWs for about 380 stars by hand, using for instance the "splot" routine from IRAF[1], and, therefore, we used the publicly available Automatic Routine for line Equivalent widths in stellar Spectra (ARES) (Sousa et al. 2007). In order to check for possible differences between the EWs determined with ARES and the ones obtained with IRAF, we plot the EWs obtained with ARES vs. the ones obtained using IRAF (see Figure 5.1). This comparison is done for a 'hot' ($T_{\rm eff}$ = 4900 K) and a 'cool' ($T_{\rm eff}$ = 4050 K) star in the sample. The nearly 1 to 1 relation between the EWs obtained with both methods shows that it

[1]IRAF is distributed by National Optical Astronomy Observatories, operated by the Association of Universities for Research in Astronomy, Inc., under contract with the National Science Foundation, U.S.A.

Ion	λ [Å]	χ [eV]	$\log gf$
Fe I	5775.080	4.220	−1.30
Fe I	5848.129	4.607	−0.9
Fe I	5902.473	4.593	−1.75
Fe I	5916.247	2.453	−2.99
Fe I	6027.050	4.076	−1.3
Fe I	6093.644	4.607	−1.41
Fe I	6096.665	3.984	−1.81
Fe I	6098.244	4.558	−1.8
Fe I	6120.249	0.915	−5.95
Fe I	6151.618	2.176	−3.30
Fe I	6187.990	3.943	−1.65
Fe I	6240.646	2.223	−3.39
Fe I	6498.939	0.958	−4.70
Fe I	6574.228	0.990	−5.00
Fe I	6703.567	2.759	−3.15
Fe I	6725.357	4.103	−2.30
Fe I	6726.666	4.607	−1.17
Fe I	7421.558	4.638	−1.80
Fe I	7547.896	5.099	−1.10
Fe I	7723.208	2.279	−3.62
Fe II	5264.812	3.230	−3.13
Fe II	5425.257	3.200	−3.22
Fe II	6247.557	3.892	−2.30
Fe II	6369.462	2.891	−4.11
Fe II	6432.680	2.891	−3.57
Fe II	6456.383	3.904	−2.05

Table 5.1: Iron lines considered in our analysis.

is reasonable to use EWs obtained with ARES. For some stars one or more lines appeared to be too strong (stronger than 200 mÅ) for a reliable parameter estimate. These lines are discarded.

From the EWs, stellar parameters are determined by imposing excitation and ionisation equilibrium through stellar atmosphere models. We performed a spectroscopic LTE analysis using the 2002 version of MOOG (Sneden 1973) and Kurucz model atmospheres, which include overshooting (Castelli et al. 1997). The resulting stellar parameters for each star are listed in Table 5.2. The reference solar iron abundance used in this work is $[Fe/H]_{\odot}$ = 7.49 and was obtained using the same grid of Kurucz models.

5.3.1 Comparison with the literature

We compare our spectroscopic stellar parameters with values obtained from the literature. These literature values are from an updated version (Ramírez & Meléndez 2005) of the Cayrel de Strobel et al. (2001) [Fe/H] catalogue, including the Luck & Heiter (2007) catalogue. If possible, suspicious literature values were corrected according to the normalisation suggested by Taylor

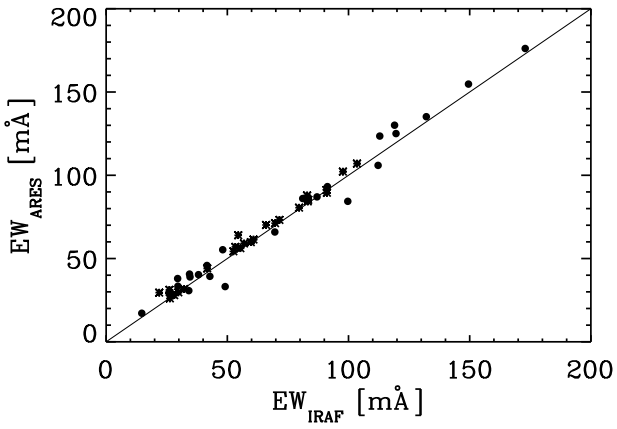

Figure 5.1: EWs obtained with the ARES software as a function of EWs computed using IRAF. The dots indicate a star with $T_{\rm eff}$ = 4050 K ('cool') and the asterisks a star with $T_{\rm eff}$ = 4900 K ('hot'). The solid line is a 1 to 1 relation.

(1999). In Figure 5.2 the difference between our spectroscopic and literature values are plotted for the temperature, surface gravity and metallicity. We find the following trimean difference and pseudo-sigma for the stellar parameters:

$$\begin{aligned} < [\mathrm{Fe/H}]^{\rm spec} - [\mathrm{Fe/H}]^{\rm lit} >= 0.01\mathrm{dex} \qquad \sigma = 0.10\mathrm{dex} \\ < \log g^{\rm spec} - \log g^{\rm lit} >= 0.15\mathrm{dex} \qquad \sigma = 0.22\mathrm{dex} \\ < T_{\rm eff}^{\rm spec} - T_{\rm eff}^{\rm lit} >= 56\mathrm{K} \qquad \sigma = 84\mathrm{K} \end{aligned}$$

The trimean T_r is a robust estimate of central tendency: T_r=(Q1+2 $\times$ median+Q3)/4 where Q1 and Q3 are the first and third quartile. The pseudo-standard deviation σ is obtained from the quartile deviation QD = (Q3-Q1)/2, employing σ = 3/2 QD (Meléndez et al. 2006).

The difference in our spectroscopic metallicity and the literature value is essentially 0 and we conclude that our metallicity scale is correct. Furthermore, our $T_{\rm eff}$ values are in good agreement with the literature, with a scatter of only 84 K, and a zero point difference of 56 K, our $T_{\rm eff}$ values being higher than the values in the literature. From the left panel of Figure 5.2 one can see that the difference is largest for the coolest stars in the sample. This might be due to the fact that the models are less accurate for low temperatures. In addition, the number of spectral lines increases with decreasing temperature, the spectra might be too crowded at lower temperatures, and also the lines get stronger and more dependent on the micro turbulence. Our results below 4000 K should be taken with caution.

The spectroscopic gravities we derived also agree well with the literature, with a scatter of only 0.22 dex, and a zero point difference of 0.15 dex. We checked whether the enhanced $\log g$ values from our spectroscopic analyses are related to the higher temperatures we obtained, compared to literature values. Hereto, we performed a test for three stars with $T_{\rm eff}$ 4170 K, 4445 K and 4980 K, respectively. We increased $T_{\rm eff}$ with 100 K and determined $\log g$, while we kept the micro turbulence fixed. For all three stars we obtained higher $\log g$ values for the increased temperatures. This reveals that the higher values for $\log g$, compared to the literature values, are related to the higher effective temperatures.

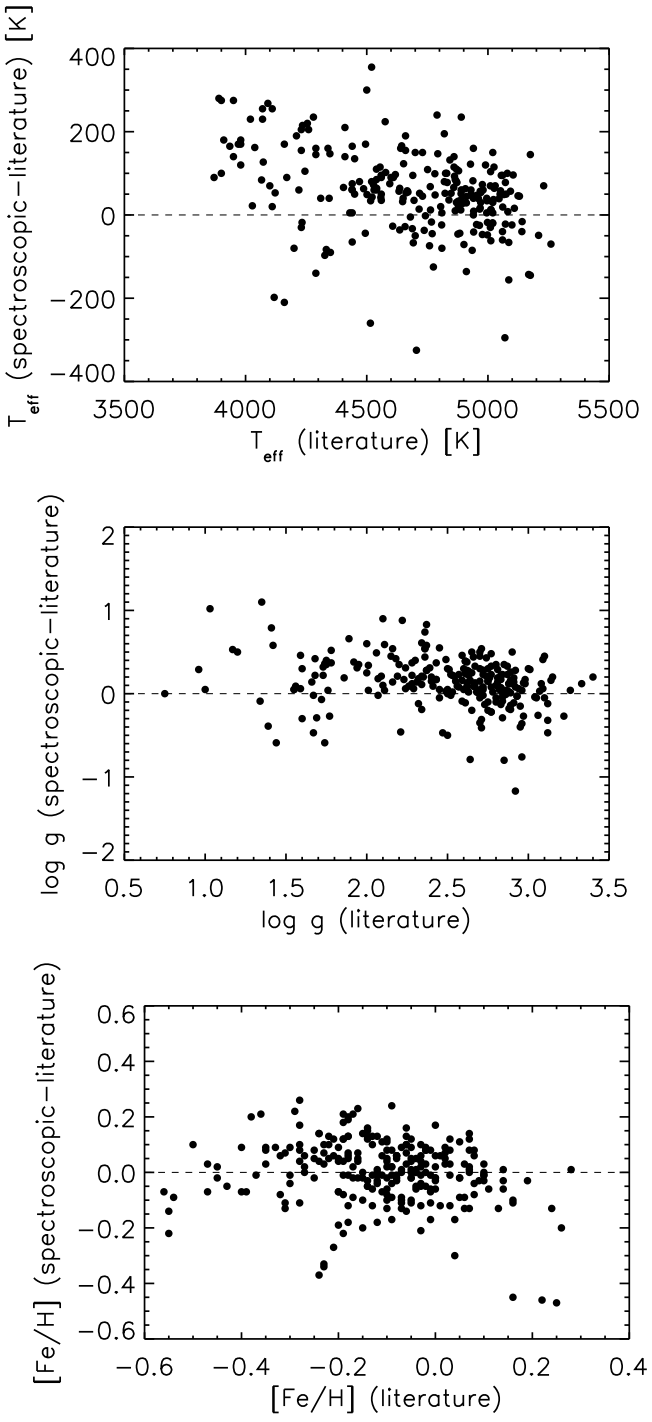

Figure 5.2: Difference between our spectroscopic values and literature values as a function of literature values for the effective temperature (top), the logarithm of the surface gravity in cgs units (centre) and metallicity (bottom).

5.3.2 Comparison with Luck & Heiter (2007)

Recently, Luck & Heiter (2007) presented a homogeneous spectroscopic analysis of 298 giants in the local region, using between 300 and 400 Fe I lines for each star and MARCS stellar models (Gustafsson et al. 2003) on spectra with R=60 000. We used the 72 stars in common between Luck & Heiter (2007) and our sample to see how well we can determine spectroscopic stellar parameters with just two dozen carefully selected iron lines instead of a few hundred iron lines. Note that different models are used for the two analyses, but spectra with the same resolution. A comparison for each parameter is shown in Figure 5.3. We find the following trimean difference and pseudo-sigma:

$$\begin{aligned} < [\mathrm{Fe/H}]^{\mathrm{spec}} - [\mathrm{Fe/H}]^{\mathrm{Luck}} >= -0.05\mathrm{dex} \qquad \sigma = 0.06\mathrm{dex} \\ < \log g^{\mathrm{spec}} - \log g^{\mathrm{Luck}} >= 0.0\mathrm{dex} \qquad \sigma = 0.15\mathrm{dex} \\ < T_{\mathrm{eff}}^{\mathrm{spec}} - T_{\mathrm{eff}}^{\mathrm{Luck}} >= -43\mathrm{K} \qquad \sigma = 35\mathrm{K} \end{aligned}$$

Our spectroscopic values are in good agreement with the ones obtained by Luck & Heiter (2007), with a scatter of only 0.06 dex for [Fe/H], 0.15 dex for $\log g$ and 35 K for the effective temperature. The mean difference in $\log g$ values is zero, while our metallicities and temperatures are slightly lower than the ones reported by Luck & Heiter (2007). These are probably systematic differences between both methods, because the pseudo-sigmas are relatively small. Luck & Heiter (2007) have benchmarked their codes against Kurucz's WIDTH and SYNTHE codes and claim that all codes yield the same result to within expected numerical accuracy and differences due to different assumptions, primarily partition functions and damping. So, most likely, the different adopted model atmospheres (MARCS vs. Kurucz) and different $\log gf$ values may cause the small systematic difference. Luck & Heiter (2007) did not publish their line list and $\log gf$ values. Since they have used a much larger number of iron lines a comparison with our $\log gf$ values is probably not meaningful.

5.3.3 Metallicity in companion hosting giants

By now 14 sub-stellar companions are announced orbiting giant stars. It seems that these giant stars with companions are metal poor, which is quite different from the known metallicity enhancement in dwarf stars hosting companions. Schuler et al. (2005) and da Silva et al. (2006) argue that giant stars with companions may be metal poor, due to a stellar mass - companion relation instead of a metallicity - companion relation. Indeed, Fischer & Valenti (2005) also find a relation between stellar mass and companions, but conclude that this is likely spurious. Here, we look at the metallicities of the giants with announced companions and compare these with the metallicities of the giants in our sample.

In Figure 5.4 the metallicity distribution of all stars in the present sample is shown together with the metallicity distribution of giant stars with announced companions. We use a two-sided Kolmogorov-Smirnov test (Press et al. 1992) to compare the distributions and find a probability of 0.75% that these are identical. The mean metallicities are -0.1 dex and 0.0 dex for the total and companions hosting sample, respectively, while the peaks of the histograms are at -0.05 dex and 0.15 dex. Gaussians fitted through the two distribution have their centres at -0.06 dex and 0.12 dex for the total and companion hosting sample, respectively. Therefore, the metallicity

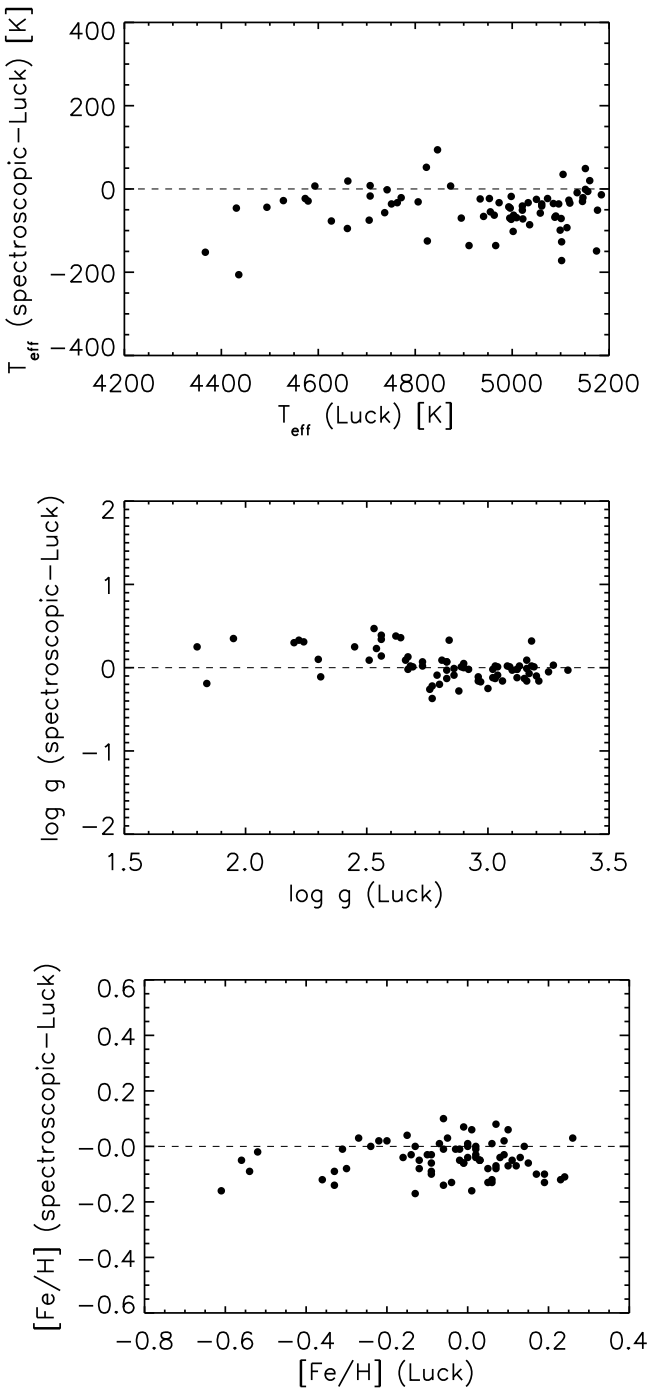

Figure 5.3: Difference between our spectroscopic values and values from Luck & Heiter (2007) as a function of Luck & Heiter (2007) values for the effective temperature (top), the logarithm of the surface gravity in cgs units (centre) and metallicity (bottom) for the 72 stars in common between the samples.

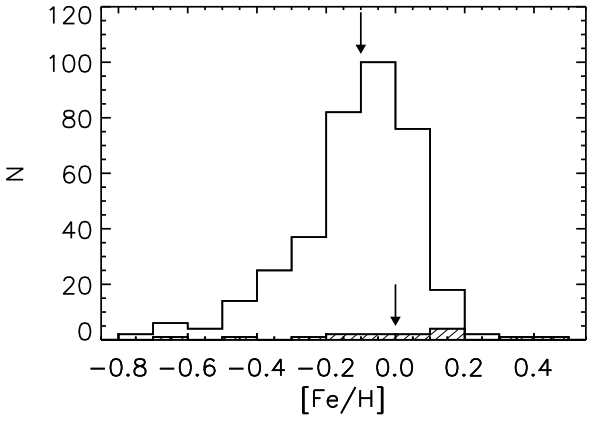

Figure 5.4: Distribution of metallicities of all stars in our sample with a mean value of -0.10 dex, indicated with the top arrow. The metallicity of 14 giants with an announced companion in the literature are plotted with the hatched histogram. These giants have a mean metallicity of 0.0 dex, which is indicated with the lower arrow.

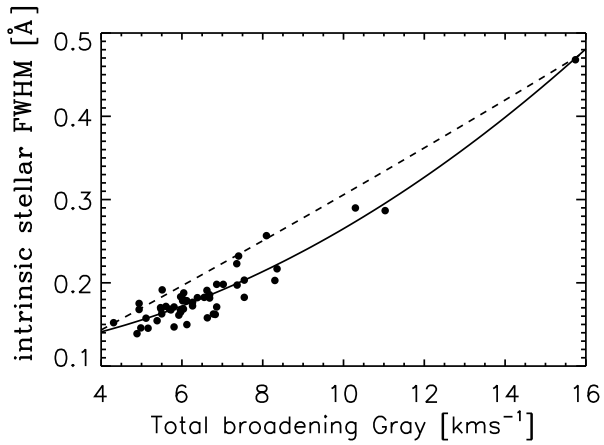

Figure 5.5: The intrinsic stellar FWHM of spectral lines as a function Gray's total broadening, for 51 stars in common between our sample and Gray (1989). The best fit (Equation (5.1)) is shown as the solid line, while the best fit obtained by Fekel (1997) is shown as the dashed line.

enhancement for companion hosting giants is 0.15 ± 0.05 dex. This is similar to the metallicity enhancement found by Fischer & Valenti (2005). Their comparison between metallicities of all stars in the sample and companion hosting dwarfs reveals that companion hosting dwarfs are more metal-rich by 0.13 dex. If they compare the metallicity enhancement as a function of stellar mass, they find also that, independent of mass, the metallicity distribution of dwarfs with companions is 0.12 dex higher than the average metallicity of all stars in the sample.

The metallicity enhancement for companion hosting giants should be taken with caution. First, it is still based on low number statistics. Second, for nearly 200 stars in our sample, we do not have a long enough time span of radial velocity observations to detect companions, in case these are present.

5.4 ROTATIONAL VELOCITY

We computed rotational velocities for our sample of giant stars, using the method described by Fekel (1997). The full width at half maximum (FWHM) for moderate spectral lines at 6432.68,

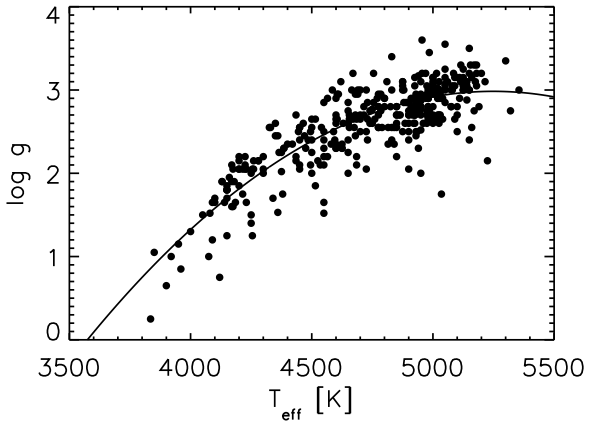

Figure 5.6: $\log g$ vs. $T_{\rm eff}$ for all stars in our sample. The solid line shows the best fit (Equation (5.2)).

6452.33, 6454.99, 6455,60, 6456.38, 6469.15 and 6471.66 Å is determined and averaged. The instrumental broadening is determined from Thorium-Argon (ThAr) images taken at the beginning and end of each night. The FWHM of several ThAr lines, in the same spectral region as the stellar lines, are determined and averaged. The intrinsic stellar broadening is computed as $\mathrm{FWHM}_{\rm intrinsic} = \sqrt{\mathrm{FWHM}^2_{\rm measured} - \mathrm{FWHM}^2_{\rm instrumental}}$.

The intrinsic stellar broadening is converted to rotational velocity $\upsilon \sin i$, using the results from Gray (1989). For the 51 stars in common (excluding 2 outliers), the intrinsic broadening is plotted as a function of the total broadening X ($X = \sqrt{(\upsilon \sin i)^2 + \upsilon^2_{\rm macro}}$) determined by Gray (1989), as shown in Figure 5.5. A second order polynomial is fitted:

$$\mathrm{FWHM}_{\rm intrinsic} = 0.10963 + 0.002758\mathrm{X} + 0.001278\mathrm{X}^2, \tag{5.1}$$

This fit is used as calibration to convert the $\mathrm{FWHM}_{\rm intrinsic}$ in Å to total broadening in km s^{-1}. Note that we only cover a total broadening between 4 and 16 km s^{-1}. All, except 2, stars in our sample fall in this range. Furthermore, our fit in Figure 5.5 is different from the fit obtained by Fekel (1997), which is shown in Figure 5.5 with the dashed line. Fekel (1997) covers a much wider range in total broadening and might not be sensitive to the curvature in the particular region discussed here. In this work we used Equation (5.1) to derive the total broadening in km s^{-1}. From this total broadening we derive the rotational velocity as $\upsilon \sin i = \sqrt{\mathrm{FWHM}^2_{\rm total} - \upsilon^2_{\rm macro}}$.

5.4.1 Macro turbulence

The macro turbulence is derived from the spectral type as shown in Figure 17.10 from Gray (2005). Each luminosity class has its own relation. We estimate the luminosity class from a $\log g$ vs. $T_{\rm eff}$ relation (Figure 5.6). Most stars in the sample are luminosity class III stars, and, therefore, the second order best fit relation, shown in Equation (5.2), is used for class III stars. This relation has a robust sigma scatter of 0.25 dex.

$$\log g_{\rm III} = -26.332 + 1.117 \cdot 10^{-2} T_{\rm eff} - 1.064 \cdot 10^{-6} T^2_{\rm eff}. \tag{5.2}$$

Stars within a factor of 2 of the $\log g_{\rm III}$ relation are considered to be class III giants, resulting in the following subdivision:

$$\begin{aligned} \text{giants:} \quad & \log g = \log g_{\rm III} \pm 0.3 \text{ dex}, \\ \text{subgiants:} \quad & \log g > \log g_{\rm III} + 0.3 \text{ dex}, \\ \text{luminous giants:} \quad & \log g < \log g_{\rm III} - 0.3 \text{ dex}. \end{aligned}$$

With the luminosity classes, we used Figure 17.10 from Gray (2005) to determine relations between $\upsilon_{\rm macro}$ and $T_{\rm eff}$ for luminosity classes II, III and IV. We found the following relations:

$$\text{class II: } \upsilon_{\rm macro} = -0.214 + 0.00158 T_{\rm eff} \qquad \sigma = 0.55 \text{ km s}^{-1} \tag{5.3}$$

$$\text{class III: } \upsilon_{\rm macro} = -3.953 + 0.00195 T_{\rm eff} \qquad \sigma = 0.45 \text{ km s}^{-1} \tag{5.4}$$

$$\text{class IV: } \upsilon_{\rm macro} = -8.426 + 0.00241 T_{\rm eff} \qquad \sigma = 0.23 \text{ km s}^{-1} \tag{5.5}$$

In case $\upsilon_{\rm macro}$ appeared to be higher than the total broadening, we used $\upsilon_{\rm macro}$ from a higher luminosity class to determine $\upsilon \sin i$. In case $\upsilon_{\rm macro}$ was still too high, we adopted $\upsilon_{\rm macro}$ = 3 km s^{-1}, as used by Fekel (1997) for G and K giants.

5.4.2 Comparison with the literature

We checked our final $\upsilon \sin i$ values by comparing the values of the 51 stars in common between our sample and the sample from Gray (1989), see Figure 5.7. The values are located around the 1 to 1 relation indicated by the solid line, which shows that the results of both samples are consistent. We also have 184 stars in common with de Medeiros & Mayor (1999) and compare our $\upsilon \sin i$ values with theirs in Figure 5.8. Our values are on average higher than the ones obtained by de Medeiros & Mayor (1999). This is probably due to the different diagnostics used. de Medeiros & Mayor (1999) show that the relation between their $\upsilon \sin i$ values, and the ones obtained by Gray (1989) for class III and IV, has an offset of 1.15 and a correlation coefficient of 1.18. We plotted the 1 to 1 relation, solid line, as well as the relation between $\upsilon \sin i$ obtained by Gray (1989) and de Medeiros & Mayor (1999) in Figure 5.8, dashed line. The data are located around this latter relation. This indicates that the difference between the results obtained here and from de Medeiros & Mayor (1999) are due to the different diagnostics used to determine $\upsilon \sin i$. Also, Luck & Heiter (2007) find that the CORAVEL $\upsilon \sin i$ values may suffer from systematic differences with respect to values derived from other techniques. For all stars $\upsilon \sin i$ and $\upsilon_{\rm macro}$ are listed in Table 5.2.

5.5 SUMMARY

We have determined spectroscopic stellar parameters for a sample of about 380 G and K giant stars. Among these, 112 stars are analysed spectroscopically for the first time. Our metallicities agree with values found in the literature and we conclude that our metallicity scale is not severely affected by systematic errors. Our temperatures are $\sim$ 50 K higher compared to the ones from the literature. The difference is largest for stars with lowest temperatures. This is

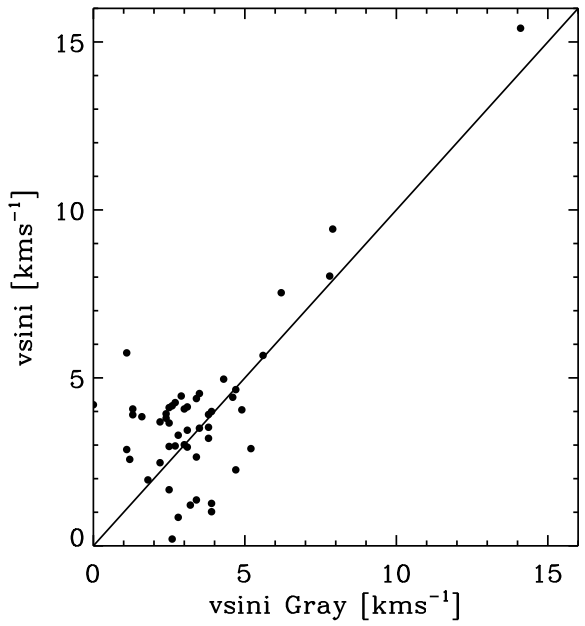

Figure 5.7: $v \sin i$ obtained in the present work vs. $v \sin i$ obtained by Gray (1989). The solid line is a 1 to 1 relation.

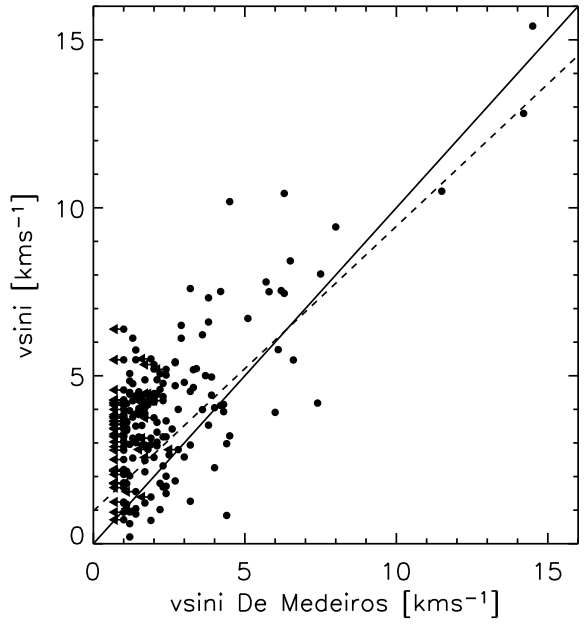

Figure 5.8: $v \sin i$ obtained in the present work vs. $v \sin i$ obtained by de Medeiros & Mayor (1999). The solid line is a 1 to 1 relation and the dashed line is relation between $v \sin i$ obtained by Gray (1989) and de Medeiros & Mayor (1999). The arrows indicate upper limits.

probably due to the lower accuracy of atmosphere models in this temperature range, the increased number and strength of spectral lines and increasing dependence on micro turbulence in cooler stars. An increase in temperature causes an increase in surface gravity and our values are 0.15 dex higher compared to the literature values.

The comparison between the mean metallicity of our total sample of giant stars and giant stars with announced companions reveals that the companion hosting stars have a 0.15 ± 0.05 dex higher metallicity than the mean metallicity of our total sample. This is in agreement with the enhanced metallicity of companion hosting dwarf stars, but based on low number statistics.

Rotational velocities are determined using the method described by Fekel (1997). Stars in common between our sample and the sample observed by Gray (1989) are used to convert FWHM of moderate lines [Å] to total line broadening [km s^{-1}]. We used a $\log g$ vs. $T_{\rm eff}$ correlation to determine the luminosity class of the stars. This luminosity class was subsequently used to calculate the macro turbulence, which has a different relation with temperature for different classes. Our data are in agreement with data obtained by Gray (1989), but are on average larger than the values obtained by de Medeiros & Mayor (1999). This is due to the different diagnostics used to determine $\upsilon \sin i$.

ACKNOWLEDGEMENT

We are very grateful to Andreas Quirrenbach, Sabine Reffert and Dave Mitchell, who started the radial velocity survey of giant stars, to allow us to use the template spectra for the present analysis. We also want to thank Conny Aerts and Ignas Snellen for carefully reading the manuscript and useful discussions.

REFERENCES

Bard, A. & Kock, M. 1994, A&A, 282, 1014

Benz, W. & Mayor, M. 1981, A&A, 93, 235

Blackwell, D. E., Lynas-Gray, A. E., & Smith, G. 1995, A&A, 296, 217

Butler, R. P., Marcy, G. W., Williams, E., et al. 1996, PASP, 108, 500

Castelli, F., Gratton, R. G., & Kurucz, R. L. 1997, A&A, 324, 432

Cayrel de Strobel, G., Soubiran, C., & Ralite, N. 2001, A&A, 373, 159

da Silva, L., Girardi, L., Pasquini, L., et al. 2006, A&A, 458, 609

de Medeiros, J. R. & Mayor, M. 1999, A&AS, 139, 433

Fekel, F. C. 1997, PASP, 109, 514

Fischer, D. A., Laughlin, G., Butler, P., et al. 2005, ApJ, 620, 481

Fischer, D. A. & Valenti, J. 2005, ApJ, 622, 1102

Frink, S., Mitchell, D. S., Quirrenbach, A., et al. 2002, ApJ, 576, 478

Frink, S., Quirrenbach, A., Fischer, D., Röser, S., & Schilbach, E. 2001, PASP, 113, 173

Gonzalez, G. 1997, MNRAS, 285, 403

Gray, D. F. 1989, ApJ, 347, 1021

Gray, D. F. 2005, The Observation and Analysis of Stellar Photospheres (The Observation and Analysis of Stellar Photospheres, 3rd Edition, by D.F. Gray. ISBN 0521851866. Cambridge, UK: Cambridge University Press, 2005.)

Gustafsson, B., Edvardsson, B., Eriksson, K., et al. 2003, in Astronomical Society of the Pacific Conference Series, Vol. 288, Stellar Atmosphere Modeling, ed. I. Hubeny, D. Mihalas, & K. Werner, 331

Hekker, S., Reffert, S., Quirrenbach, A., et al. 2006, A&A, 454, 943

Hekker, S., Snellen, I., Aerts, C., et al. 2007, A&A, in preparation

Hinkle, K., Wallace, L., Valenti, J., & Harmer, D. 2000, Visible and Near Infrared Atlas of the Arcturus Spectrum 3727-9300 A (Visible and Near Infrared Atlas of the Arcturus Spectrum 3727-9300 A ed. Kenneth Hinkle, Lloyd Wallace, Jeff Valenti, and Dianne Harmer. (San Francisco: ASP) ISBN: 1-58381-037-4, 2000.)

Luck, R. E. & Heiter, U. 2007, AJ, 133, 2464

Marcy, G. W. & Butler, R. P. 1992, PASP, 104, 270

May, M., Richter, J., & Wichelmann, J. 1974, A&AS, 18, 405

Meléndez, J. & Barbuy, B. 1999, ApJS, 124, 527

Meléndez, J., Shchukina, N. G., Vasiljeva, I. E., & Ramírez, I. 2006, ApJ, 642, 1082

Milford, P. N., O'Mara, B. J., & Ross, J. E. 1994, A&A, 292, 276

O'Brian, T. R., Wickliffe, M. E., Lawler, J. E., Whaling, J. W., & Brault, W. 1991, Journal of the Optical Society of America B Optical Physics, 8, 1185

Perryman, M. A. C. & ESA. 1997, The HIPPARCOS and TYCHO catalogues. Astrometric and photometric star catalogues derived from the ESA HIPPARCOS Space Astrometry Mission (The Hipparcos and Tycho catalogues. Astrometric and photometric star catalogues derived from the ESA Hipparcos Space Astrometry Mission, Publisher: Noordwijk, Netherlands: ESA Publications Division, 1997, Series: ESA SP Series vol no: 1200, ISBN: 9290923997 (set))

Press, W. H., Teukolsky, S. A., Vetterling, W. T., & Flannery, B. P. 1992, Numerical recipes in C. The art of scientific computing (Cambridge: University Press, Ic1992, 2nd ed.)

Ramírez, I. & Meléndez, J. 2005, ApJ, 626, 446

Reffert, S., Quirrenbach, A., Mitchell, D. S., et al. 2006, ApJ, 652, 661

Robinson, S. E., Ammons, S. M., Kretke, K. A., et al. 2007, ApJS, 169, 430

Santos, N. C., Israelian, G., & Mayor, M. 2004, A&A, 415, 1153

Santos, N. C., Israelian, G., Mayor, M., et al. 2005, A&A, 437, 1127

Schuler, S. C., Kim, J. H., Tinker, Jr., M. C., et al. 2005, ApJ, 632, L131

Sneden, C. A. 1973, PhD thesis, AA(The University of Texas in Austin.)

Sousa, S. G., Santos, N. C., Israelian, G., Mayor, M., & Monteiro, M. J. P. F. G. 2007, A&A, in press

Takeda, Y., Ohkubo, M., & Sadakane, K. 2002, PASJ, 54, 451

Taylor, B. J. 1999, A&AS, 134, 523

Valenti, J. A., Butler, R. P., & Marcy, G. W. 1995, PASP, 107, 966

Valenti, J. A. & Fischer, D. A. 2005, ApJS, 159, 141

Table 5.2: Stellar parameters: Star name, V magnitude, parallax (plx) in mas with its error (e_plx), $B-V$ colour, all from the Hipparcos catalogue (Perryman & ESA 1997), effective temperature ($T_{\rm eff}$) in Kelvin, surface gravitity ($\log g$) in dex, micro turbulence (ξ) in km s^{-1}, metallicity ([Fe/H]), rotational velocity ($\upsilon \sin i$) in km s^{-1} and macro turbulence ($\upsilon_{\rm macro}$) in km s^{-1}.

HIP	HD	V	plx	e_plx	$B-V$	$T_{\rm eff}$	$\log g$	ξ	[Fe/H]	$\upsilon \sin i$	$\upsilon_{\rm macro}$
		mag	mas	mas	mag	K	dex	km/s		km/s	km/s
379	225216	5.68	10.30	0.58	1.051	4775	2.8	1.75	7.42	0.71	5.36
1354	1239	5.74	5.08	0.58	0.898	5150	2.4	1.81	7.23	0.84	7.92
1562	1522	3.56	11.26	0.73	1.214	4500	2.25	2.0	7.52	3.37	4.82
2006	2114	5.77	5.50	1.03	0.855	5160	2.55	1.85	7.36	1.26	6.11
2497	2774	5.59	8.29	0.68	1.163	4550	2.85	1.8	7.42	3.66	2.54
2942	3421	5.45	3.19	0.77	0.886	5225	2.15	2.57	7.14	5.51	8.04
3031	3546	4.34	19.34	0.76	0.871	4975	2.6	1.65	6.88	4.12	3.56
3179	3712	2.24	14.27	0.57	1.170	4625	2.30	2.85	7.29	6.71	5.07
3193	3807	5.90	5.66	0.94	1.091	4625	2.3	1.76	7.05	1.81	5.07
3231	3817	5.30	9.47	0.81	0.891	5025	2.65	1.5	7.34	1.21	5.85
3419	4128	2.04	34.04	0.82	1.019	4925	3.05	2.2	7.40	4.07	5.65
3607	4398	5.49	9.78	0.71	0.978	4925	2.7	1.66	7.30	2.27	5.65
3760	4627	5.92	4.93	0.82	1.104	4600	2.3	1.78	7.24	3.96	2.66
4422	5395	4.62	15.84	0.58	0.957	4860	2.7	1.64	7.09	2.16	3.29
4510	5575	5.44	4.63	0.74	1.076	4725	2.05	2.23	7.24	11.27	7.25
4587	5722	5.62	10.35	0.96	0.949	4925	2.7	1.41	7.31	4.44	3.44
4906	6186	4.27	17.14	0.81	0.952	4900	2.7	1.6	7.25	3.54	3.38
4914	6203	5.40	7.95	0.86	1.106	4650	2.6	1.54	7.22	2.72	5.11
5364	6805	3.46	27.73	0.71	1.161	4600	2.9	1.85	7.56	3.78	2.66
5571	7087	4.66	7.42	0.68	1.024	4850	2.55	1.77	7.34	3.54	5.50
5742	7318	4.67	8.64	0.81	1.047	4815	2.55	1.92	7.38	6.22	5.44
6537	8512	3.60	28.48	0.77	1.065	4750	2.77	1.8	7.36	3.61	3.02
6732	8763	5.50	10.63	0.77	1.106	4690	3.0	1.95	7.48	4.46	2.88
6999	9057	5.27	11.26	0.77	0.999	4950	2.8	1.58	7.55	4.47	3.50
7607	9927	3.59	18.76	0.74	1.275	4375	2.25	1.85	7.56	2.78	4.58
7884	10380	4.45	8.86	0.77	1.347	4300	2.2	2.25	7.22	3.00	4.43
7906	10348	5.97	6.23	0.80	1.015	4885	2.6	1.8	7.43	5.50	5.57
8198	10761	4.26	12.63	0.86	0.942	5025	2.9	1.75	7.49	4.46	3.68
9110	11909	5.09	4.95	0.95	0.921	5025	2.6	1.8	7.39	3.33	7.73
9347	12274	3.99	10.84	0.79	1.554	4200	2.2	2.35	7.43	7.52	1.70
9631	12641	5.96	9.89	0.88	0.851	4875	3.1	1.42	7.34	7.61	5.55
9884	12929	2.01	49.48	0.99	1.151	4600	2.7	1.7	7.36	3.44	2.66
10234	13468	5.94	9.20	0.83	0.967	4925	2.8	1.44	7.37	0.19	5.65
10326	13692	5.86	8.17	0.81	1.006	4970	3.2	1.53	7.52	3.64	3.55
10642	14129	5.51	9.58	0.93	0.962	5000	3.05	1.79	7.42	4.00	3.62
10729	13994	5.99	4.59	0.69	1.039	4935	2.5	2.04	7.29	10.49	7.58
11220	14770	5.19	8.69	0.67	0.979	4985	2.75	1.68	7.46	0.69	5.77
11432	15176	5.55	11.39	1.04	1.114	4650	2.85	1.65	7.42	3.60	2.78
12093	16161	4.87	8.77	1.11	0.880	5170	2.75	1.62	7.31	4.70	6.13
13288	17824	4.76	17.85	0.69	0.906	5180	3.3	1.3	7.56	3.66	4.06

Table 5.2: Continued.

HIP	HD	V	plx	e_plx	$B-V$	$T_{\rm eff}$	$\log g$	ξ	[Fe/H]	$\upsilon \sin i$	$\upsilon_{\rm macro}$
		mag	mas	mas	mag	K	dex	km/s		km/s	km/s
13339	17656	5.86	8.21	0.79	0.903	5150	3.0	1.37	7.53	2.91	6.09
13701	18322	3.89	24.49	0.72	1.088	4700	3.00	1.58	7.46	2.92	2.90
13905	18449	4.94	9.31	0.78	1.235	4500	2.65	1.93	7.42	3.14	4.82
13965	18474	5.47	5.85	0.75	0.869	4940	2.3	1.59	7.18	2.97	5.68
14668	19476	3.79	29.05	0.66	0.980	4950	3.1	1.65	7.55	1.79	3.50
14817	19656	4.61	10.69	0.80	1.115	4600	2.3	1.89	7.31	2.57	5.02
14838	19787	4.35	19.44	1.23	1.033	4875	3.05	1.68	7.59	2.15	3.32
15549	20644	4.47	5.09	0.90	1.555	4100	1.65	3.0	7.05	5.77	4.04
15696	20825	5.55	3.35	1.16	1.100	4775	2.55	2.18	7.32	9.43	5.36
15861	21017	5.50	14.18	0.98	1.190	4620	3.1	1.75	7.66	3.37	2.71
16335	21552	4.36	9.23	0.83	1.367	4215	2.05	1.87	7.29	2.21	4.27
16358	21755	5.93	6.31	0.96	0.953	5140	3.05	1.62	7.46	4.59	3.96
16780	22409	5.56	8.60	0.77	0.915	4980	2.8	1.51	7.18	3.33	3.58
16989	22675	5.86	8.35	0.74	0.980	5000	3.0	1.34	7.60	4.41	3.62
17103	22796	5.55	8.14	0.85	0.931	4990	3.0	1.6	7.33	2.15	5.78
18212	24240	5.76	7.58	0.78	1.040	4850	2.7	1.91	7.48	4.38	5.50
19009	25555	5.46	3.42	0.90	0.813	4360	1.53	1.68	7.16	5.78	6.67
19011	25723	5.62	8.12	0.84	1.062	4775	2.7	1.67	7.46	3.66	3.08
19388	26162	5.51	11.21	0.87	1.077	4800	2.9	1.7	7.55	4.00	3.14
19483	26409	5.44	8.65	0.82	0.941	5000	2.8	1.66	7.45	2.52	5.80
19996	27179	5.95	5.92	0.76	1.078	4850	2.6	1.77	7.55	5.79	5.50
20241	27278	5.95	9.42	0.79	0.962	4950	2.95	1.47	7.40	3.75	3.50
20250	27382	4.97	9.53	0.92	1.150	4550	2.5	1.57	7.17	0.94	4.92
20252	27348	4.93	14.42	0.83	0.950	5050	3.07	1.33	7.60	4.14	3.74
20268	27497	5.76	7.62	0.93	0.914	5180	3.2	1.37	7.63	0.88	6.15
20455	27697	3.77	21.29	0.93	0.983	5000	3.0	1.5	7.58	2.96	5.80
20732	28100	4.69	7.17	0.81	0.979	4930	2.45	1.77	7.25	4.96	5.66
20885	28307	3.84	20.66	0.85	0.952	5000	3.0	1.45	7.57	4.38	3.62
20889	28305	3.53	21.04	0.82	1.014	4910	2.75	1.73	7.54	3.66	5.62
21248	29085	4.49	26.22	0.71	0.972	4875	3.1	1.35	7.29	2.15	3.32
21421	29139	0.87	50.09	0.95	1.538	4100	1.70	2.45	7.13	5.20	4.04
21743	29737	5.56	10.34	0.69	0.926	4980	2.8	1.42	7.20	1.48	3.58
22220	30138	5.99	7.36	0.85	0.934	4920	2.9	1.71	7.43	2.98	5.64
22860	31414	5.71	6.85	0.63	0.953	5150	3.0	1.93	7.57	5.25	6.09
23015	31398	2.69	6.37	0.96	1.490	3950	1.15	2.57	7.31	7.32	3.75
23123	31767	4.47	3.42	0.86	1.369	4250	1.4	2.35	7.26	4.17	6.50
23685	32887	3.19	14.39	0.68	1.460	4150	1.8	2.2	7.30	4.30	4.14
24294	33833	5.90	7.31	0.74	0.960	4980	3.0	1.54	7.46	3.24	3.58
24822	34559	4.96	15.83	0.86	0.937	5060	3.1	1.53	7.52	3.02	3.77
25247	35369	4.13	18.71	0.74	0.943	4950	2.8	1.46	7.32	2.72	3.50
27280	38527	5.78	10.88	0.86	0.888	5125	3.05	1.32	7.42	1.71	6.04
27483	38656	4.51	15.34	0.80	0.949	4980	2.9	1.46	7.37	4.22	3.58
27588	39118	5.97	2.89	0.83	0.953	4550	1.52	2.16	7.15	4.19	6.97

Table 5.2: Continued.

HIP	HD	V	plx	e_plx	$B-V$	$T_{\rm eff}$	$\log g$	ξ	[Fe/H]	$\upsilon \sin i$	$\upsilon_{\rm macro}$
		mag	mas	mas	mag	K	dex	km/s		km/s	km/s
27629	39004	5.60	8.66	0.98	0.978	5000	3.05	1.66	7.50	3.80	5.80
28812	41361	5.67	2.96	0.87	1.047	4900	2.4	1.95	7.38	3.88	7.53
28814	41380	5.63	1.31	0.76	1.041	4900	2.5	2.9	7.20	12.81	7.53
29379	42398	5.83	4.33	0.83	1.110	4650	2.4	1.54	7.34	4.20	2.78
29575	43023	5.83	10.36	0.73	0.910	5140	3.1	1.41	7.53	3.85	3.96
30457	44951	5.21	7.76	0.74	1.230	4500	2.4	1.92	7.26	3.76	4.82
30720	45433	5.55	4.35	0.86	1.376	4200	1.85	2.0	7.41	4.70	4.24
31159	46241	5.88	6.30	0.94	0.997	4925	2.7	1.59	7.42	3.87	3.44
31592	47205	3.95	50.41	0.70	1.037	4830	3.4	1.45	7.70	1.15	3.00
31700	47442	4.42	7.03	0.62	1.137	4550	2.3	1.8	7.40	4.31	4.92
32249	48433	4.49	11.82	0.83	1.167	4550	2.2	1.76	7.29	2.17	4.92
32562	48781	5.22	7.69	0.78	1.131	4725	2.5	1.82	7.41	2.55	5.26
32814	49738	5.68	2.17	0.88	1.329	4300	2.0	2.35	7.44	5.60	4.43
33152	50877	3.89	1.65	0.62	1.740	3900	0.65	4.0	7.17	12.31	5.95
33160	50778	4.08	12.94	0.87	1.418	4050	1.5	1.8	7.10	4.27	3.94
33421	51000	5.91	8.47	0.92	0.878	5180	3.05	1.55	7.45	2.26	6.15
33449	50522	4.35	19.14	0.76	0.850	4775	2.8	0.94	7.45	2.94	5.36
33856	52877	3.49	2.68	0.59	1.729	3850	1.05	3.5	7.20	10.76	3.55
33914	52556	5.78	5.06	0.85	1.140	4700	2.65	2.3	7.41	3.84	5.21
34033	52960	5.14	4.39	0.72	1.391	4150	1.8	2.0	7.41	5.33	4.14
34267	53329	5.55	10.68	0.88	0.909	4950	2.7	1.62	7.03	4.26	3.50
34387	54079	5.74	5.74	0.86	1.176	4450	2.1	1.8	7.07	3.04	4.72
34693	54719	4.41	10.81	0.97	1.261	4500	2.55	1.96	7.63	3.03	4.82
34987	55751	5.36	4.35	0.89	1.193	4550	2.1	1.86	7.38	3.74	4.92
35476	56989	5.90	6.27	0.85	1.069	4790	2.55	1.43	7.50	7.79	5.39
35615	57478	5.59	5.86	0.74	0.971	5090	2.65	1.94	7.41	8.40	7.83
35907	57669	5.23	4.48	0.96	1.249	4500	2.0	2.35	7.42	3.21	6.90
36041	58367	4.99	3.30	0.88	0.991	4900	2.05	2.04	7.37	4.22	7.53
36388	59311	5.60	2.00	0.94	1.493	4225	2.2	2.3	7.30	5.35	1.76
36616	59686	5.45	10.81	0.75	1.126	4650	2.75	1.68	7.64	4.28	2.78
36848	60666	5.78	10.41	0.67	1.045	4750	2.6	1.38	7.47	4.03	3.02
36962	60522	4.06	13.57	0.87	1.540	4130	1.9	2.6	7.13	5.19	4.10
37204	60986	5.58	10.65	0.97	0.921	5200	3.2	1.46	7.65	3.44	4.11
37364	61774	5.92	4.53	0.71	1.158	4680	2.45	1.58	7.43	1.78	5.17
37447	61935	3.94	22.61	0.80	1.022	4825	2.8	1.6	7.50	0.70	5.46
37740	62345	3.57	22.73	0.83	0.932	5030	2.95	1.58	7.47	4.36	3.70
37826	62509	1.16	96.74	0.87	0.991	4925	3.15	1.65	7.56	1.67	3.44
38253	63752	5.60	2.32	1.03	1.446	4075	1.0	2.38	7.14	6.21	6.22
38375	64152	5.62	11.90	0.73	0.956	4930	2.85	1.7	7.41	2.60	3.46
38962	65345	5.30	12.33	0.96	0.933	5020	3.02	1.34	7.55	3.41	3.67
39079	65695	4.93	13.06	0.96	1.205	4470	2.45	1.7	7.34	1.85	4.76
39177	65759	5.60	4.52	1.01	1.317	4300	2.05	1.9	7.55	5.73	4.43
39191	65714	5.87	2.90	0.89	1.021	4920	2.6	1.76	7.55	2.50	5.64

Table 5.2: Continued.

HIP	HD	V	plx	e_plx	$B-V$	$T_{\rm eff}$	$\log g$	ξ	[Fe/H]	$\upsilon \sin i$	$\upsilon_{\rm macro}$
		mag	mas	mas	mag	K	dex	km/s		km/s	km/s
40107	68312	5.36	10.32	0.87	0.892	5150	3.2	1.44	7.47	2.25	3.99
40305	68077	5.88	6.59	0.73	1.016	4940	2.8	1.82	7.49	4.15	5.68
40526	69267	3.53	11.23	0.97	1.481	4200	2.05	2.3	7.30	4.88	4.24
40866	69994	5.80	6.39	0.82	1.137	4650	2.6	1.57	7.42	3.15	2.78
41075	70272	4.25	8.39	0.79	1.550	4175	2.05	2.8	7.25	5.41	4.19
41704	71369	3.35	17.76	0.65	0.856	5190	2.8	1.84	7.33	3.93	6.17
41909	72292	5.33	10.46	0.89	1.252	4450	2.55	1.68	7.64	2.89	4.72
42008	72561	5.89	0.60	1.09	1.066	4840	2.35	2.32	7.33	3.91	7.43
42402	73471	4.45	9.25	0.94	1.216	4550	2.4	2.1	7.54	2.95	4.92
42911	74442	3.94	23.97	0.83	1.083	4730	2.65	1.55	7.56	3.78	2.97
43409	75691	4.02	15.63	0.58	1.272	4450	2.55	1.7	7.47	2.21	4.72
43531	75506	5.15	11.91	0.72	0.971	4830	2.55	1.6	7.15	4.05	3.21
43813	76294	3.11	21.64	0.99	0.978	4840	2.55	1.73	7.33	3.18	5.49
43834	76219	5.23	5.68	0.84	1.000	4950	2.9	1.99	7.37	10.43	5.70
43923	76291	5.72	14.21	0.78	1.125	4665	3.0	1.63	7.42	2.02	2.82
44154	76813	5.23	10.19	0.75	0.913	5020	2.9	1.47	7.45	1.87	5.84
44356	77353	5.64	5.32	0.85	1.163	4525	2.15	1.89	7.11	3.04	4.87
44406	77445	5.85	4.91	0.91	1.100	4760	2.65	1.78	7.44	4.34	3.05
44659	77996	4.99	2.69	0.93	1.189	4380	1.75	1.88	7.37	2.32	6.71
44818	78235	5.42	12.56	0.81	0.888	5170	3.3	1.38	7.50	5.39	4.03
44936	78668	5.76	7.09	0.93	0.937	5000	2.65	1.39	7.42	3.72	5.80
45412	79452	5.98	7.17	0.90	0.839	5100	2.7	1.9	6.86	10.18	5.99
46390	81797	1.99	18.40	0.78	1.440	4200	2.15	2.5	7.44	6.20	1.70
46652	82087	5.87	6.33	0.90	1.032	4850	2.8	1.7	7.46	0.24	5.50
46750	82308	4.32	9.69	0.89	1.541	4000	1.3	2.3	7.19	6.12	3.85
46880	82734	5.02	9.76	0.69	1.023	4980	2.9	1.95	7.60	6.60	5.76
46952	82635	4.54	18.52	0.88	0.914	5150	3.5	1.55	7.51	6.59	3.99
46982	82870	5.56	4.79	0.83	1.159	4600	2.6	1.85	7.46	4.09	2.66
47029	82741	4.81	14.23	0.81	0.992	4910	2.9	1.62	7.32	3.88	3.41
47189	83189	5.73	3.42	0.93	1.223	4450	2.05	2.04	7.55	8.88	4.72
47431	83618	3.90	11.83	0.80	1.313	4400	2.35	1.9	7.42	2.43	4.63
47570	83805	5.61	9.59	0.74	0.951	5020	2.9	1.65	7.43	4.45	3.67
47959	84561	5.67	4.65	0.92	1.489	4225	2.05	2.23	7.17	3.50	4.29
48356	85444	4.11	11.92	0.81	0.918	5090	3.05	1.67	7.47	1.67	5.97
48455	85503	3.88	24.52	0.87	1.222	4565	2.9	1.95	7.78	5.06	2.58
48734	86080	5.85	4.84	0.78	1.129	4650	2.25	1.79	7.24	1.44	5.11
48802	85945	5.97	6.99	0.64	0.895	5160	3.15	1.47	7.53	7.53	6.11
50027	88547	5.77	6.19	0.89	1.178	4375	2.02	2.0	6.96	2.78	4.58
50336	89024	5.84	10.35	0.90	1.206	4755	3.2	2.6	7.28	4.60	3.03
51069	90432	3.83	13.14	0.79	1.456	4225	2.1	2.15	7.37	5.87	4.29
51775	91612	5.07	10.23	0.78	0.921	5025	2.95	1.42	7.38	4.03	3.68
52689	93291	5.49	11.34	0.86	0.908	5080	3.05	1.45	7.43	3.67	3.82
52943	93813	3.11	23.54	0.81	1.232	4435	2.2	2.0	7.24	1.76	4.70

Table 5.2: Continued.

HIP	HD	V	plx	e_plx	$B-V$	$T_{\rm eff}$	$\log g$	ξ	[Fe/H]	$\upsilon \sin i$	$\upsilon_{\rm macro}$
		mag	mas	mas	mag	K	dex	km/s		km/s	km/s
53229	94264	3.79	33.40	0.78	1.040	4725	3.0	1.58	7.38	1.81	2.00
53261	94247	5.12	4.82	0.62	1.355	4385	2.3	2.2	7.28	3.61	4.60
53316	94481	5.65	7.97	0.83	0.832	5355	3.0	1.58	7.52	4.00	4.48
53740	95272	4.08	18.71	1.03	1.079	4785	2.95	1.75	7.50	3.76	5.38
53781	95212	5.47	3.70	0.78	1.466	4150	1.85	2.1	7.26	3.77	4.14
54539	96833	3.00	22.21	0.68	1.144	4655	2.55	2.0	7.35	3.38	2.79
55086	97989	5.88	7.74	0.73	1.102	4755	2.85	2.98	7.14	3.58	3.03
55282	98430	3.56	16.75	0.82	1.112	4580	2.35	1.9	7.06	2.40	4.98
55650	99055	5.39	8.93	0.83	0.938	5020	2.7	1.71	7.34	4.52	3.67
55716	99196	5.80	6.97	0.85	1.376	4215	1.75	2.1	7.14	4.26	4.27
55797	99283	5.73	9.38	0.71	0.988	4930	2.85	1.67	7.31	4.28	3.46
55945	99648	4.95	5.25	0.84	1.000	4950	2.52	1.87	7.42	4.40	5.70
56647	100920	4.30	18.31	0.89	0.983	4910	2.8	1.61	7.33	4.27	3.41
57399	102224	3.69	16.64	0.60	1.181	4495	2.1	2.05	7.05	1.18	4.81
58181	103605	5.83	10.34	0.63	1.101	4630	2.6	1.9	7.32	3.18	5.08
58654	104438	5.59	9.01	0.77	1.019	4875	3.0	1.64	7.43	3.64	3.32
58948	104979	4.12	19.08	0.77	0.967	4950	2.77	1.68	7.07	1.55	5.70
59316	105707	3.02	10.75	0.71	1.326	4475	2.3	2.9	7.31	5.28	4.77
59501	106057	5.60	6.73	0.74	0.961	5000	2.95	1.68	7.41	3.19	3.62
59847	106714	4.93	13.12	0.88	0.957	4850	2.8	1.87	7.29	2.14	5.50
60202	107383	4.72	9.04	0.86	1.010	4880	3.0	1.67	7.25	0.60	5.56
60485	107950	4.76	8.30	0.58	0.877	5100	2.5	1.7	7.37	5.47	7.84
60646	108225	5.01	14.35	0.60	0.955	5050	3.0	1.5	7.57	4.39	3.74
60742	108381	4.35	19.18	0.83	1.128	4675	2.55	1.68	7.65	3.52	2.84
61420	109519	5.86	5.00	0.84	1.242	4495	2.5	2.65	7.30	5.42	4.81
61571	109742	5.70	6.29	0.85	1.436	4280	2.15	2.25	7.36	4.22	4.39
62103	110646	5.91	14.26	0.77	0.850	5000	3.07	1.29	7.01	1.59	3.62
63533	113095	5.97	8.14	0.78	0.971	4975	2.95	1.57	7.45	1.49	5.75
63608	113226	2.85	31.90	0.87	0.934	5115	3.1	1.71	7.58	1.69	6.02
64078	114038	5.15	10.66	0.84	1.138	4715	2.8	1.69	7.55	1.33	5.24
64540	115004	4.94	6.24	0.68	1.061	4730	2.4	1.91	7.39	7.50	5.27
64823	115478	5.33	10.94	1.00	1.304	4350	2.6	1.76	7.59	4.88	2.06
64962	115659	2.99	24.69	0.70	0.920	5110	2.9	1.55	7.52	3.35	6.01
65301	116292	5.36	10.20	0.73	0.987	4940	2.75	1.55	7.42	2.26	5.68
65323	116365	5.88	2.81	0.86	1.431	4180	1.9	2.06	7.16	4.87	4.20
66098	117818	5.21	12.36	0.78	0.964	4900	2.7	1.63	7.18	3.87	3.38
66320	118219	5.70	8.80	0.76	0.950	4915	2.7	1.55	7.24	1.37	5.63
66907	119458	5.98	6.71	0.76	0.857	5125	3.0	1.66	7.40	4.05	6.04
67210	120048	5.92	8.08	0.63	0.948	5100	3.15	1.48	7.55	2.58	5.99
67459	120477	4.05	13.29	0.81	1.520	4170	1.60	2.60	6.92	5.06	4.18
67545	120602	6.00	8.09	0.81	0.899	5140	2.88	1.59	7.35	3.82	6.07
68895	123123	3.25	32.17	0.77	1.091	4670	2.65	1.8	7.33	2.25	2.83
69427	124294	4.18	14.59	0.95	1.323	4175	1.6	1.9	7.02	4.13	4.19

Table 5.2: Continued.

HIP	HD	V	plx	e_plx	$B-V$	$T_{\rm eff}$	$\log g$	ξ	[Fe/H]	$\upsilon \sin i$	$\upsilon_{\rm macro}$
		mag	mas	mas	mag	K	dex	km/s		km/s	km/s
69673	124897	-0.05	88.85	0.74	1.239	4230	1.65	1.95	6.86	3.80	4.30
70469	126218	5.34	8.16	0.87	0.962	5125	3.0	1.72	7.64	4.59	3.93
70791	127243	5.58	10.59	0.61	0.864	5030	2.7	2.05	6.79	3.99	3.70
71053	127665	3.57	21.92	0.81	1.298	4385	2.3	2.17	7.30	3.14	4.60
71832	129312	4.86	5.66	0.82	0.992	4925	2.6	1.74	7.39	8.42	5.65
71837	129336	5.55	8.46	0.86	0.941	4980	2.9	1.67	7.22	3.41	3.58
72125	129972	4.60	14.48	0.79	0.972	4980	2.9	1.72	7.43	0.80	5.76
72210	129944	5.80	8.91	0.96	0.980	4865	2.7	1.8	7.19	4.02	3.30
72571	130694	4.42	10.68	0.83	1.366	4250	2.0	2.13	6.80	4.23	4.33
72934	131530	5.78	8.94	0.96	0.982	5015	3.2	1.49	7.53	0.85	5.83
73133	131918	5.48	6.06	0.79	1.491	4140	1.65	2.25	7.25	4.96	4.12
73166	132146	5.72	5.28	0.81	0.951	5075	2.8	1.84	7.46	2.83	5.94
73555	133208	3.49	14.91	0.57	0.956	5100	2.8	1.8	7.49	2.64	5.99
73620	133165	4.39	17.78	0.90	1.026	4700	2.7	1.9	7.19	2.24	2.90
73909	134190	5.24	12.53	0.53	0.958	4830	2.4	1.7	7.02	3.45	3.21
74239	134373	5.75	7.25	1.00	1.045	4900	2.85	2.0	7.45	4.26	5.60
74666	135722	3.46	27.94	0.61	0.961	4900	2.75	1.65	7.11	2.87	3.38
74732	135534	5.52	6.52	1.16	1.357	4365	2.25	1.92	7.56	4.24	4.56
75352	136956	5.72	5.41	0.77	1.039	5040	2.9	1.67	7.60	2.55	5.88
75458	137759	3.29	31.92	0.51	1.166	4605	2.95	1.73	7.60	3.93	2.67
75730	137744	5.64	3.59	0.93	1.545	4230	2.05	2.25	7.29	5.10	4.30
75944	138137	5.82	5.78	0.83	1.056	4935	2.75	1.98	7.45	3.36	5.67
76425	139195	5.26	13.89	0.70	0.925	5000	3.15	1.56	7.37	3.56	3.62
76810	140027	6.00	7.24	0.79	0.908	5215	3.1	1.61	7.48	4.50	4.14
77512	141714	4.59	19.71	0.73	0.794	5300	3.35	1.48	7.23	5.62	4.35
77738	142531	5.81	9.09	0.51	0.972	5000	3.15	1.52	7.58	3.07	3.62
77853	142198	4.13	20.02	0.88	1.003	4685	2.2	1.67	7.14	3.06	5.18
78132	142980	5.54	14.36	0.80	1.141	4610	2.95	1.76	7.46	4.58	2.68
78442	143553	5.82	13.62	0.79	1.003	4810	3.10	1.33	7.34	3.01	3.17
78990	144608	4.31	12.32	0.89	0.831	5320	2.75	1.85	7.44	3.50	6.42
79195	145206	5.39	6.60	0.91	1.446	4160	1.95	2.65	7.23	2.91	4.16
79540	145897	5.24	7.43	0.91	1.394	4350	2.45	1.87	7.48	3.98	2.06
79882	146791	3.23	30.34	0.79	0.966	4970	2.9	1.52	7.42	3.50	3.55
80331	148387	2.73	37.18	0.45	0.910	5110	3.15	1.55	7.48	3.69	3.89
80343	147700	4.48	18.32	0.89	0.996	4775	2.55	1.71	7.29	1.72	5.36
80693	148513	5.41	7.72	0.87	1.461	4200	2.05	2.15	7.47	3.21	4.24
80894	148786	4.29	15.53	0.77	0.924	5175	3.1	1.68	7.65	5.01	6.14
81660	151101	4.84	4.79	0.45	1.212	4535	2.1	2.28	7.36	1.17	6.95
81724	150416	4.91	8.34	0.85	1.095	5000	2.6	1.86	7.36	5.19	7.69
81833	150997	3.48	29.11	0.52	0.916	5020	3.0	1.43	7.29	2.47	5.84
83000	153210	3.19	37.99	0.75	1.160	4655	2.7	1.82	7.56	2.16	5.12
83254	153834	5.69	1.07	0.74	1.332	4340	1.7	2.61	7.34	5.23	6.64
84380	156283	3.16	8.89	0.52	1.437	4170	1.9	2.26	7.50	6.12	4.18

Table 5.2: Continued.

HIP	HD	V	plx	e_plx	$B-V$	$T_{\rm eff}$	$\log g$	ξ	[Fe/H]	$\upsilon \sin i$	$\upsilon_{\rm macro}$
		mag	mas	mas	mag	K	dex	km/s		km/s	km/s
84671	156681	5.03	4.72	0.80	1.539	4170	2.1	2.25	7.28	5.47	1.62
84950	157681	5.69	5.52	0.51	1.463	4255	2.05	2.18	7.30	3.78	4.34
85139	157617	5.77	3.03	0.79	1.251	4565	2.2	2.47	7.46	7.34	4.95
85355	157999	4.34	2.78	0.92	1.480	4080	1.52	2.54	7.42	7.51	4.00
85693	158899	4.41	8.88	0.64	1.434	4325	2.55	2.62	7.40	6.22	2.00
85715	158974	5.63	8.65	0.56	0.960	5090	3.15	1.57	7.58	2.01	5.97
85888	159501	5.72	8.62	0.53	1.089	4685	2.65	1.77	7.20	0.94	2.86
86742	161096	2.76	39.78	0.75	1.168	4680	2.95	2.02	7.62	3.84	2.85
87808	163770	3.86	4.87	0.54	1.350	4255	1.25	2.75	7.38	7.45	6.51
87847	163532	5.44	7.66	0.71	1.162	4800	2.8	1.98	7.42	1.46	5.41
87933	163993	3.70	24.12	0.52	0.935	5085	3.20	1.8	7.49	4.53	3.83
88048	163917	3.32	21.35	0.79	0.987	4900	2.85	2.05	7.55	3.04	5.60
88636	165683	5.72	4.69	0.62	1.179	4600	2.35	2.05	7.37	1.39	5.02
88684	165438	5.74	28.61	0.83	0.968	4955	3.60	1.22	7.60		
88765	165760	4.64	13.71	0.82	0.951	5025	3.0	1.75	7.45	1.02	5.85
88839	165634	4.55	9.38	0.77	0.938	4980	2.65	1.73	7.44	1.49	3.58
89008	166640	5.57	7.52	0.57	0.915	5080	3.0	1.54	7.50	1.80	5.95
89587	167768	5.99	9.91	0.83	0.890	4930	2.5	2.05	6.72	4.42	7.58
89826	168775	4.33	13.71	0.56	1.162	4590	2.50	1.7	7.64	2.81	5.00
89919		8.88	3.81	0.80	1.058	5130	3.1	1.6	7.41		
89962	168723	3.23	52.81	0.75	0.941	4955	3.2	1.33	7.34	0.44	3.52
90067	169191	5.25	7.48	0.66	1.250	4515	2.65	1.75	7.44	0.95	4.85
90139	169414	3.85	25.40	0.65	1.168	4585	3.0	1.45	7.56	3.48	2.62
90496	169916	2.82	42.20	0.90	1.025	4770	2.9	1.45	7.44	3.81	3.07
91004	171115	5.49	0.95	0.97	1.795	3835	0.25	3.1	7.03	7.31	5.85
91105	171391	5.12	11.25	0.78	0.926	5125	3.15	1.55	7.47	3.05	6.04
91117	171443	3.85	18.72	0.81	1.317	4280	2.15	1.88	7.51	4.58	4.39
92747	174947	5.68	1.88	0.85	1.206	4685	2.10	2.48	7.38	3.82	7.19
93026	175751	4.83	15.77	0.89	1.057	4730	2.85	1.85	7.46	3.00	2.97
93085	175775	3.52	8.76	0.99	1.151	4595	2.4	2.1	7.48	6.29	5.01
93429	176678	4.02	21.95	0.92	1.079	4690	2.95	1.53	7.51	3.91	2.88
93864	177716	3.32	27.09	1.48	1.169	4690	3.2	3.9	7.22	1.04	4.90
94302	180006	5.13	9.57	0.47	1.008	4940	2.9	1.54	7.58	5.00	5.68
94624	180262	5.58	5.32	0.90	1.067	4960	2.6	1.77	7.49	5.48	5.72
94779	181276	3.80	26.48	0.49	0.950	5050	3.25	1.65	7.58	4.28	3.74
94820	180540	4.88	6.09	0.86	1.013	4850	2.2	1.95	7.31	4.08	7.45
95352	182694	5.85	8.06	0.47	0.924	5115	3.1	1.59	7.48	3.20	6.02
95785	183491	5.82	6.74	0.72	1.023	4890	2.85	1.64	7.57	2.80	5.58
96229	184406	4.45	29.50	0.78	1.176	4670	3.2	1.82	7.53	2.78	2.83
96327	184492	5.12	7.34	0.76	1.122	4875	2.5	2.16	7.33	8.88	7.49
96459	185351	5.17	24.64	0.49	0.928	5050	3.55	1.46	7.49	2.06	3.00
96516	185194	5.67	6.89	0.72	1.007	4975	2.7	1.74	7.51	3.32	5.75
97118	186675	4.89	11.70	0.50	0.948	5050	2.85	1.65	7.47	2.94	5.89

Table 5.2: Continued.

HIP	HD	V	plx	e_plx	$B-V$	$T_{\rm eff}$	$\log g$	ξ	[Fe/H]	$\upsilon \sin i$	$\upsilon_{\rm macro}$
		mag	mas	mas	mag	K	dex	km/s		km/s	km/s
97402	187193	6.00	8.16	0.72	0.993	4930	2.95	1.52	7.38	1.24	5.66
98337	189319	3.51	11.90	0.71	1.571	4150	1.70	2.85	7.09	5.81	4.14
98571	190147	5.06	7.60	0.47	1.122	4700	2.5	1.95	7.38	3.63	5.21
98823	190327	5.51	6.19	0.79	1.063	4850	2.7	1.98	7.34	10.30	5.50
99951	192944	5.30	6.91	0.64	0.951	5000	2.7	1.68	7.39	5.02	5.80
100064	192947	3.58	30.01	0.91	0.883	5035	1.75	2.62	7.34	7.79	7.74
100587	194317	4.43	12.77	0.62	1.331	4435	2.7	2.0	7.53	4.85	2.26
100754	194577	5.68	6.00	0.73	0.921	5075	3.0	1.47	7.51	4.65	5.94
101870	196753	5.91	1.65	0.74	0.953	4550	1.65	2.3	7.13	6.20	6.97
101986	197139	5.97	6.93	0.54	1.186	4485	2.4	1.44	7.41	6.39	4.79
102422	198149	3.41	69.73	0.49	0.912	4985	3.45	1.34	7.31	1.04	2.00
102453	197912	4.22	15.84	0.62	1.051	4940	3.17	1.87	7.46	4.31	3.48
102488	197989	2.48	45.26	0.53	1.021	4785	2.75	1.62	7.38	3.01	3.11
102978	198542	4.12	5.19	0.95	1.633	3960	0.85	2.9	6.88	4.68	6.04
103294	199253	5.19	6.88	0.74	1.119	4625	2.35	1.75	7.30	4.80	5.07
103360	199612	5.92	2.56	0.52	1.054	4740	2.6	2.0	7.40	4.76	5.29
104060	200905	3.72	2.77	0.52	1.609	3920	1.00	3.1	7.08	9.30	3.69
104459	201381	4.50	19.93	0.77	0.926	5025	3.10	1.5	7.48	3.29	3.68
104963	202320	5.17	4.72	0.82	1.161	4515	1.85	2.07	7.23	4.14	6.92
105412	203222	5.87	9.69	0.86	0.912	5050	3.05	1.46	7.50	1.79	5.89
105497	203644	5.68	9.93	0.55	1.100	4740	2.75	1.77	7.53	4.25	5.29
105515	203387	4.28	15.13	0.80	0.888	5025	3.0	1.48	7.34	5.67	5.85
106039	204381	4.50	18.18	0.89	0.889	5155	3.30	1.78	7.47	5.74	4.00
106481	205435	3.98	26.20	0.51	0.885	5125	3.25	1.46	7.34	4.26	3.93
107188	206453	4.72	11.22	0.79	0.868	5040	2.65	1.72	7.10	3.72	5.88
107315	206778	2.38	4.85	0.84	1.520	4150	1.25	3.5	7.31	8.32	6.34
107382	206834	5.10	4.08	0.89	1.108	4815	2.35	2.63	7.30	3.75	7.39
108691	209128	5.60	4.93	0.83	1.279	4465	2.60	2.18	7.40	4.04	4.75
109023	209761	5.75	8.22	0.73	1.249	4420	2.35	1.73	7.41	5.19	4.67
109068	209747	4.86	12.38	0.90	1.443	4130	1.90	2.03	7.51	4.77	4.10
109492	210745	3.39	4.49	0.50	1.558	4120	0.75	3.4	7.27	10.64	6.30
109602	210762	5.97	1.07	0.70	1.500	4185	1.65	2.45	7.49	7.87	4.21
109754	211073	4.50	5.79	0.64	1.385	4360	2.45	2.77	7.40	6.50	2.08
109937	211388	4.14	5.20	0.61	1.447	4260	2.15	2.7	7.50	7.60	4.35
109972	211554	5.88	4.48	0.56	0.950	5075	2.8	1.84	7.57	5.21	5.94
110000	211361	5.34	6.74	0.88	1.132	4800	2.9	1.83	7.48	3.43	5.41
110003	211391	4.17	17.04	0.74	0.979	5000	3.1	1.67	7.56	3.94	3.62
110023	211434	5.75	9.56	0.86	0.878	5025	2.7	1.6	7.18	1.96	5.85
110532	212320	5.92	7.10	0.93	0.998	5030	2.9	1.95	7.22	2.89	5.86
110602	212430	5.76	6.01	0.76	0.970	4975	2.75	1.73	7.28	4.07	3.56
110986	213119	5.60	5.63	0.85	1.578	4090	1.65	2.5	7.01	5.01	4.02
111362	213930	5.72	9.60	0.53	0.966	4975	3.05	1.61	7.54	5.18	5.75
111394	213789	5.88	7.35	0.86	0.977	5015	3.0	1.66	7.39	3.80	5.83

Table 5.2: Continued.

HIP	HD	V	plx	e_plx	$B-V$	$T_{\rm eff}$	$\log g$	ξ	[Fe/H]	$\upsilon \sin i$	$\upsilon_{\rm macro}$
		mag	mas	mas	mag	K	dex	km/s		km/s	km/s
111925	214878	5.94	9.49	0.54	0.946	5050	3.15	1.49	7.53	3.86	3.74
111944	214868	4.50	10.81	0.56	1.318	4445	2.50	2.05	7.32	1.80	4.71
112067	214995	5.92	12.22	0.79	1.114	4680	2.70	1.8	7.45	7.21	5.17
112242	215373	5.11	11.89	0.60	0.960	4950	2.87	1.69	7.50	3.61	5.70
112440	215665	3.97	8.26	0.70	1.070	4650	2.0	1.89	7.23	8.03	7.13
112529	215721	5.24	12.26	0.87	0.941	4900	2.6	1.86	7.01	3.90	3.38
112724	216228	3.50	28.27	0.52	1.053	4830	3.00	1.59	7.54	3.27	3.21
112748	216131	3.51	27.95	0.77	0.933	4980	2.9	1.51	7.39	0.20	5.76
113084	216646	5.82	9.63	0.79	1.136	4600	2.65	1.65	7.56	3.05	2.66
113562	217303	5.66	4.62	0.71	1.253	4250	1.50	1.76	6.75	3.86	4.33
113622	217459	5.85	5.96	0.80	1.343	4260	2.05	1.84	7.36	2.51	4.35
113686	217563	5.94	1.23	0.91	0.992	4950	2.0	2.27	7.36	2.14	7.61
113864	218029	5.25	8.48	0.52	1.248	4450	2.4	1.78	7.68	3.18	4.72
114341	218594	3.68	13.96	0.94	1.202	4435	2.15	2.09	7.29	3.59	4.70
114449	218792	5.68	6.45	0.81	1.330	4330	2.55	1.91	7.51	4.12	2.01
114855	219449	4.24	21.97	0.89	1.107	4715	2.70	1.73	7.46	2.78	5.24
114971	219615	3.70	24.92	0.89	0.916	4940	2.9	1.76	6.95	4.20	3.48
115152	219945	5.44	9.95	0.63	1.014	4880	2.85	1.55	7.40	1.21	5.56
115438	220321	3.96	20.14	0.72	1.082	4655	2.65	1.59	7.23	3.08	2.79
115669	220704	4.38	10.57	0.72	1.460	4150	1.8	2.34	7.22	3.90	4.14
115830	220954	4.27	20.54	0.80	1.062	4775	2.95	1.84	7.51	1.79	3.08
117375	223252	5.49	11.19	0.85	0.941	5000	3.0	1.6	7.41	2.57	5.80
117567	223559	5.70	7.09	0.92	1.488	4090	1.20	2.25	6.93	3.44	4.02
117756	223807	5.76	5.33	0.81	1.171	4605	2.65	1.89	7.47	3.60	2.67
118209	224533	4.88	14.58	0.83	0.930	5115	3.3	1.56	7.47	4.64	3.90

Summary and Future prospects

SUMMARY

In this thesis I have investigated radial velocity variations in red giant stars and studied mechanisms, e.g. oscillations, starspots and sub-stellar companions, which possibly cause these variations.

Short tem radial velocity variations: Solar-like oscillations

Four red (sub)giants, which are known solar-like oscillators, were investigated on short timescales for radial velocity variations. Analysis of line profile variations, taking damping and re-excitation into account, revealed that non-radial oscillations are observable in these red (sub)giants. These observational results are a new incentive to improve current theoretical models, because, so far, theory predicted that only radial oscillations can be observable at the surface, due to damping of non-radial modes in the vicinity of the very dense core of the star. Observations obtained with CORALIE mounted on the Swiss 1.2 m Euler telescope at La Silla, ESO, Chile and processed with the INTER-TACOS (INTERpreter for the Treatment, the Analysis and the COrrelations of Spectra) software package (Baranne et al. 1996) were used for this research (Chapter 2).

Long term radial velocity variations

The long term radial velocity survey, using data obtained with the Hamilton échelle spectrograph mounted on the Coudé Auxiliary Telescope (CAT) at University of California Observatories / Lick Observatory, USA and processed with the pipeline described by Butler et al. (1996), revealed that there is a region in the M_V vs. $B-V$ diagram, roughly $0.8 < B-V < 1.2$ and $-2 < M_{\rm V} < 4$, in which most K giants are stable. Stable stars were defined as stars with a standard deviation of the radial velocity less than 20 m s^{-1} (Chapter 3). A trend between radial velocity amplitude and $\log g$ was found, independent of periodicity, which provids an indication that a large fraction of the observed radial velocity variations are possibly induced by processes intrinsic to the stars. On the other hand, if the observed radial velocity variations with significant periodicity are interpreted as due to sub-stellar companions, then the orbital parameters are significantly different from what is known from sub-stellar companions orbiting F, G and K main sequence stars. It would also mean that massive sub-stellar companions ($> 1{\rm M}_{\rm Jup}$) are 5 times more common around red giant stars than around main sequence stars.

In order to investigate the mechanism(s) inducing the radial velocity variations for individual stars, a line profile analysis was performed on high resolution data from the SARG échelle spectrograph mounted on the Telescopio Nazionale Galileo (TNG) at La Palma, Spain. Despite the fact that these data had only scarce time sampling and lacked an accurate wavelength calibration, a line residual analysis was performed to try to distinguish between different mechanisms inducing radial velocity variations (Chapter 4).

Determination of accurate stellar parameters

For about 380 G and K giant stars for which long-term radial velocity observations were performed, the effective temperature, surface gravity, and iron abundance were determined. This was done by imposing excitation and ionisation equilibrium for iron lines, using an LTE analysis (MOOG, Sneden (1973)) and a grid of Kurucz model atmospheres (Kurucz 1993). For 112 stars, these parameters were not determined before, while the parameters for all other stars were in good agreement with literature values. Furthermore, the mean metallicity of giant stars with announced sub-stellar companions turned out to be 0.15 ± 0.05 dex higher than the mean metallicity of the 380 stars investigated here. This is in agreement with the enhanced metallicity found for companion harbouring main sequence stars.

Rotational velocities were also determined for the 380 G and K giant stars, using the method developed by Fekel (1997). The equivalent width of moderate lines were determined and corrected for instrumental effects. For stars in common with Gray (1989), a calibration was obtained to convert the corrected equivalent widths in Å to total broadening in $\mathrm{km\,s^{-1}}$. An estimate for the macro turbulence was obtained from Gray (2005). The rotational velocity was determined as the square root of the quadratic subtraction of the macro turbulence from the total broadening. The rotational velocities, determined here, are in good agreement with those of the stars available in the literature (Chapter 5).

FUTURE

Solar-like oscillations

In December 2006, the CoRoT (COnvection, ROtation and planetary Transits) satellite was successfully launched and the Kepler mission is scheduled for launch in November 2008. These missions are designed to search for extra-solar planetary systems, using the transit technique. This will entail continuous monitoring of a single patch of the sky for 5 months (CoRoT) up to at least 4 years (Kepler), with a high cadence. Stars in these fields are of course also targets for asteroseismology. Also, CoRoT has an additional CCD developed for asteroseismology. With the long continuous time series of high precision data with high time resolution available from these satellites, it will be possible to resolve oscillation frequencies of red giants.

In order to identify the observed oscillation modes, a detailed model of oscillating red giant atmospheres is needed. The extended atmospheres of the red giant stars imply that spectral line forming regions extend over a large depth. So far, all computations have assumed spectral line formation at a single depth in the star, which is a good approximation for the sun, but

perhaps not for red giants. The oscillations possibly change amplitude and/or phase over depth, and, therefore, oscillations will have different behaviour at the surface of these giant stars. This behaviour can be computed from 3-dimensional stellar models, because the depth of the formation of spectral lines could be taken into account. Such 3-dimensional models, which could be used as input for oscillation computations, have recently been developed by, among others, Collet et al. (2007).

From a theoretical point of view, it would be interesting to investigate the damping of non-radial modes close to the stellar core. This damping was assumed but not really calculated before, but is crucial to know the oscillatory behaviour at the surface. Damping of non-radial modes is mentioned as a mechanism responsible for the theoretical prediction of only radial oscillations to be observable. The damping of non-radial oscillation modes can possibly be calculated from first principles for different stages of hydrogen shell burning and helium core burning. For most red giant stars, the exact stages of hydrogen shell and helium core burning cannot be revealed from the luminosity or colour of the star. But, the cores of stars at different stages are considerably different, which, most likely, has influence on the damping of non-radial oscillations inside the star, and thus on the oscillations observed at the surface. These calculations would seriously improve the internal structure models of red giant stars.

In order to establish the results on non-radial solar-like oscillations in red giants presented in this thesis, it would be interesting to perform the same analysis, as performed on the red giants, for the sun. The oscillation modes of the sun are well known and this could be a way to identify which non-radial modes are present in the observed line profiles of red giants.

Long term radial velocity variations

Although a first step is made, it is still difficult to determine the mechanism inducing the observed long term radial velocity variations in red giants. A more detailed interpretation of the radial velocity and line shape variability, in terms of a physical mechanism, requires far more extensive spectroscopic time series suitable for line shape analysis, than the data assembled in this thesis. It would be favourable to have time series of spectra, covering a full radial velocity period with short cadence, from a stabilised spectrograph, such that an accurate wavelength calibration can be obtained. From such a data set, it should be possible to reveal the physical mechanism inducing the observed radial velocity variations, using for instance the spectral line diagnostics described in this thesis. Also, a time series of high precision photometry (from space), covering a full radial velocity period, could be useful to detect possible photometric variations associated with the radial velocity variations.

Stellar parameters

In this thesis, the iron abundance was determined for about 380 G and K giant stars. It would also be very interesting to determine the lithium abundance in these stars. One of the reasons for Li enhancement is enrichment by sub-stellar companions. Although none of the stars in the sample is Li-rich, it may be possible to put constraints on the sub-stellar companion hypothesis. Also, abundances of other metals could be determined and may be interesting.

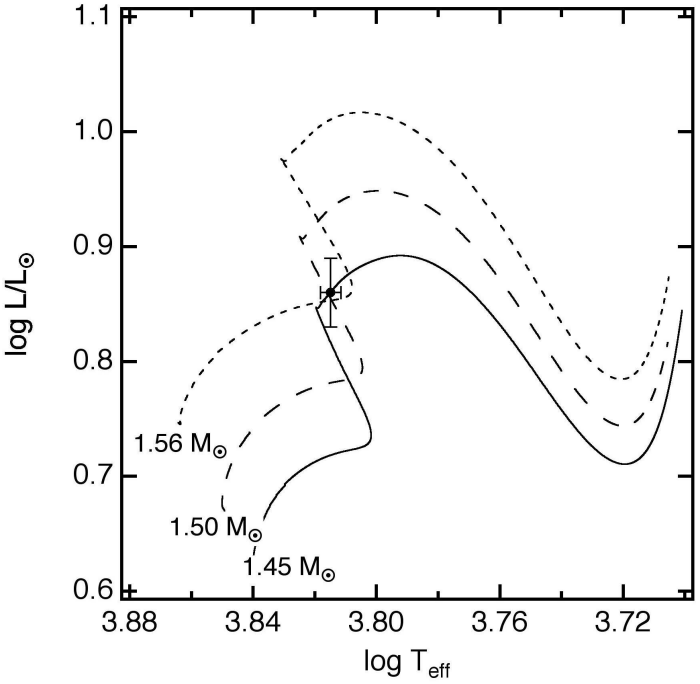

Figure 6.1: Location of Procyon in the Hertzsprung-Russell diagram. Three different evolutionary tracks with the same initial composition (X = 0.71, Z = 0.02) but slightly different masses all pass through the observed position of Procyon. The three models are in different evolutionary phases and span a wide range of ages: the 1.45 $M_{\odot}$ model (age 2.47 Gyr) has exhausted its core of hydrogen, the 1.5 $M_{\odot}$ model (age 2.20 Gyr) still has a hydrogen core mass fraction of $X_{\rm core}$ = 0.005, while the 1.56 $M_{\odot}$ model (age 1.74 Gyr) has $X_{\rm core}$ = 0.138. A full set of reliable oscillation frequencies should indicate clearly which model is correct. Figure from Matthews et al. (2004).

Procyon

I recently contributed to a worldwide asteroseismology observing campaign on Procyon, an F5IV, 1.5 solar mass star close to the end of its main sequence life. This star is an excellent target for asteroseismology, because:

- it is nearby and extremely well studied. In fact, Procyon is the closest F-type subgiant and it is an astrometric binary, so that its distance, mass and angular diameter are all known to high precision,
- it is bright (V=0.3 mag). Detecting oscillations is difficult and the best precision can be achieved on the brightest stars,
- it is hotter than all other stars so far investigated for solar-like oscillations, and it is therefore of great interest for understanding the physics controlling the lifetimes and amplitudes of the oscillations,
- it is in a very interesting stage of its evolution, near the end of core hydrogen burning, see Figure 6.1. Accurate measurements of a substantial number of frequencies will provide strong constraints on the evolution of intermediate-mass stars in this phase, including the effects of the convective core and possibly convective overshoot and/or rotational mixing.

Observations for this world wide campaign on Procyon were taken from December 28, 2006 until January 21, 2007, using UCLES at the AAT, Australia (12 nights), HARPS at the 3.6 m telescope (7 nights) and CORALIE at the 1.2 m Euler telescope (6 nights), La Silla, Chile, SARG at TNG (4 nights) and FIES at the NOT (10 nights), La Palma, Spain, SOPHIE at the 1.93 m, Observatoire de Haute Provence, France (10 nights), HIDES at the 1.88 m telescope,

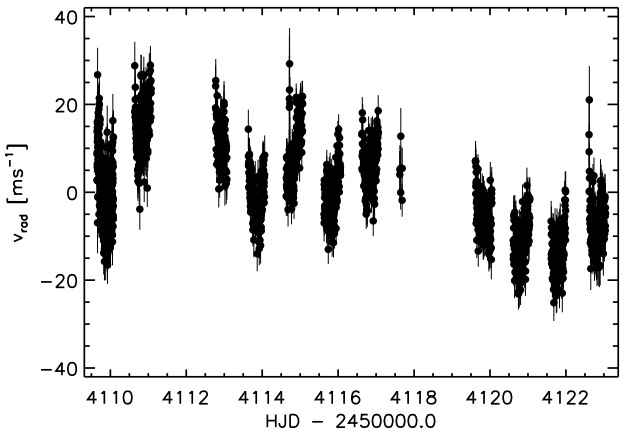

Figure 6.2: The radial velocity variations of Procyon as a function of time obtained at Lick Observatory from January 8 until January 21, 2007. The velocity dispersion of the 1900 observations is 10.1 m s^{-1} with a mean error of 4.1 m s^{-1}.

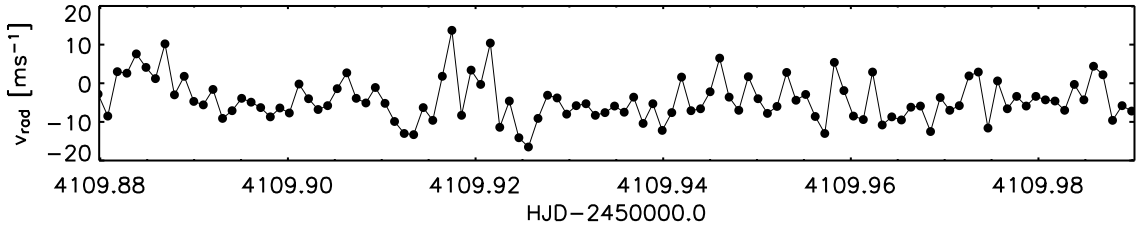

Figure 6.3: A short time interval of radial velocity observations of Procyon.

Okayama, Japan (20 nights), the échelle spectrographs in Tautenberg, Germany (20 nights), and at McDonald observatory, Texas, USA (6 nights). I contributed with a fortnight of observations using the Hamilton échelle spectrograph at the CAT, UCO/Lick Observatory, USA. Apart from these spectroscopic observations, the MOST (Microvariability and Oscillations of Stars) satellite performed photometry on Procyon during the same period.

All radial velocity observations obtained at Lick Observatory are shown in Figure 6.2 as a function of time. The velocity dispersion of this data set is 10.1 m s^{-1} with a mean error in each data point of 4.1 m s^{-1}. The periods of the solar-like oscillations are of order minutes and the variation over several nights are caused by a still unknown effect. In Figure 6.3, a short time interval of radial velocity observations of Procyon is shown.

At the time of writing, the data processing and combination of the data obtained at all telescopes, as well as interpretation, is ongoing. Here I show some preliminary results from the Lick data. In Figure 6.4 a periodogram is shown, obtained from the data shown in Figure 6.2. I did not yet remove the long trend from the data nor any bad observations. There is large power excess at low frequencies, which is caused by the long-term variations. From earlier observations and simulations it is known that the solar-like oscillations on Procyon have frequencies between 500 and 1500 μHz. Some power excess is present in this region in Figure 6.4, and 3 frequencies are believed to be observed with 99% significance (1039.2 μHz, 774.3 μHz and 709.1 μHz).

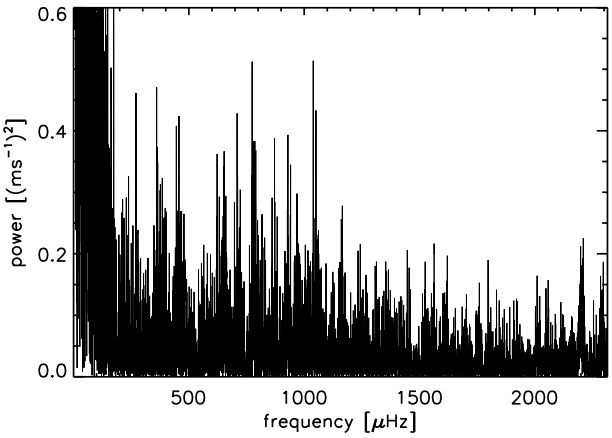

Figure 6.4: Periodogram of the data shown in Figure 6.2, without removing the trend or any bad data point.

REFERENCES

Baranne, A., Queloz, D., Mayor, M., et al. 1996, A&AS, 119, 373

Butler, R. P., Marcy, G. W., Williams, E., et al. 1996, PASP, 108, 500

Collet, R., Asplund, M., & Trampedach, R. 2007, A&A, 469, 687

Fekel, F. C. 1997, PASP, 109, 514

Gray, D. F. 1989, ApJ, 347, 1021

Gray, D. F. 2005, The Observation and Analysis of Stellar Photospheres (The Observation and Analysis of Stellar Photospheres, 3rd Edition, by D.F. Gray. ISBN 0521851866 Cambridge, UK: Cambridge University Press, 2005.)

Kurucz, R. 1993, ATLAS9 Stellar Atmosphere Programs and 2 km/s grid. Kurucz CD-ROM No. 13. Cambridge, Mass.: Smithsonian Astrophysical Observatory, 1993, 13

Matthews, J. M., Kusching, R., Guenther, D. B., et al. 2004, Nature, 430, 51

Sneden, C. A. 1973, PhD thesis, AA(The University of Texas Austin)

Bibliography

REFEREED PAPERS

Precise radial velocities of giant stars. IV. Stellar parameters
Hekker, S., Meléndez, J.
2007, Astronomy & Astrophysics, submitted
Chapter 5

Precise radial velocities of giant stars. III. Variability mechanism derived from statistical properties and from line profile analysis
Hekker, S., Snellen, I. A. G., Aerts, C., Quirrenbach, A., Reffert, S., Mitchell, D. S.
2007, Astronomy & Astrophysics, submitted
Chapter 4

Retired A Stars and their Companions: Exoplanets Orbiting Three Intermediate-Mass Subgiants
Johnson, J. A., Fischer, D. A., Marcy, G. W., Wright, J. T., Driscoll, P., Butler, R. P., **Hekker, S.**, Reffert, S., Vogt, S. S.
2007, The Astrophysical Journal, in press.

Precise radial velocities of giant stars. II. Pollux and its planetary companion
Reffert, S., Quirrenbach, A., Mitchell, D. S., Albrecht, S., **Hekker, S.**, Fischer, D. A., Marcy, G. W., Butler, R. P.
2006, The Astrophysical Journal, Volume 652, pp. 661–665

Pulsations detected in the line profile variations of red giants. Modelling of line moments, line bisector and line shape
Hekker, S., Aerts, C., De Ridder, J., Carrier, F.
2006, Astronomy & Astrophysics, Volume 458, pp. 931–940
Chapter 2

Precise radial velocities of giant stars. I. Stable stars
Hekker, S., Reffert, S., Quirrenbach, A., Mitchell, D. S., Fischer, D. A., Marcy, G. W., Butler, R. P.
2006, Astronomy & Astrophysics, Volume 454, pp. 943–949
Chapter 3

CONFERENCE PROCEEDINGS

High-Precision Spectroscopy of Pulsating Stars
Aerts, C., **Hekker, S.**, Desmet, M., Carrier, F., Zima, W., Briquet, M., De Ridder, J.
2007, To appear in Precision Spectroscopy in Astrophysics, Eds. Pasquini, M. Romaniello, N.C. Santos, and A. Correia, Springer-Verlag series " ESO Astrophysics Symposia"

A line profile analysis of the pulsating red giant star Ophiuchi (G9.5III)
Hekker, S., Aerts, C., De Ridder, J., Carrier, F.
2006, Proceedings of SOHO 18/GONG 2006/HELAS I, Beyond the spherical Sun (ESA SP–624). 7–11 August 2006, Sheffield, UK. Editor: Karen Fletcher. Scientific Editor: Michael Thompson, Published on CDROM, p. 117.1

Multiplicity in a Complete Sample of Giant Stars
Reffert, S., Quirrenbach, A., **Hekker, S.**, Mitchell, D. S., Fischer, D. A., Marcy, G. W., Butler, R. P.
2006, Binary stars as Critical Tools and Tests in Contemporary Astrophysics, IAU 240, held 22–25 August, 2006 in Prague, Czech Republic, S240, 143

Radial velocity variations in K giants: planets or pulsations?
Hekker, S., Reffert, S., Quirrenbach, A.
2006, Communications in Asteroseismology, Volume 147, pp. 121–124

Choosing Suitable Target, Reference and Calibration Stars for the PRIMA Astrometric Planet Search
Reffert, S., Launhardt, R., **Hekker, S.**, Henning, T., Queloz, D., Quirrenbach, A., Segransan, D., Setiawan, J.
2005, Astrometry in the Age of the Next Generation of Large Telescopes, Vol. 338, Proceedings of a meeting held 18-20 October 2004 at Lowell Observatory, Flagstaff, Arizona, USA. Edited by P. Kenneth Seidelmann and Alice K. B. Monet. San Francisco: ASP, p. 81

Preparing the PRIMA astrometric planet search: selecting suitable target and reference stars
Frink, S., **Hekker, S.**, Launhardt, R., Setiawan, J., Segransan, D., Quirrenbach, A., Henning, T., Queloz, D.
2004, New Frontiers in Stellar Interferometry, Proceedings of SPIE Volume 5491. Edited by Wesley A. Traub. Bellingham, WA: The International Society for Optical Engineering, p. 1166

Radiële snelheidsvariaties in Rode Reuzen: trillingen, vlekken en planeten

STERREN worden net als mensen geboren, worden volwassen, oud en gaan daarna weer dood. De eerste stappen op het 'levenspad' worden door sterren echter niet gezet door het samensmelten van een eicel met een zaadcel, gevolgd door celdeling. Nee, een ster ontstaat door een samenspel van zwaartekracht en materie. Onder invloed van zijn eigen zwaartekracht zal een wolk van waterstofgas ineen vallen en een grotere dichtheid krijgen. Hierdoor wordt het in het centrum van de gaswolk erg heet en kan kernfusie plaatsvinden. Dit zal eerst gebeuren voor de lichtste elementen, deuterium (1 proton en 1 neutron in de kern) en daarna waterstof (1 proton en 2 neutronen in de kern). Deze elementen fuseren tot helium (2 protonen met 2 neutronen in de kern). Bij deze kernfusie komt veel energie vrij waardoor de ster gaat schijnen. Omdat nog niet al het gas en stof uit de wolk, waaruit de ster ontstaan is, echt aan de ster gebonden is, zal dit in een schijf rond de ster gaan draaien. In deze schijf kunnen 'klonten' ontstaan die kunnen uitgroeien tot planeten. Al het overgebleven gas en stof wordt door de ster 'weggeblazen'. De ster is nu in een 'volwassen' evenwichtstoestand gekomen die, afhankelijk van de massa van de ster, miljarden jaren kan duren.

Op een gegeven moment raakt het waterstof op en zal de ster over moeten gaan op het fuseren van helium tot koolstof. Deze fusie vindt plaats bij een hogere temperatuur dan de fusie van waterstof tot helium. Net als bij het ontstaan kan een ster onder invloed van de zwaartekracht weer dichter en heter worden in de kern, waardoor bij een temperatuur van 100 miljoen graden heliumfusie zal beginnen. Terwijl de kern van de ster zich samentrekt, zal de buitenste laag van de ster opzwellen en afkoelen. Licht afkomstig van een koeler object is roder en deze opgezwollen rode ster wordt dan ook een Rode Reus genoemd. Sterren in deze 'oude levensfase' zijn onderzocht in dit proefschrift. Veel van de helderste sterren aan de hemel, zoals Aldebaran, Arcturus en Pollux, zijn rode reuzen.

Als de ster zwaar genoeg is zal het in de kern nog dichter en heter kunnen worden, zodat koolstof kan fuseren. Deze hele zware sterren 'sterven' uiteindelijk door te imploderen en in één klap uit elkaar te vallen. We zien dan een supernova. Minder zware sterren zullen langzaam uitdoven.

RADIËLE SNELHEIDSVARIATIES

De radiële snelheid is de snelheid in de richting van de straal (radius) van de aarde, dus van ons af of naar ons toe. Sterren in ons melkwegstelsel bewegen allemaal, net als de zon en

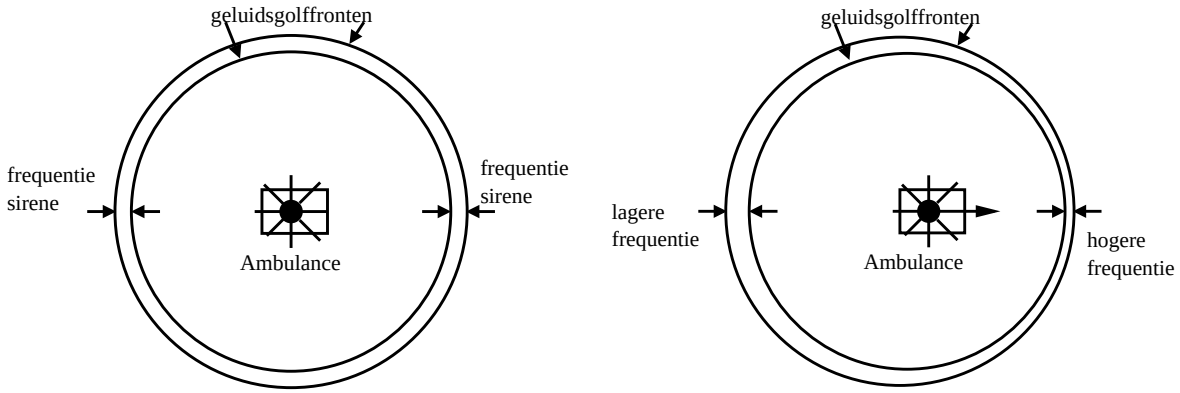

Figuur 8.1: Links: een ambulance met sirene die stil staat. De afstand tussen de geluidsgolffronten is overal even groot en het geluid heeft overal dezelfde frequentie. Rechts: een ambulance met sirene rijdt naar rechts. De afstand tussen de golffronten is nu aan de voorzijde van de ambulance kleiner dan bij stilstand en het geluid heeft een hogere frequentie. De afstand tussen de golffronten aan de achterzijde van de ambulance is groter en de frequentie is hoorbaar met een lagere frequentie.

de aarde. Dit is een 3-dimensionale beweging, waarbij sterren zowel een component in het noord-zuid, oost-west vlak aan de hemel kunnen hebben, als in de radiële richting. Ik heb in dit proefschrift alleen bewegingen in radiële richting bekeken. Dit kan je doen door naar de Doppler verschuiving van een spectrum te kijken.

Doppler verschuiving komt in het dagelijks leven bijvoorbeeld voor bij het voorbij rijden van een ambulance met loeiende sirene. Op het moment dat de ambulance nadert heeft het geluid van de sirene een hogere frequentie dan als de ambulance voorbij komt. Bij het wegrijden is de frequentie van de sirene lager. Dit komt doordat de sirene steeds een geluidsgolf uitzendt. Deze golf reist met een bepaalde snelheid. De volgende geluidsgolf vertrekt een tijdje na de eerste geluidsgolf. In de richting die de ambulance op rijdt, zal de afstand tussen de geluidsgolven kleiner zijn, namelijk met de afstand die de ambulance heeft afgelegd tussen het uitzenden van de eerste en tweede geluidsgolf. Dit geeft dus een hogere frequentie. Achter de ambulance zal de afstand tussen de geluidsgolven juist toegenomen zijn met de afstand die de ambulance heeft afgelegd tussen het uitzenden van de golven. Vandaar de lagere frequentie van het geluid als de ambulance van je weg rijdt. Dit is schematisch weergegeven in Figuur 8.1. Het Doppler effect treedt niet alleen op bij geluidsgolven, maar ook bij lichtgolven.

Net als de zon schijnt een ster in alle kleuren van de regenboog (zonlicht gebroken door regendruppels), ofwel een heel spectrum van licht met verschillende frequenties. In feite zendt een ster fotononen (lichtpakketjes) uit met heel veel verschillende frequenties. Doordat er verschillende elementen, zoals bijvoorbeeld, waterstof, zuurstof, ijzer, calcium etc. in de ster aanwezig zijn, wordt het licht op verschillende frequenties zwakker. Dit komt doordat deze elementen, ieder op een eigen frequentie, fotonen invangen (absorberen) waardoor op bepaalde frequenties minder fotonen de aarde bereiken, hierdoor ontstaat een spectrum met absorptie lijnen. Als de ster van ons af of naar ons toe beweegt zullen de absorptie lijnen iets verschoven zijn van hun nominale frequentie net als bij de naderende of wegrijdende ambulance. In dit proefschrift heb ik gekeken naar sterren waarvoor de radiële snelheid varieert en de verschuiving van de absorptie lijnen dus varieert in de tijd.

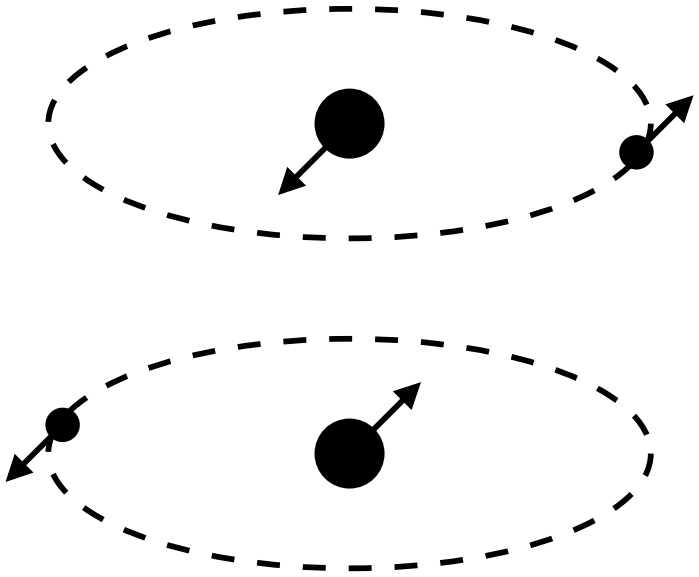

Figuur 8.2: Planeet die rondom een ster draait. Boven: de planeet beweegt van de waarnemer af, dan komt de ster naar de waarnemer toe en is het spectrum blauwverschoven. Onder: de planeet beweegt naar de waarnemer toe, dan beweegt de ster van de waarnemer af en is het licht roodverschoven.

PLANETEN

Het woord planeet is afkomstig uit het grieks en betekent 'zwerver'. Dit is ontstaan doordat de planeten uit ons zonnestelsel ten opzichte van de 'vaste' sterrenhemel bewegen en dus steeds op andere locaties waarneembaar zijn. Sinds augustus 2006 luidt de officiële definitie van een planeet: 'Een hemellichaam dat om (de overblijfselen van) een ster heen beweegt en zwaar genoeg is om, onder invloed van de eigen zwaartekracht, bolvormig te zijn, maar niet zwaar genoeg voor kernfusie. Daarbij moet het de directe omgeving vrij gemaakt hebben van kleinere objecten.' Volgens deze definitie zijn er acht planeten in ons zonnestelsel. Pluto is gedefinieerd als een dwergplaneet.

In 1994 is de eerste planeet rondom een andere ster dan de zon ontdekt en sindsdien zijn er al meer dan 200 waargenomen. Dit waarnemen gebeurt niet direct, maar indirect. Als een planeet om een ster heen draait zal de ster door de zwaartekracht tussen de planeet en de ster ook gaan draaien met een zelfde, maar tegengestelde kracht, zie Figuur 8.2. De perioden van deze bewegingen is gelijk, maar de straal van de beweging is omgekeerd evenredig met de massa van de lichamen. De beweging van de ster is zichtbaar als een variatie in de radiële snelheid en die kunnen we meten, zoals beschreven in de vorige sectie.

Uit de periode en grootte van de radiële snelheidsvariatie kan de massa van de planeet, afhankelijk van de hoek waaronder we tegen het systeem aankijken, afgeleid worden. Als deze massa kleiner is dan $15\times$ de massa van Jupiter dan is het een planeet. In zwaardere objecten van 15-$100\times$ de massa van Jupiter kan deuteriumfusie optreden. Dit zijn bruine dwergen. In een object van meer dan $100\times$ de massa van Jupiter vindt waterstoffusie in de kern plaats. Een dergelijk object is een ster.

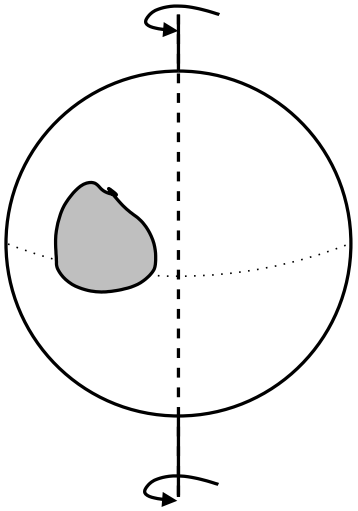

Figuur 8.3: Een donkere vlek op een roterende ster.

VLEKKEN

Op de zon zijn, met een cyclus van 11 jaar, donkere vlekken zichtbaar. Deze plekken zijn donker omdat ze iets koeler zijn dan de rest van het oppervlak van de zon. In Figuur 8.3 is een roterende ster met een vlek schematisch weergegeven. In Figuur 1.7 van de introductie is een opname van een zonnevlek weergegeven. Hierin is duidelijk een zeer donker egaal binnenste deel, de umbra, en buitenste deel bestaand uit filamenten, de penumbra te zien. Deze vlekken ontstaan onder invloed van een magneetveld en geven daarom ook informatie over de magnetische eigenschappen van de ster. De levensduur van vlekken is evenredig met de grootte, in het geval van kleine vlekken. Grote vlekken kunnen jaren 'overleven' op het oppervlak.

Deze vlekken kunnen waargenomen worden door naar de lichtintensiteit van de ster te kijken. Als er een vlek ontstaat, of naar de zichtbare kant van de ster draait, dan zal de lichtintensiteit van de ster iets lager worden door die donkere vlek. Ook kan de vlek in het spectrum van de ster zichtbaar zijn. Het totale spectrum van een ster is opgebouwd uit de spectra van ieder zichtbaar oppervlakte element van de ster. In de vlek is de lichtintensiteit lager en dus zullen de spectra van die gebieden een lagere intensiteit hebben. Dit geeft een vervorming in de absorptie lijnen van het totale spectrum. Bij radiële snelheidswaarnemingen kunnen deze vervormingen een variatie in de gemeten radiële snelheid geven, terwijl de ster in feite met een constante radiële snelheid beweegt. Het meten van verandering in de vorm van de absorptielijnen kan uitsluitsel geven over het mechanisme in de ster dat verantwoordelijk is voor de waargenomen radiële snelheidsvariaties.

TRILLINGEN

Bij het bestuderen van het binnenste van de aarde wordt gebruik gemaakt van trillingen die door de aarde zelf worden voortgebracht, zoals aardbevingen, maar ook door het tot ontploffing brengen van dynamiet, of door andere controleerbare trillingsbronnen. Uit de tijd die een golf onderweg is kan dan opgemaakt worden hoe de aarde er van binnen uitziet. Dit onderzoeksgebied heet seismologie.

Nu is het in principe ook mogelijk om het binnenste van sterren te bestuderen aan de hand van trillingen, als die (meetbaar) aanwezig zijn. Dit is in veel sterren het geval. Stertrillingen worden onderzocht in het vakgebied dat astero(ster)seismologie heet.

Het oppervlak van de zon trilt met een periode van ongeveer 5 minuten en een kleine uitwijkingen van orde $\mathrm{cm\,s^{-1}}$. Deze trillingen ontstaan in de buitenste turbulente laag van de zon door stochastische fluctuaties. In andere sterren met een turbulente atmosfeer komen deze trillingen ook voor, maar deze zijn uiteraard moeilijker waarneembaar dan in de zon. Trillingen kunnen in een ster ook ontstaan in de buurt van de kern doordat daar dichtheidsfluctuaties ontstaan bij de fusie van waterstof naar helium. Ook kunnen trillingen ontstaan doordat een deels geïoniseerde laag energie van de kern naar het oppervlak even 'vasthoudt', waarna het alsnog naar het oppervlak doorstroomt.

Stertrillingen kunnen ervoor zorgen dat de ster meer of minder licht uitstraalt. Dit kan bijvoorbeeld als de hele ster wat krimpt en dan weer opzwelt (radiële trilling), maar het kan ook zijn dat verschillende stukken van de ster opzwellen, terwijl naast gelegen delen juist naar binnen bewegen (niet-radiële trilling). In totaal hoeft dit geen variatie in licht intensiteit te geven. Net als in het geval van de vlek op het steroppervlak kan een trilling ook zichtbaar zijn in het spectrum. De spectra van alle oppervlakte elementen zijn nu een klein beetje blauw- of roodverschoven afhankelijk of dat deel van de ster zwelt of krimpt. Als nu een groter deel van het zichtbare oppervlak van de ster krimpt en dus blauwverschoven is, dan zullen alle absorptie lijnen in het totale spectrum iets 'sterker' zijn aan de blauwe kant en iets 'zwakker' zijn aan de rode kant en vice versa als een groter deel van het zichtbare oppervlak van de ster zwelt en dus roodverschoven is. Ook in deze situatie geldt dat de vervorming van de absorptielijnen aanleiding kan geven tot het meten van een radiële snelheidsverandering, terwijl de ster eigenlijk met een constante radiële snelheid beweegt. Het meten van de verandering in de vormen van de absorptielijnen kan ook in dit geval uitsluitsel geven over het mechanisme dat de gemeten radiële snelheidsvariatie veroorzaakt.

DIT PROEFSCHRIFT

Het onderzoek beschreven in dit proefschrift gaat met name over radiële snelheidsvariaties in rode reuzen. Voor één project zijn ongeveer eens per maand waarnemingen gedaan, terwijl voor een ander project zoveel mogelijk waarnemingen voor één ster per nacht gedaan zijn. De gemeten radiële snelheidsvariaties en mogelijke mechanismen die deze variaties veroorzaken zijn onderzocht.

Hoofdstuk 1

Hoofdstuk 1 is een algemene introductie, waarbij wat dieper op de stof wordt ingegaan dan in deze Nederlandse Samenvatting.

Hoofdstuk 2

In Hoofdstuk 2 zijn vier rode (sub)reuzen onderzocht waarvan al bekend was dat ze trillen op dezelfde manier als de zon. Omdat deze trillingen periodes hebben van een paar uur, zijn deze sterren zo vaak mogelijk per nacht waargenomen. Om nu te achterhalen wat voor soort trillingen er aanwezig zijn in deze sterren, zijn variaties in de vorm van de absorptielijnen onderzocht. Hieruit is voor 3 van de 4 sterren naar voren gekomen dat niet-radiële trillingen aanwezig zijn in deze sterren. Dit is een baanbrekend resultaat, aangezien tot nu toe gedacht werd dat alleen radiële trillingen waarneembaar zouden zijn in rode reuzen.

Hoofdstuk 3

Dit hoofdstuk, samen met de twee volgende, heeft betrekking op maandelijks gemeten radiële snelheidsvariaties aan rode reuzen. Dit is in eerste instantie, vanaf 1999, gedaan voor ongeveer 180 sterren. In 2003 is dit aantal uitgebreid naar ongeveer 380 sterren. Uit de eerste 180 sterren blijken 34 sterren maar een hele kleine variatie in de radiële snelheid te hebben, te weten een standaardafwijking kleiner dan 20 $\mathrm{m\,s^{-1}}$. Het blijkt dat deze sterren allemaal relatief blauw van kleur zijn, en dus relatief warm vergeleken met de andere sterren in de verzameling. Verder behoren deze sterren niet tot de helderste sterren in de verzameling. Dit kunnen interessante gegevens zijn indien men 'stabiele' sterren nodig heeft, bijvoorbeeld als referentiesterren.

Hoofdstuk 4

Behalve 'stabiele' sterren zijn er ook sterren in de verzameling met een periodiek variërende radiële snelheid. Om te achterhalen waardoor deze radiële snelheidsveranderingen ontstaan zijn, is gekeken of er een verband bestaat tussen de amplitude van de radiële snelheid en de oppervlaktezwaartekracht. Dit blijkt het geval te zijn en dit is een eerste indicatie dat de radiële snelheidsvariaties door een mechanisme intrinsiek aan de ster veroorzaakt kunnen worden. Ook is er, voor een klein aantal sterren, een lijnvorm analyse en een temperatuurmeting uitgevoerd om te kijken of daar variaties over tijd in aanwezig waren. Dit is erg lastig gebleken, aangezien hiervoor spectra met goede resolutie, een goede signaal-ruis verhouding en een nauwkeurige golflengtecalibratie nodig zijn. Om vervolgens te kunnen zeggen of de variatie in de absorptie lijnen inderdaad de gemeten radiële snelheidsvariaties veroorzaken, moeten er genoeg waarnemingen voor iedere ster zijn. In dit geval waren er niet voldoende data, maar het lijkt wel mogelijk een eerste indicatie van het mechanisme te kunnen geven.

Verder is er gekeken naar de baanparameters in het geval de periodieke radiële snelheidsvariaties veroorzaakt zouden worden door planeten. Het blijkt dat relatief veel begeleiders dan geen planeten zouden zijn, maar bruine dwergen. Ook zouden de omloop periodes dan veel langer zijn voor begeleiders rond rode reuzen dan voor begeleiders rond zon-achtige sterren.

Hoofdstuk 5

Aangezien voor ongeveer 380 sterren minstens één goed spectrum aanwezig was, zijn voor alle sterren de effectieve temperatuur aan het oppervlak, de oppervlaktezwaartekracht, het ij-

zergehalte en de rotatiesnelheid bepaald. De gevonden resultaten komen zeer goed overeen met waarden uit de literatuur, voor zover die bekend zijn. Dit geeft aan dat de resultaten voor de sterren waarvoor de genoemde parameters nog niet bepaald waren zeer betrouwbaar zijn.

TOEKOMST

Met het onderzoek beschreven in dit proefschrift zijn stappen in de goede richting gezet met betrekking tot de interpretatie van waargenomen radiële snelheidsvariaties, maar er is ook nog veel werk te verrichten. Allereerst, is hier voor het eerst aangetoond dat niet-radiële trillingen aanwezig zijn in rode reuzen. Tot nu toe was het nog niet mogelijk te achterhalen welke niet-radiële trillingen dat zijn. Hiervoor zal verbetering moeten komen in de analyse van de waarnemingen. Ook zijn de theoretische voorspellingen op dit moment niet gelijk aan de waarnemingen en op dit terrein zal dus ook nog vooruitgang geboekt moeten worden.

Verder is de oorzaak van de radiële snelheidsvariaties in rode reuzen nog voor een groot deel onbekend. Hiervoor zal meer data verzameld moeten worden om aan de hand van absorptielijn vormen hierover op grote schaal conclusies te kunnen trekken. Verder is er theoretisch nog veel onbekend over eventuele trillingen met periodes van honderden dagen, zoals die aanwezig lijken te zijn in de rode reuzen. Op dit vlak zou ons begrip van deze sterren dus ook nog zeer kunnen verbeteren.

Voor de sterren in deze verzameling is alleen het ijzergehalte bepaald, maar het lithium gehalte is ook zeer interessant. Hieruit zou bijvoorbeeld afgeleid kunnen worden of er planeten op de ster gevallen zijn. Als hier meer bewijs van waarnemingen voor komt, zou dat kunnen bijdragen aan de ontwikkeling van theorieën met betrekking tot de vorming van planeten.

Curriculum Vitae

I was born on April 24, 1978 in Heeze, The Netherlands, and followed my highschool education at the Augustinianum, Eindhoven. After six years, I received my diploma and because of my technical interests I went to the Delft University of Technology to study Applied Physics. I started this study in September 1996 and managed to obtain my propedeuse within one year. During this same year I started to become an active member of the student association of Applied Physics, the Vereniging voor Technische Physica (VvTP). Over the years, I have been part of many committees and I even joined the board for one year. I have also been member of the management team of the Faculty of Applied Physics, and the student council. Furthermore, I have been chair of the committee organising the freshmen's week at Delft (about 2000 participants).

In April 2003, I graduated *cum laude* for my master degree with a thesis entitled: 'Temperature measurements in Rayleigh-Bénard convection using suspended Liquid Crystals'. I also won, with this research, the poster price for the most interesting science topic at the 100th anniversary symposium of the Faculty of Applied Physics.

From September 2003 on, I have worked as a PhD student in Professor A. Quirrenbach's group at the Leiden Observatory, Leiden University. During the second half of my PhD, I worked under supervision of Dr. I. Snellen and Professor C. Aerts. My research has been focused on radial velocity variations in red giant stars. This research has been observational and I went mostly to UCO/Lick Observatory, California, USA (nearly 100 nights) and to the observatory in La Palma, Spain (13 nights) for my observations. I followed international schools in Dwingeloo (The Netherlands), Garching (Germany), Geneva (Switzerland) and Tenerife (Spain). In addition to these schools, I stayed in Leuven (Belgium) for a three month working visit. During this visit I collaborated with Professor C. Aerts and her co-workers, which formed the basis of Chapter 2 of this thesis. Furthermore, I presented my research at several conferences in Glasgow (Great Britain), Blankenberghe (Belgium), Liège (Belgium), Ameland (The Netherlands), Sheffield (Great Britain), Pasadena (USA), Vancouver (Canada) and Göttingen (Germany). At the meetings in Blankenberghe and Pasadena, I won a poster price for my contribution.

Throughout my life water polo, and swimming has been very important. I have been member of the provincial team and Dutch national youth squad in all age classes. I also participated twice in the European League for national cup winners and I won the national cup once.

In the fall of 2007, I will join the group of Patricia Lampens at the Royal Observatory of Belgium, Brussels and continue to perform research in the field of asteroseismology.

Acknowledgements

PHD research is a project performed in collaboration with others. At this last page of my thesis, I want to take the opportunity to acknowledge some (groups of) people.

The three month working visit to Leuven has been very important for me, both to develop my scientific skills and to experience how exciting research is. I have really enjoyed working in the Leuven Asteroseismology team and I had a great time with the entire staff at the Institute.

I also want to thank the staff at Lick Observatory. Without the treats from Karen, Orpha, Linda and Kim, or the technical support from Kris, Keith, Bernie, Wayne and the maintenance guys, I would not have survived my nearly 100 nights on the mountain. Apart from the profesional support the chats were an important part of daily life. Debra, thanks for showing me the Chuck-a-doe trail.

At the observatory, we would all be lost without the great work from the ladies at the secretariat: Kirsten, Jeanne, Liesbeth, Anita, Elise and Laura and the guys from the computergroup: David, Tycho, Aart and Erik.

This thesis has mainly been funded by NWO through Professor A. Quirrenbach's VICI project: 'Optical Interferometry: A new method for studies of extra solar planets' (NWO project 639.043.201). I am also grateful for the following funds: Leids Kerkhoven Bosscha Fonds, OPTICON, Leids Sterrewacht Fonds, and the European Network 'The Origin of Planetary Systems' for their financial support.

I also want to thank everybody in my group and at the observatory, who gave me some help at any moment during my PhD. Vincent, Dave and Jean-Charles, it was good to share a room with you.

Tot slot zijn mijn ouders en broer(tje) van groot belang geweest voor mijn ontwikkeling. Mijn ouders hebben mij altijd vrij gelaten en gesteund in mijn keuzes en Jaap hield mij met beide voeten aan de grond. Maarten, dankjewel!